3-18-2015

Numerical Investigation of Interfacial Mass Transport Resistance and Two-phase Flow in PEM Fuel Cell Air Channels

Mustafa Koz

R·I·T

NUMERICAL INVESTIGATION OF INTERFACIAL MASS TRANSPORT RESISTANCE AND TWO-PHASE FLOW IN PEM FUEL CELL AIR CHANNELS

by

MUSTAFA KOZ

A dissertation submitted in partial fulfillment of the requirements for the degree of

Doctorate of Philosophy in Microsystems Engineering

Microsystems Engineering Program
Kate Gleason College of Engineering

Rochester Institute of Technology
Rochester, New York
18 March, 2015

NUMERICAL INVESTIGATION OF INTERFACIAL MASS TRANSPORT RESISTANCE AND TWO-PHASE FLOW IN PEM FUEL CELL AIR CHANNELS

Committee Approval:

We, the undersigned committee members, certify that we have advised and/or supervised the candidate on the work described in this dissertation. We further certify that we have reviewed the dissertation manuscript and approve it in partial fulfillment of the requirements of the degree of Doctor of Philosophy in Microsystems Engineering.

Dr. Satish G. Kandlikar — Date
James E. Gleason Professor, Mechanical Engineering Department (Advisor)

Dr. Blanca Lapizco-Encinas — Date
Professor, Biomedical Engineering Department

Dr. Jiandi Wan — Date
Professor, Microsystems Engineering Department

Dr. Steven Day — Date
Professor, Mechanical Engineering Department

Certified by:

Dr. Stefan Preble — Date
Director, Microsystems Engineering Program

Harvey J. Palmer, Ph.D. — Date
Dean, Kate Gleason College of Engineering

ABSTRACT

Kate Gleason College of Engineering
Rochester Institute of Technology

Degree: Doctor of Philosophy **Program:** Microsystems Engineering
Author: Mustafa Koz
Advisor: Satish G. Kandlikar
Dissertation Title: Numerical Investigation of Interfacial Mass Transport Resistance and Two-Phase Flow in PEM Fuel Cell Air Channels

Proton exchange membrane fuel cells (PEMFCs) are efficient and environmentally friendly electrochemical engines. The performance of a PEMFC is adversely affected by oxygen (O_2) concentration loss from the air flow channel to the cathode catalyst layer (CL). Oxygen transport resistance at the gas diffusion layer (GDL) and air channel interface is a non-negligible component of the O_2 concentration loss. Simplified PEMFC performance models in the available literature incorporate the O_2 resistance at the GDL-channel interface as an input parameter. However, this parameter has been taken as a constant so far in the available literature and does not reflect variable PEMFC operating conditions and the effect of two-phase flow in the channels.

This study numerically calculates the O_2 transport resistance at the GDL-air channel interface and expresses this resistance through the non-dimensional Sherwood number (Sh). Local Sh is investigated in an air channel with multiple droplets and films inside. These water features are represented as solid obstructions and only air flow is simulated. Local variations of Sh in the flow direction are obtained as a function of superficial air velocity, water feature size, and uniform spacing between water features. These variations are expressed with mathematical expressions for the PEMFC performance models to utilize and save computational resources.

The resulting mathematical correlations for Sh can be utilized in PEMFC performance models. These models can predict cell performance more accurately with the help of the results of this work. Moreover, PEMFC performance models do not need to use a look-up table since the results were expressed through correlations. Performance models can be kept simplified although their predictions will become more realistic. Since two-phase flow in channels is experienced mostly at lower temperatures, performance optimization at low temperatures can be done easier.

Table of Contents

CHAPTER 1. INTRODUCTION 1

1.1. HYDROGEN ENERGY 1

1.2. INTRODUCTION TO PEMFCs 3

1.2.1. Components 4

1.2.2. PEMFC Operation Principles 7

1.2.3. Two-Phase Flow in PEMFC Components 10

1.2.4. Transport of Oxygen in a PEMFC 12

1.2.5. Oxygen Transport Resistance at the GDL-Air Channel Interface 14

CHAPTER 2. BACKGROUND 17

2.1. TWO-PHASE FLOW DEPENDENT FUEL CELL PERFORMANCE 17

2.1.1. Experimental Evidences of Performance Variations 17

2.1.2. Numerical Evidences of Performance Variations 18

2.2. CONSIDERATIONS OF INTERFACIAL MASS TRANSPORT RESISTANCE IN PEMFC PERFORMANCE MODELING 20

2.2.1. Models Implicitly Solving for the Interfacial Resistance 20

2.2.2. Models Incorporating the Interfacial Resistance as an Input Parameter 22

2.3. INVESTIGATION OF INTERFACIAL MASS TRANSPORT RESISTANCE 22

2.3.1. Utilization of Heat and Mass Transport Analogy 22

2.3.2. Simulation of the Interfacial Transport Resistance 23

2.4. REACTANT CHANNEL TWO-PHASE FLOW PATTERNS 24

2.4.1. In-Situ Visualization of Two-Phase Flow 24

2.4.2. Ex-Situ Visualization of Two-Phase Flow 26
2.4.3. Fundamental Experimental Studies on Two-Phase Flow Patterns 27
CHAPTER 3. OBJECTIVES 32
3.1. OBTAINING THE TRENDS OF SHERWOOD NUMBER AS A FUNCTION OF DROPLET AND FILM CONFIGURATION BY USING NUMERICAL SIMULATIONS 32
3.2. BUILDING CORRELATIONS FOR SHERWOOD NUMBER 33
3.3. EXPANDING THE USE OF SHERWOOD NUMBER CORRELATIONS 33
CHAPTER 4. APPROACH 35
4.1. PHYSICAL MODEL 35
4.1.1. Geometric Configuration for Droplet-GDL-Channel Conjugate Simulations 37
4.1.2. Geometric Configuration for Droplet Simulations 38
4.1.3. Geometric Configuration for Film Simulations 39
4.2. VARIABLES AND THEIR NON-DIMENSIONALIZATION 41
4.3. NUMERICAL MODEL 43
4.3.1. Governing Equations 43
4.3.2. Boundary Conditions (BCs) for the Numerical Model 45
4.3.3. Selection of Input Parameters 51
4.3.4. Mesh Independency and Validation 59
CHAPTER 5. RESULTS 68
5.1. TRENDS OF SHERWOOD NUMBER 68
5.1.1. Effect of Droplets 68
5.1.2. Effect of Injection/Suction at the GDL-Air Channel Interface 83

5.1.3. Effect of Films 86

5.2. SHERWOOD NUMBER CORRELATIONS 96

5.2.1. Droplet Correlations 96

5.2.2. Film Correlations 99

5.3. EXPANDING THE USE OF SHERWOOD NUMBER CORRELATIONS 105

5.3.1. Applicability of Droplet Results to Different Length Scales and Air Properties 105

5.3.2. Applicability of Single-Film Correlations to Multiple Films and Different Air Properties 106

CHAPTER 6. CONLUSIONS AND FUTURE WORK 110

6.1. Conclusions 110

6.1.1. Addressing the Needs in the Available Literature 110

6.1.2. Approach 110

6.1.3. Major Conclusions 111

6.1.4. Specific Conclusions for Droplets 112

6.1.5. Conclusions for Films 113

6.2. Future Work 115

CHAPTER 7. REFERENCES 116

List of Figures

Figure 1: Various currently available energy-well-to-drive-wheel chains for a transition to hydrogen use as an energy medium (adapted from [1]).....2

Figure 2: Schematic of PEMFC components and transport processes.....5

Figure 3: A typical PEMFC polarization curve that is associated with voltage losses (η).....9

Figure 4: Pressure gradient and thermal-gradient driven water transport mechanisms for liquid and vapor states, respectively. Porous gas diffusion layer and flow field are shown.....12

Figure 5: X-ray tomographic microscopy of PEMFC cathode components (GDL and BPP) operating at the current density: 0.45 A cm^{-2} [19]. Visualized components: a) BPP, GDL and all liquid water; b) GDL and all liquid water; c) The water column connecting water generation site to the droplet.....12

Figure 6: Concentration losses of oxygen during its transport from the reactant channel to the catalyst layer. Cases presented for a) fewer and b) more droplets in the channel. 14

Figure 7: Three scenarios of air velocity at the GDL-reactant channel interface depending on the relative amounts of water vapor and oxygen flux.....15

Figure 8: Air permeation into the gas diffusion layer (GDL) due to a droplet. Air suction and injection take place upstream and downstream of the droplet, respectively.....16

Figure 9: A volume-of-fluid (VOF) simulation of two-phase flow in a PEMFC air channel with structured roughness to mimic GDL surface topology. Droplet detachment dynamics and their effect on cell performance were investigated [30].....19

Figure 10: An example of a 3D wet PEMFC model that simulates the PEM, CL,GDL and serpentine reactant channels at anode and cathode sides [32]. 21

Figure 11: A PEMFC with a grooved GDL that leads to water droplets emerging from the channel center width. 26

Figure 12: Contact angle distribution on the perimeter of a droplet foot print, under conditions of: a) absence of an external force, b) presence of an external force. 28

Figure 13: Static and dynamic contact angle measurement setup utilized by several researchers in the literature. 29

Figure 14: Characterization of droplet deformation through the mismatch of droplet diameter measured in two normal axes. 30

Figure 15: A droplet emerging from a GDL into an air channel: a) No air flow in the channel; b) Air flow in the channel leads to luminescent particles creating streaklines in long exposure... 30

Figure 16: Temperature dependence of Schmidt number (Sc) for fully humidified air. 36

Figure 17: a) Geometry of a repeating pattern taken from the simulated fuel cell cathode side; b) Cross sectional view of the channel with droplet-shaped obstruction. 38

Figure 18: a) The dimensions of the simulated channel with uniformly spaced droplets; b) The dimensions for the channel and bipolar plate cross section. The bipolar plate was not simulated. 39

Figure 19: a) The dimensions of the simulated channel with uniformly spaced films; b) The dimensions for the channel and bipolar plate cross section. The bipolar plate was not simulated. 41

Figure 20: The meshed domain as the result of mesh independency study. The droplet radius is r = 0.15 mm and uniform droplet spacing Δx_d = 1.00 mm. The first droplet is moved closer to the inlet for easier demonstration. 45

Figure 21: Film dimensions, TPCLs, contact angles and conventions of positioning which are shown from a) the top (z axis) and b) the side (y axis) channel walls. (Long dashed lines: channel wall boundaries; Solid lines: TPCLs on the top and side channel wall; Dashed-dotted lines: TPCL on the GDL surface) 55

Figure 22: The Sherwood number (Sh) mesh independency study for the droplet radius r = 0.15 mm, superficial air velocity u_m = 10.59 m s^{-1}, and uniform droplet spacing Δx_d = 2.00 mm.

The position of the first droplet $x_{d,1}$ = 3.00 mm. a) Depiction of the overall Sh trend, b) A close-up view of Sh in the wake of the seventh droplet ($x_{d,7}$ = 7.00 mm) 61

Figure 23: Different film entrance types that are represented by a varying semi-principle axis, r_x while the other, r_y is kept constant. 62

Figure 24: Effect of film entrance types on local Sherwood number (x_f = 5.00 mm). 63

Figure 25: Flow over backward-facing step problem. a) Description of the problem geometry and flow conditions; b) Experimental vs. numerical comparison of velocity in the x direction (u) with respect to non-dimensionalized height (z/S). 65

Figure 26: Comparison of experimental [99] and numerical mean Nusselt number (Nu_m) at channel Reynolds number of Re_{ch} = 400.00 and the interfacial Reynolds number of Re_{int} = 20.00 (corresponding to injection). 66

Figure 27: Comparison of experimental [100] and numerical mean Nusselt number (Nu_m) at channel Reynolds number of Re_{ch} = 500.00 and the interfacial Reynolds number of Re_{int} = -5.00 (corresponding to suction). 67

Figure 28: The effect of Péclet number (Pe) on the Sherwood number (Sh) for the non-dimensional droplet radius, r^* = 0.29 (the droplet position, $x_{d,1}$=3.00 mm). 68

Figure 29: The effect of droplet spacing (Δx_d) on the Sherwood number (Sh) for two consecutive droplets at Péclet number, Pe = 174.22 and the non-dimensional droplet radius, r^* = 0.29 (the first and the second droplet positions: $x_{d,1}$ = 3.00 mm and $x_{d,2} = x_{d,1}+\Delta x_d$, respectively). 70

Figure 30: The down-the-channel-averaged Sherwood number ($Sh_{av,n}$) for the non-dimensional droplet radius r^* = 0.39, uniform droplet spacing Δx_d^* = 1.96, and Péclet number Pe = 26.16 and 69.75. 72

Figure 31: The effect of uniform non-dimensional droplet spacing (Δx_d^*) on the Sherwood number (Sh) and down-the-channel-averaged Sh ($Sh_{av,n}$) at the Péclet number, Pe = 69.75, non-

dimensional droplet radius, $r^* = 0.29$: a) Sh against the non-dimensional distance parameter ($x^* = (x - x_{d,1}) / \Delta x_d$); b) $Sh_{av,n}$ against the droplet number in the flow direction (n). 73

Figure 32: The quadratic behavior of $Sh_{av,\infty}$ with the non-dimensional radius (r^*) at the Péclet number of a) Pe = 13.16 and b) Pe = 26.16. 75

Figure 33: The linear behavior of $Sh_{av,\infty}$ with the non-dimensional radius (r^*) at the Péclet number of Pe = 121.91. 76

Figure 34: The flow conditions for the superficial mean air velocity $u_m = 10.59$ m s^{-1}, and the droplet radius, $r = 0.15$ mm. *yz* direction of the velocity is shown by arrows of which lengths are logarithmically proportional with the velocity magnitude in the *yz* cross section. Each slice is separated for 0.20 mm, and the color map corresponds to a) $+x$ velocity magnitude ($-x$ velocity areas are left blank on the slices), and b) O_2 concentration (C). 77

Figure 35: The effect of helical air flow path on local O_2 concentration profile: The Péclet number Pe = 261.42, non-dimensional droplet radius $r^* = 0.20$, non-dimensional uniform droplet spacing $\Delta x_d^* = 3.92$. a) The streamline originated at $x = 0$, $y = 0.10$ mm, $z = 0.15$ mm; b) Oxygen concentration normalized with the mean concentration (C/C_m) at a *yz* cross section from the symmetric half of the channel. C_m is 3.520 and 3.394 mol m^{-3} at $x = 0$ and 12.00 mm, respectively. 79

Figure 36: The effect of creeping air flow over the droplets on local O_2 concentration profile: The Péclet number Pe = 13.16, non-dimensional droplet radius $r^* = 0.39$, and non-dimensional uniform droplet spacing $\Delta x_d^* = 1.96$. a) Streamlines originated at $x = 0$, $0 < y < 0.70$ mm, $z = 0.19$ mm; b) Oxygen concentration normalized with the mean concentration (C/C_m) at a *yz* cross section from the symmetric half of the channel. C_m is 3.626 and 3.464 mol m^{-3} at $x = 0$ and 11.50 mm, respectively. 80

Figure 37: The comparison between O_2 concentration drop from the channel cross sectional mean value (C_m) to interfacial average one ($C_{int,av}$) at two different Péclet numbers: 26.16 and

174.22. Non-dimensional droplet radius and uniform spacing are 0.29 (0.15 mm) and 3.92 (2.00 mm), respectively. 81

Figure 38: Induced injection and suction by the droplet with a radius of r = 0.15 mm at a channel based Reynolds number of Re_{ch} = 275.15. Droplet induced injection/suction is expressed by interfacial Reynolds number (Re_{int}). 85

Figure 39: Normalized local Sherwood numbers (Sh) with the respective zero injection/suction fully developed values ($Sh_{FD,0}$). Changes induced by a droplet with a radius of 0.15 mm at channel based Reynolds number of 275.15. Comparison made between channel-only and channel-GDL simulations. 86

Figure 40: Characteristic points are shown in two scenarios of Sherwood number (Sh) profile due to a single film with zero length (L_f = 0): a) No Sh overshoot, b) Overshoot of Sh. 87

Figure 41: Characteristic points shown on a Sherwood number profile due to a single film with a length larger than zero (L_f > 0). 90

Figure 42: The comparison between dry-region-averaged (Sh) and effective (Sh_{eff}) Sherwood numbers for a film at x_f = 5.00 mm. Conditions are Pe = 69.75, W_f* = 0.78 (W_f = 0.40 mm), and L_f* = 9.80 (L_f = 5.00 mm). 94

Figure 43: Sh results for a single-film scenario and multiple-film scenarios. All results have the condition of W_f* = 0.39, L_f* = 9.80 (L_f = 5.00 mm), and Δx_f* = 9.80 (Δx_f = 5.00 mm). The first film is positioned at $x_{f,1}$ = 5.00 mm. 95

Figure 44: Comparison of numerically generated Sherwood number (Sh) and predicted Sh through correlations (Sh_{cor}) along the non-dimensional distance measured in the film wake (x_w*). a) Superimposition of Sh and Sh_{cor}, b) Ratio of Sh_{cor}/Sh. 103

Figure 45: The comparison of Sh_{eff} obtained through numerical simulations and correlations. The comparison is made for a configuration of two films that 5.00 mm apart. Their widths are $W_{f,1}$ = 0.40 mm and $W_{f,2}$ = 0.50 mm. 104

Figure 46: The applicability of Sherwood number (Sh) correlations at different length scales. The Péclet number (Pe), non-dimensional droplet radius (r^*) and uniform spacing (Δx_d^*) are 174.22, 0.29, and 3.92, respectively. Results of Sh exactly match at different hydraulic diameters (d_h) since non-dimensional variables are the same. 106

Figure 47: The ratio of correlation-predicted Sherwood number (Sh_{cor}) to numerically generated Sherwood number (Sh): Sh_{cor}/Sh. The ratio is plotted against the distance measured from the first film in the domain (x-$x_{f,1}$). At the same position different data points are presented for various Pe and W_f^* conditions. L_f^* and Δx_f^* are 9.80 (5.00 mm). 108

Nomenclature

Abbreviations

BC	boundary condition
BPP	bipolar plate
CL	catalyst layer
FD	fully developed
GDL	gas diffusion layer
ICE	internal combustion engine
MAPE	mean absolute percentage error
MPL	microporous layer
PEM	proton exchange membrane
PEMFC	proton exchange membrane fuel cell
PV	photovoltaic
TPCL	triple-phase contact line

Variables

A	area
a, b, c	coefficients of correlations
Bo	Bond number
C	molar concentration of a gas
$D_{\mathrm{O2\text{-}air}}$	molar oxygen diffusivity in air
$D_{\mathrm{O2\text{-}GDL}}$	molar oxygen diffusivity in the gas diffusion layer
d_{h}	hydraulic diameter
F	air drag force on a water feature
F_{c}	Faraday's constant
g	gravitational acceleration

H	height
h_M	mass transfer coefficient
$\mathbf{I}$	identity matrix
i	current density
J	molar consumption rate of species
j	molar flux of species
L	length
N	number of water features in the air channel
Nu	Nusselt number
Pe	Péclet number
Po	Poiseuille number
Pr	Prandtl number
p	air pressure
Q	volumetric flow rate
r	semi-principle axis length of an ellipsoid
R_u	universal gas constant
S	benchmark problem step height
Sc	Schmidt number
Sh	Sherwood number
t	gas diffusion layer thickness
T	temperature
$\mathbf{u}$	velocity vector
u, v, w	velocity components
V	voltage
W	width
We	Weber number

$\mathbf{x}$	spatial coordinate vector
x^*	non-dimensional distance in the flow direction
x, y, z	spatial coordinate components
Δx	spacing in the flow direction

Greek

α	convergence rate of Sherwood number to the asymptotic value
Γ	Gibbs free energy
η	voltage loss
Θ	entropy
θ	contact angle
λ	stoichiometric ratio
μ	dynamic viscosity of air
ξ	droplet-blocked portion of the channel cross sectional area
Π	enthalpy or non-dimensional group
ρ	air mass density
σ	air-water surface tension
τ	the number of electrons exchanged for a molecule/atom of reactant/by-product
ω	molar fraction of a species

Subscript

∞	asymptotic value
A	electrochemical activation voltage loss
ac	repetitive unit area under a channel and a land
ad	adhesion
adv	advancing contact angle

air	air
av	flow direction averaged
ch	channel
CROSS	voltage loss due to fuel cross over
D	drag force along the flow direction
d	droplet
eff	effective
f	Film
FD	fully developed
H2O	water
k	type of species or index of discrete position
in	inlet
int	interfacial
land	bipolar plate land width between two channels
m	mean
max	maximum value in the water feature wake
n	water feature number in the flow direction
O2	oxygen
R	resistive voltage loss
rec	receding contact angle
rev	reversal voltage loss
side	side wall of the channel
st	static contact angle
sat	saturation
T	thermal transport related
TH	thermal cell voltage

top	top wall of the channel
x	flow direction specific
wet	droplet-covered portion of the GDL-channel interface

Superscript

*	non-dimensional
T	transpose

CHAPTER 1. INTRODUCTION

1.1. HYDROGEN ENERGY

Reduction of greenhouse emissions and utilization of renewable energy are among the current objectives of transportation industry. These objectives bear critical importance in addressing environmental pollution and relying excessively on fossil fuels. Today, one third of the greenhouse emissions are due to transportation [1]. Under these circumstances, internal combustion engine (ICE) powered vehicles are aimed to be transformed into zero tailpipe emission vehicles in the future. Developing countries, such as the US and Europe have been encouraging the achievement of this aim [2]. Currently, hybrid passenger cars are available in the market. These cars generate electricity through an ICE and then, either store the electrical energy or utilize it for mechanical propulsion [3]. Since these cars proved to offer a more efficient utilization of fossil energy, the electrical motors are foreseen to be used in the future products as well.

Reduction of greenhouse emissions to an ideal level of zero can be achieved by reengineering the entire energy-well-to-drive-wheel (well-to-wheel) chain. The well-to-wheel emissions include feedstock extraction and transport, fuel production, fuel storage, transport and delivery, and evaporative emissions during refueling [1]. The next generation vehicles should be based on an energy source which will lead to the maximum reduction of emissions in all links of the well-to-wheel chain. Fuel cell vehicles using hydrogen potentially offer the lowest emissions for the entire well-to-wheel chain and the widest range of primary energy supply possibilities compared to any alternative [1]. In addition to these advantages, the vehicle design is simpler since there are no moving parts. However, the fuel supply infrastructure is required to be more complex especially for a transition period from gasoline to hydrogen energy. As a transient solution, cars are available with onboard fuel processors to transform conventional energy sources, such as gasoline or diesel, into hydrogen. However, studies show that cars with onboard hydrogen storage

are simpler in design, less costly, and more energy-efficient compared to the ones with an onboard fuel processor [4]–[9]. Therefore, fuel cell cars with onboard storage are favored in long term and there is a variety of transition pathways as the primary energy source.

The ultimate goal of hydrogen energy utilization is to establish a link between clean energy sources (wind, solar, and nuclear) and transportation industry. With this link established, greenhouse emissions can be brought to an almost zero level. Before the full utilization of clean energy resources, there are projected transition steps to the use of hydrogen energy. Figure 1 shows possible pathways to transition into hydrogen energy. Some of these pathways are already readily utilized, such as oil, natural gas, and coal. By using these available pathways, the following reductions in greenhouse emissions can be achieved: Emissions can be reduced at most by 50% with gasoline or diesel based ICE hybrids compared to conventional ICE cars [1]. If hydrogen is produced from steam reforming of natural gas, which is the most widely used technique currently to produce hydrogen, emissions can be reduced down to the one fourth of the conventional ICE cars [1]. If the carbon dioxide sequestration is used along with steam reforming of natural gas, one twentieth of the ICE emission can be achieved [1].

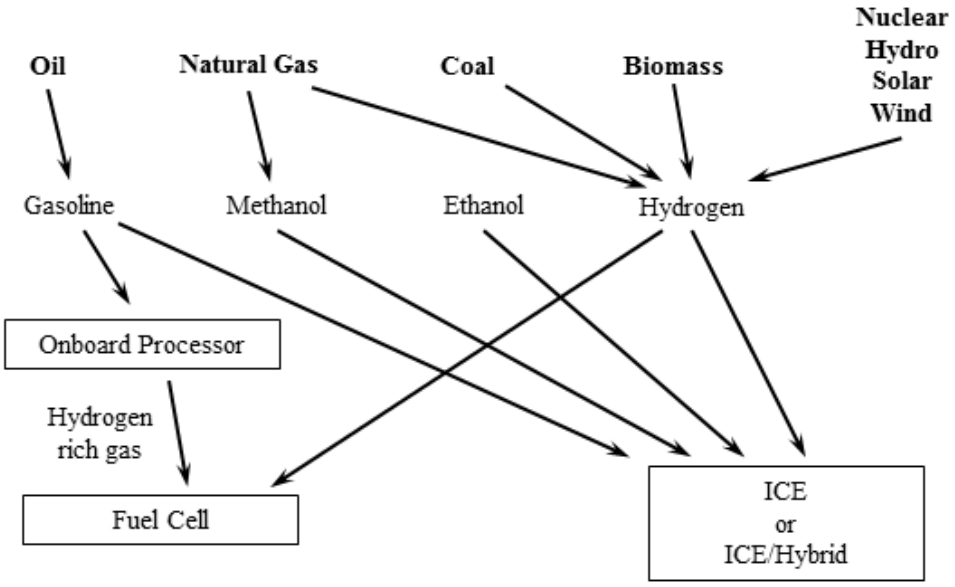

Figure 1: Various currently available energy-well-to-drive-wheel chains for a transition to hydrogen use as an energy medium (adapted from [1]).

Various clean energy sources can be listed as wind, solar (also known as: photovoltaic (PV)), nuclear, and decarbonized fossil sources which are achieved by capturing and secure sequestrating of carbon dioxide during hydrogen production [1]. Among them, some are renewable and hence, preferred to nuclear or decarbonized fossil sources. However, renewable sources such as wind and PV have not completed their technological evolution yet to be commercially competitive. Solar energy through PV technology can power a car up with a 25 m^2 collection area (based on average US insolation) [1]. However, PV technology requires a high initial financial investment by individuals and this challenge is currently aimed to be addressed by large scale fuel stations [1]. Biomass and wastes can also contribute to the transition to hydrogen energy. The biomass from two third of the US idle cropland could power all cars up via hydrogen [10]. Moreover, the gasification of municipal solid waste can power the 25 to 50% of the metropolitan cars up in the US [11].

Hydrogen utilizing fuel cells, also known as proton exchange membrane fuel cells (PEMFCs), need to be engineered to a level that they are commercially competitive in the ICE vehicle market. The commercialization of fuel cells for cars is expected to happen until 2015 by the brands: Toyota, Honda, Hyundai, Daimler, and General Motors (GM) [12]. For the cost of a fuel cell to be reduced, there are fundamental research areas on fuel cell operation. Some of these areas can be listed as material science, electrochemistry, heat/mass transfer and micro/nano fluidics. The present work focuses on the coupled problem of mass transfer and micro fluidics.

1.2. INTRODUCTION TO PEMFCs

Proton exchange membrane fuel cells (PEMFCs) convert chemical energy stored in the bonds of hydrogen molecules into electrical energy. Converting energy into useful work gives fuel cells the name, engine [13]. Oxygen in air is used as the oxidizer for the hydrogen. Rearrangement of the bonds leads to usable electrical energy, waste heat that can sometimes be utilized, and by-product water that replaces greenhouse gases.

PEMFCs operate at higher efficiencies (60% for only electrical energy conversion, and 80% for overall conversion to electrical and usable heat [12]) than internal combustion engines [14]. This efficiency is achieved by the absence of moving parts and so, the direct conversion of chemical energy to electrical energy [14]. Moreover, the absence of moving parts provides more reliability, longer life time and noiseless operation [14]. The byproducts of PEMFC are water and heat that are environmentally friendly.

1.2.1. Components

A PEMFC consists of sandwiched layers that serve diverse purposes. A single cell cannot provide enough power for most of the applications. Cells are connected in series to increase the net voltage difference while current density remains constant. Therefore, a cell stack can provide more electrical power. The working principles for a single cell remain constant for the stack configuration. It is more convenient to introduce the cell components on the schematic of a single cell than a stack of cells. As demonstrated in Figure 2, these components are proton exchange membrane (PEM), catalyst layer (CL), gas diffusion layer (GDL) and bipolar plate (BPP).

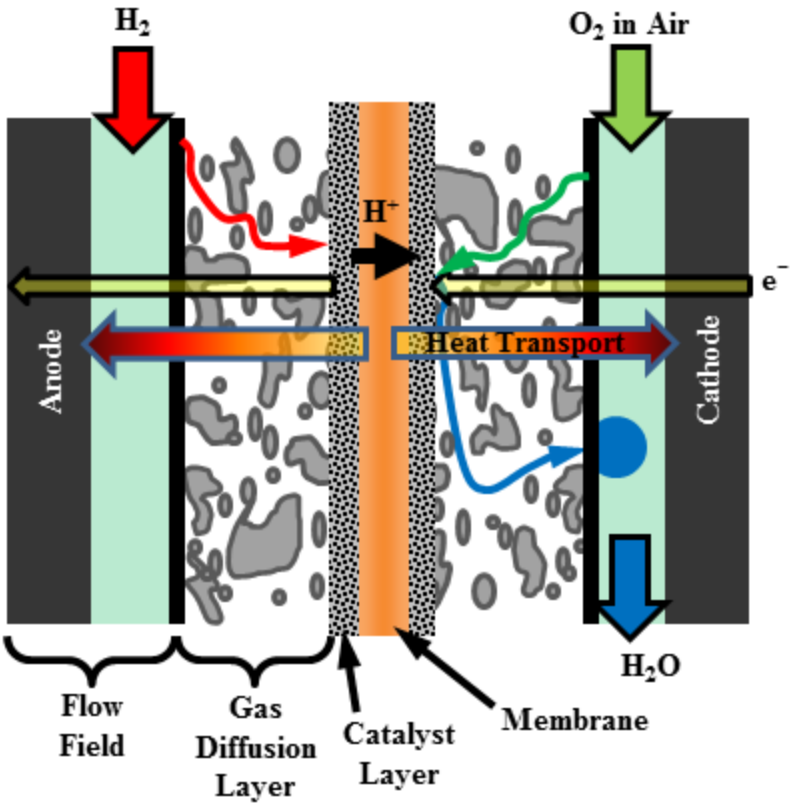

Figure 2: Schematic of PEMFC components and transport processes.

Proton Exchange Membrane (PEM): The main objective of this component is to transfer the hydrogen protons (H^+) generated at the anode catalyst layer (CL) to the cathode CL. Meanwhile, the membrane should prevent the transport of any other species. The membrane consists of a hydrophobic and inert polymer structure that is sulfonated with hydrophilic acid clusters to provide proton conductivity [13]. Hydration of the membrane is required for proton conductivity. Hydration can be achieved through the presence of liquid water by the membrane. However, the amount of hydration should be optimized to prevent dehydration and water flooding in the adjacent layers. The typical thickness of a PEM can range between 18-25 μm and the PEM can resist temperatures up to 120 °C [13]. However, their operational temperatures do not exceed 90 °C [13] to ensure sufficient hydration.

Catalyst Layer (CL): The major role of this component is to provide electrochemically active sites for half reactions to take place. At the reaction sites, ions, reactants, and byproducts

are transported. This layer is a 3D porous structure with a typical thickness of 5-30 μm [13]. The porosity of CL is in between 0.4 and 0.6 [13] that is aimed to be increased for less resistance to mass transport. In order to reduce the electrical resistance, carbon and catalyst particles are bonded together. The ionomer has a fraction up 30% [13] to promote ion transport to/from the PEM. The removal of excess water is another issue to be considered because the CL mostly consists of hydrophilic materials. The hydrophilicity is balanced out by the partial use of hydrophobic polytetrafluouroethylene (PTFE).

Gas Diffusion Layer (GDL): This major role of this component is the uniform reactant transport to CL from the reactant channels and the product water removal from CL to reactant channels. This layer is made of either woven carbon cloth or nonwoven fiber paper as the macroporous layer, and a highly hydrophobic microporous layer (MPL) [13]. The thickness of GDL can range between 175 and 450 μm [13]. The hydrophilic carbon constituent leads to the possibility of water flooding that is prevented by the use of PTFE additive. Electron conduction to/from CL takes place through GDL. The electron resistivity for a given direction is dependent on the GDL type and PTFE content. Additionally, GDL transfers heat from the heat generation sites (CL and PEM) to the bipolar plate (BPP). The thermal conductivity is dependent on the PTFE fraction. Lastly, it provides mechanical support for PEM.

Microporous layer (MPL) is a complementary layer of the GDL. It is 5-20 μm thick and it has 100-500 nm pores [13]. MPL is used for water management because it is highly hydrophobic. In addition to water management, it is used to improve electrical conductivity between the CL and GDL, and prevent CL from carbon fiber intrusion damage caused by GDL.

Bipolar Plate (BPP): This plate accommodates reactant channels that are together called flow field (FF). This plate supplies the reactants and interconnects cells in stack electrically. It also provides the exhaust of non-consumed reactant and by-product water (gas or liquid state), structural integrity and dissipation of waste heat. In a fuel cell stack, each BPP side has a different reactant because these sides correspond to the anode and cathode of two different fuel cells which

are adjacent to each other at this particular BPP. As a result of the cell connections in series, a particular BPP is the anode and the cathode of two neighboring cells. It has a minimum thickness of 2 mm [13] which is much larger than the characteristic thicknesses presented for other components. The flow field may consist of parallel or serpentine channels. Serpentine configuration imposes a given air flow rate and hence, any water feature in the channel is discharged for whatever cost of pressure drop [15]. On the contrary, parallel channels are connected to the same manifold. Hence, a water feature in a channel can create flow resistance and the flow through the blocked channel can be directed to other parallel channels. Although parallel channels require less pressure drop than serpentine channels, they are prone to flow maldistribution [15].

1.2.2. PEMFC Operation Principles

The fuel (hydrogen) and oxidizer (oxygen in air) are introduced into the cell through the anode and cathode flow fields, respectively. While the reactants run through the flow fields, they diffuse through their respective GDL and reach CL where the electrochemical reactions take place. The global reaction and the half reactions taking place at the CLs are:

$$\text{Global: } 2H_2 + O_2 \rightarrow 2H_2O \quad (1)$$

$$\text{Anode: } 2H_2 \rightarrow 4H^+ + 4e^- \quad (2)$$

$$\text{Cathode: } 4e^- + 4H^+ + O_2 \rightarrow 2H_2O \quad (3)$$

Electrochemically active areas of the CLs provide enough activation energy for the half reactions to take place. Each half reaction leads to a total change in enthalpy ($\Delta\Pi$) and entropy ($\Delta\Theta$). These changes are documented for the global reaction and used to calculate the maximum extractable electrical energy from the system, namely the change in Gibbs free energy ($\Delta\Gamma$). It is expressed for a constant temperature (T) and pressure (p) conditions as:

$$\Delta\Gamma = \Delta\Pi - T\Delta\Theta \quad (4)$$

A typical performance measure of a fuel cell at steady state is the polarization curve. Figure 3 shows a typical polarization curve that plots the voltage (V) versus current density (i). In Figure 3, sections are identified to show the major sources of voltage loss (η). Although the sections are affiliated with a certain type of voltage loss, most of those regions are still under the partial effect of other voltage losses.

If all of the chemical energy in hydrogen could be transferred into electrical energy, the resulting electrical energy would equal to the change in enthalpy during the reaction ($\Delta\Pi$). The open circuit voltage (V_{OC}) obtained in this hypothetical condition is named thermal voltage (V_{TH}). As the first source of voltage loss and heat dissipation, $T\Delta\Theta$ in Eq. (4) is an inevitable one due to the nature of the energy conversion system. This loss is called reversible (η_{REV}) or Peltier loss. The thermodynamic terms in Eq. (4) are not exactly known for half reactions. Therefore, the distribution of the reversible losses to the anode and cathode sides has not been obtained yet.

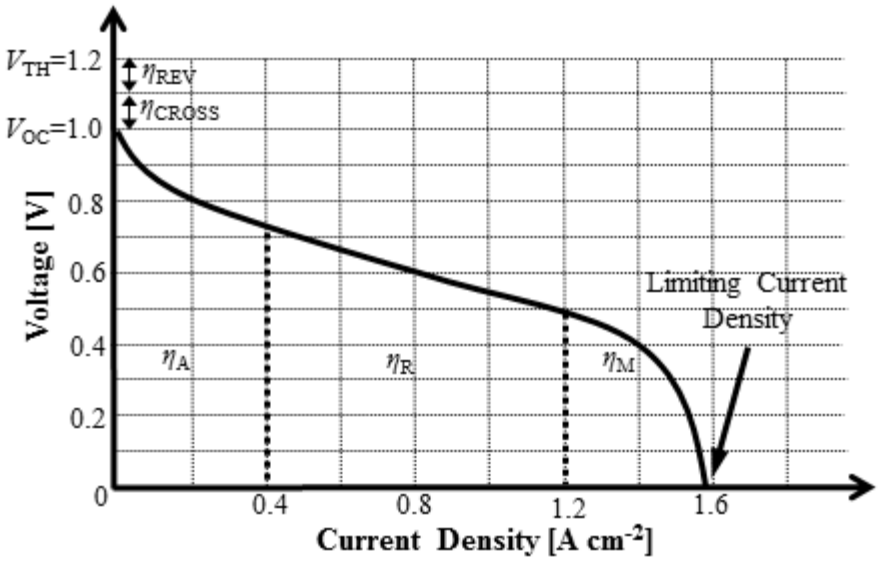

Figure 3: A typical PEMFC polarization curve that is associated with voltage losses (η).

As the cell departs from the open circuit voltage, the electrons and protons are forced to displace due to the voltage difference between the CLs. The cathode always has a higher absolute voltage than the anode. This voltage difference is at its maximum during the open circuit condition. As the system operates at higher currents densities, the absolute voltages of cathode and anode are decreased and increased, respectively. This change leads to a smaller voltage difference between them as the current density increases. The loss of the voltage difference is used as the activation energy at the CLs and named as the activation loss (η_A). The activation loss also incorporates the effect of fuel cross over through the membrane. The fuel cross over loss (η_{CROSS}) is itemized separately only in the open circuit voltage condition when the activation loss is zero.

The hydrogen protons (H^+) and electrons are subjected to ohmic resistance that leads to ohmic voltage loss (η_R). Since the proton resistance dominates over the electron resistance, this loss is mostly indicative of PEM proton conductivity. The proton conductivity of the PEM is reported to be dependent on how much hydrated it is [13]. The uniform distribution of conductivity can be disrupted by water transport processes in PEM. The water diffuses into PEM from the adjacent layers and hydrates it. Additionally, the water molecules are transported along

with hydrogen protons during cell operation [13]. This causes a water flux in the direction of proton transfer, namely from the anode to the cathode. This process is called electro-osmotic drag and is responsible for putting the anode side of PEM under the danger of dehydration. The diffusion and electro-osmotic drag of water counteract to each other and their net effect can be interpreted through the ohmic losses.

In addition to the proton conductivity of PEM, electron conductivity of the remaining layers plays a minor role in ohmic losses. The contributors to electron resistance are the CL, GDL, BPP, and the external load circuit. The last contributor to the ionic and electronic resistances is contact resistance between the layers, and it is due to the imperfect contact of two dissimilar materials.

As the current density approaches the limiting current density, the dominating voltage loss is the reactant transportation limitation or concentration loss (η_M). As the current density increases, the reactant concentration difference between the flow field and the CLs has to become larger to sustain the required reactant flux. However, the reactant concentration in the flow field is constant for a given point and the concentration at the CL can be reduced to as low as zero. Under these circumstances, the available maximum concentration difference limits the maximum attainable current density. When the reactant concentration at the CL is low, the CL spends more energy to incorporate the scarcely available reactants into the reaction. This loss manifests itself in the high current region of a cell in the form of a dramatic voltage drop. This proposal focuses on the concentration losses taking place on the cathode side for the oxygen transport since the anode side losses are negligible comparably.

1.2.3. Two-Phase Flow in PEMFC Components

The by-product water in a PEMFC is produced at the cathode CL. Depending on the thermal condition of the cell, the water is partially in liquid state and the rest is in vapor state. As the thermal conditions change locally within the cell, the vapor can condense in the porous medium,

GDL. The liquid and vapor states of water are transported from CL to reactant channels through different ways.

The vapor transport in the cathode GDL is governed by the concentration gradient of vapor in the air. This gradient is due to the higher vapor concentration at CL with respect to the reactant channel. The higher vapor concentration at CL does not necessarily stem from the aforementioned water production. As shown in Figure 4, the heat generation at PEM and CLs creates a higher temperature at the cathode CL with respect to the cathode reactant channels. The temperature gradient from CL to reactant channels leads to a vapor concentration gradient even when the air is fully humidified everywhere in the cell. Since the water saturation pressure increases non-linearly with the temperature, the air can carry significantly more vapor as temperature increases. Hence, the vapor transport in fuel cell porous medium can be mostly called thermal-gradient-driven. The transported vapor leaves the GDL from its reactant channel interface as shown in the center section of Figure 4.

The water vapor transport can lead to condensation as local temperatures or thermal gradients decrease. In the areas of condensation, the condensed water keeps fulfilling the pores of GDL. The GDL temperature in the immediate vicinity of BPP lands is always lower than the one at the reactant channel interface. The cooling provided by the BPP can access the GDL more easily through the BPP lands than the reactant channel since the BPP lands have a lower thermal resistance than the air-occupied channels. Under these circumstances, vapor transport leads to more condensation under the BPP lands than the channel interface [16], [17]. Condensation sites in a GDL form a water column originated from the water generating CL. The border of this water column towards the reactant channel is called condensation front. This front occurs in the GDL due to a need of pressure build-up for the liquid water column to break through a microscale and hydrophobic GDL pore [18]. Two columns of liquid water can be seen in Figure 4 with their fronts adjacent to BPP lands.

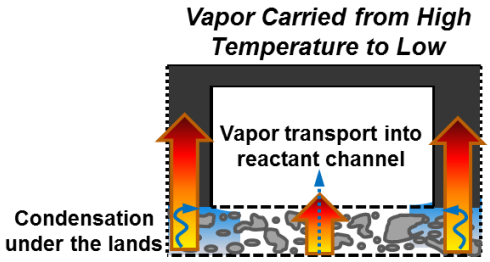

Figure 4: Pressure gradient and thermal-gradient driven water transport mechanisms for liquid and vapor states, respectively. Porous gas diffusion layer and flow field are shown.

The water transport mechanisms affect the distribution of liquid water in the GDL. These mechanisms can be demonstrated through the visualization of the GDL liquid water distribution in an operational PEMFC. Figure 5 shows images of X-ray tomographic microscopy from a cell operating at 0.45 A cm^{-2} [19]. Vapor transport leads to condensation consistently underneath the BPP lands. Liquid water broke through the GDL into the reactant channel in the form a droplet. The droplet that emerge into the channel can later grow or coalesce with other and form more complex liquid water features such as films or slugs that will be discussed in the consequent sections.

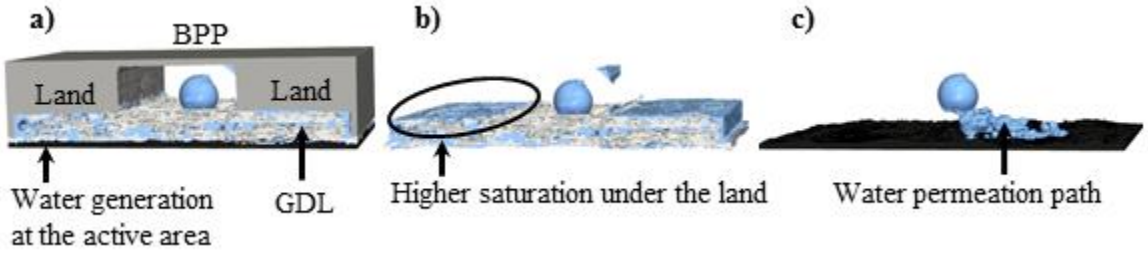

Figure 5: X-ray tomographic microscopy of PEMFC cathode components (GDL and BPP) operating at the current density: 0.45 A cm^{-2} [19]. Visualized components: a) BPP, GDL and all liquid water; b) GDL and all liquid water; c) The water column connecting water generation site to the droplet.

1.2.4. Transport of Oxygen in a PEMFC

The concentration of oxygen at the cathode CL affects the cell voltage for a given current density. Although hydrogen concentration at the anode CL is a parameter on the performance, it

is less of a concern compared to the oxygen concentration owing to the higher diffusivity of hydrogen than oxygen. Oxygen concentration at the cathode CL is a function of concentration losses distributed from the air channel to the CL. These losses are located at GDL-channel interface, GDL, and GDL-CL interface. They depend on liquid water occupancy of the porous media. Hence, knowing the capacity of vapor removal through the porous media is important to predict the condensation in the pores and so, the oxygen concentration drops.

Oxygen concentration decreases along the flow direction in the channel due to continuous oxygen consumption. In order to minimize the variation of oxygen concentration in the flow direction, air flow rate is set to a value that provides more oxygen than to be consumed per unit time. The ratio of the volumetric air flow rate at the channel inlet to the volumetric air consumption is called stoichiometry (stoichiometric ratio). Most frequently, stoichiometry is set to be two in most PEMFC applications. At a stoichiometry of two, the oxygen concentration would reach half of its original value from the channel inlet by the channel outlet.

The cross sectional mean oxygen concentration at a given point in the air channel first goes through an abrupt drop at the GDL-channel interface and then followed by a continuous decrease within the GDL. These losses of oxygen concentration are shown in Figure 6. For vapor transport, the vapor concentration will vary with the opposite trend: higher concentration at the CL and lower concentration at the channel. Since the objective is to highlight the relative importance of the GDL-channel interfacial oxygen resistance with respect to the one of the GDL, the interfacial GDL-CL resistance is not presented here.

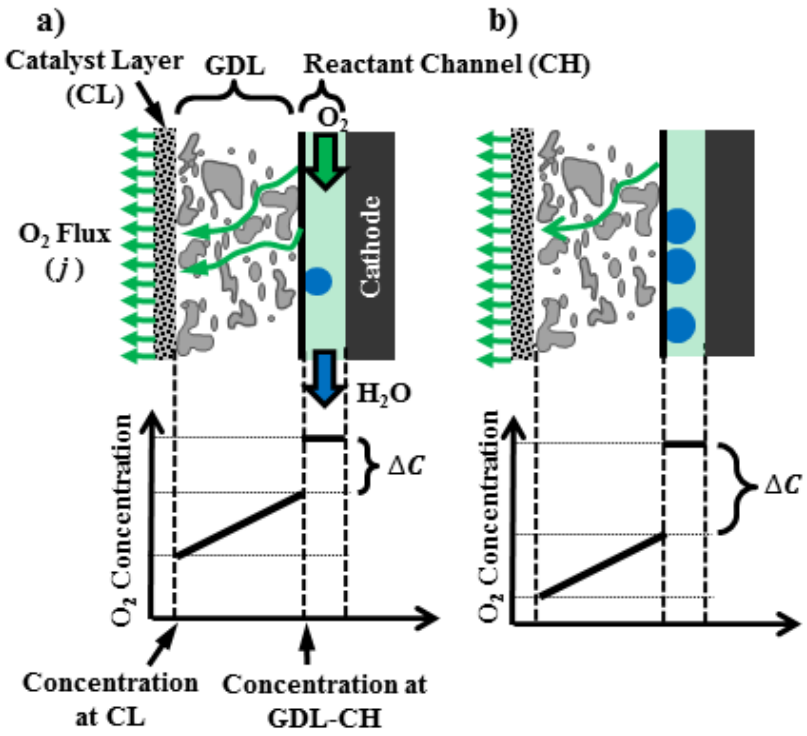

Figure 6: Concentration losses of oxygen during its transport from the reactant channel to the catalyst layer. Cases presented for a) fewer and b) more droplets in the channel.

The effect of two-phase flow in the reactant channel on the interfacial oxygen concentration drop is demonstrated by the comparison of Figure 6a and Figure 6b. The larger number of droplets in the channel covers a larger portion of the GDL-reactant channel interface. Hence, a larger concentration drop occurs. The variation of concentration drop is not only dependent on the area coverage of the interface by the droplet. Since the droplet changes the local air flow conditions, the transport resistance at the interface needs to be investigated.

1.2.5. Oxygen Transport Resistance at the GDL-Air Channel Interface

The oxygen concentration in the cathode air channel is expressed as the cross-sectional mean value for a given position in the flow direction. This mean concentration decreases abruptly at the GDL-channel interface as the fuel cell consumes oxygen through the porous GDL. The amount of concentration drop is proportional to the flux of oxygen. The ratio of oxygen flux to the concentration drop is called mass transfer coefficient (h_M). This parameter is dependent on

oxygen diffusivity in the air (D_{O_2-air}) and hydraulic diameter (d_h). The mass transfer coefficient is non-dimensionalized with the aforementioned parameters into Sherwood number (Sh) which is independent of the parameters. Sherwood number is only dependent on the channel cross sectional aspect ratio and the boundary condition of mass transfer.

Possible scenarios of boundary condition are demonstrated in Figure 7. Both side walls and the top wall do not contribute to mass transfer. The bottom GDL-channel interface is subjected to oxygen flux. There are three possible conditions that can be seen at the interface during oxygen flux. Air may flow into or out from the interface, or the air may have zero velocity at the interface. Air flow into the interface is referred to as suction, while the flow out from the interface is injection.

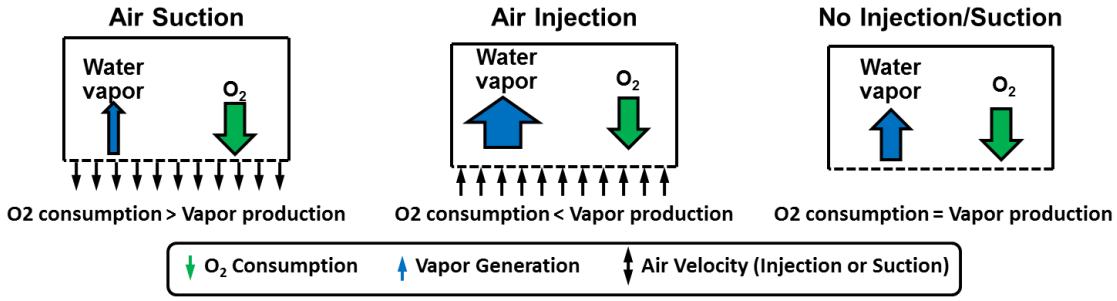

Figure 7: Three scenarios of air velocity at the GDL-reactant channel interface depending on the relative amounts of water vapor and oxygen flux.

The relative amount of vapor and oxygen fluxes at the interface determines what air velocity the GDL-channel interface will have. If all by-product water is in liquid state, the interfacial air velocity will be dominated by the inward oxygen flux and this would result in air suction. If all by-product water is in vapor state, vapor exhaust can overpower the oxygen consumption and this would result in air injection. At conditions that vapor and oxygen fluxes are the same, the net air flow velocity becomes zero. As the boundary condition changes due to variable oxygen and vapor fluxes, Sherwood number can be affected and needs to be investigated.

Under fully developed flow conditions in the channel, Sherwood number remains constant. However, water features in the channel disrupts the fully developed flow. As they do so, a part of

the flow can permeate into the GDL adjacent to the channel as shown in Figure 8. In conditions like this oxygen flux at the GDL-air channel interface (j_{O2}) has advective ($j_{O2,dif}$) and diffusive components ($j_{O2,dif}$) as shown in Eq. (5). The advective transport takes place at the interface with a velocity of w_{int} and O_2 concentration of C_{int}. Diffusive transport is a function of mass transfer coefficient (h_M) and the difference between the mean O_2 concentration in the channel (C_m) and C_{int}. In a simulation approach of neglecting the GDL and just simulating the channel, advective transport at the interface is assumed to be zero. Simulations that incorporate the GDL can reveal the comparison of $j_{O2,adv}$ with respect to $j_{O2,dif}$.

$$\begin{aligned} j_{O2} &= j_{O2,adv} + j_{O2,dif} \\ &= w_{int}C_{int} + h_M(C_{int} - C_m) \end{aligned} \tag{5}$$

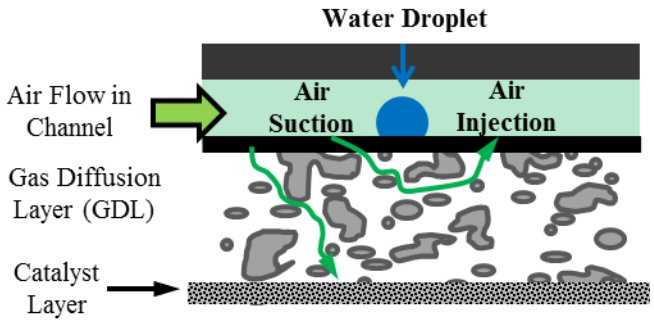

Figure 8: Air permeation into the gas diffusion layer (GDL) due to a droplet. Air suction and injection take place upstream and downstream of the droplet, respectively.

Under these conditions, the variation in Sherwood number is not known and needs to be investigated. Therefore, PEMFC performance models can incorporate the Sherwood number as a function of two-phase flow conditions. For Sherwood number to be investigated under two-phase flow, water features in reactant channels and their effects on cell performance should be characterized.

CHAPTER 2. BACKGROUND

2.1. TWO-PHASE FLOW DEPENDENT FUEL CELL PERFORMANCE

The performance of a PEMFC is investigated in the literature as a function of the liquid water in its reactant channels. Experimental and numerical studies are utilized to reveal the two-phase flow impact on the cell performance.

2.1.1. Experimental Evidences of Performance Variations

Fuel cell experimentations mostly demonstrate the effect water slugs that plug the channels on cell performance [20]–[23]. It is frequently observed that as the current density is reduced, liquid water coverage in the channels increases [24]–[27]. This can be explained with the consideration of the following facts: Superficial air velocity and water production rate depend on the current density linearly. The drag force applied by the air flow on a water feature depends on the superficial air velocity quadratically. The quadratic dependence is due to the fact that the order of magnitude for a typical Reynolds number in the reactant channel is two. The volume of liquid water in channel increases with current density. The adhesion force of water features grows linearly with the feature size. Therefore, the adhesion of water features increases linearly. Linear and quadratic dependencies of water feature adhesion and the drag forces, respectively explains the reason of observing water features mostly at low current densities.

The two-phase flow patterns are affected by current density which controls superficial air and liquid water velocities. The dominant flow pattern makes a transition from droplets to films and then to slugs as the current density is reduced [25], [26]. These transitions affect how the GDL-reactant channel interface is covered. Slugs completely block the channel. If the air flow rate is kept constant at the blocked channel, the air flow is directed into the GDL and underneath the slug. Although this significantly increases pressure drop required to drive the same flow rate, the reactants would reach the CL directly rather than diffusing from the interface. Hence, the transport resistance at the GDL-reactant channel interface becomes irrelevant to the convective

transport of air to the CL. This scenario is representative of serpentine reactant channels. In the case of parallel reactant channels connected to the same manifold, a slug in a channel can block the air flow to the respective channel completely. The air supplied from the manifold is redistributed to the unblocked parallel channels [28]. Since air convection is not present in the blocked channel anymore, mass transport cannot happen from that channel to the CL. In this case, interfacial resistance is irrelevant again. Therefore, interfacial resistance should be investigated for droplet and films but not for slugs.

The air flow can coexist with films and droplets in a channel. Some of the GDL-air channel interface remains unblocked and subjected to mass transfer. The interfacial transport resistance increases along with the reduction of interfacial area. Moreover, these water features alter the local flow conditions and change the way air flow interacts with the GDL-channel interface. Hence, Sherwood number is expected to change locally. The change in Sherwood number should be characterized to understand the effect of films and droplets on the cell performance.

2.1.2. Numerical Evidences of Performance Variations

Numerical studies investigate how the variation of O_2 resistance affects the cell performance. Compared to experimental studies, numerical studies can reveal the impact of varying O_2 resistance more clearly since they compare a channel with single-phase gas flow assumption and another channel with a realistic two-phase flow. Ding et al. simulated a 3D air channel with two-phase flow and the channel was coupled with a 1D membrane electrode assembly model at the GDL-air channel interface [29]. The effect of water slugs on the cell performance was studied. It was showed that slugs can increase the O_2 transport resistance and decrease the cell voltage at current densities higher than 0.6 A cm^{-2}. At a current density of 0.8 A cm^{-2}, the average cell voltage was shown to drop from 0.6 V to 0.35 V that represent single and two-phase flow cases, respectively. The adverse impact of the slugs on the performance is significant. This work can be complemented by extending the investigation to droplets and films.

The effect droplet and films on cell performance was numerically studied by Chen et al. [30]. In their model, they simulated an air channel (0.28 mm × 0.34 mm × 2.00 mm) and a GDL as 3D domains, and a cathode CL as a boundary on the GDL. Figure 9 presents the simulated domains and a typical instant of droplet detachment. Compared to the model of Ding et al. [29], simulating the porous GDL in 3D allowed the air to permeate into the GDL in the flow direction in case of a droplet obstructing the flow. The cell was simulated at a voltage and average current density of 0.5 V and 1.92 A cm^{-2}. It was shown that the permeation of air flow under a sliding droplet on the interface can increase the local current density. The average current density was shown to increase 10 mA cm^{-2}. Moreover, a film at the top channel wall (across the GDL-channel interface) could also increase the local current density as it directs the air flow towards the GDL-channel interface. However, the positive and local impact of the film is not significant enough to increase the average current density. In order to complement the studies by Ding et al. [29] and Chen et al. [30] revealing the effects of two-phase flow patterns, there is a need to characterize the local interfacial O_2 resistance for PEMFC operating conditions.

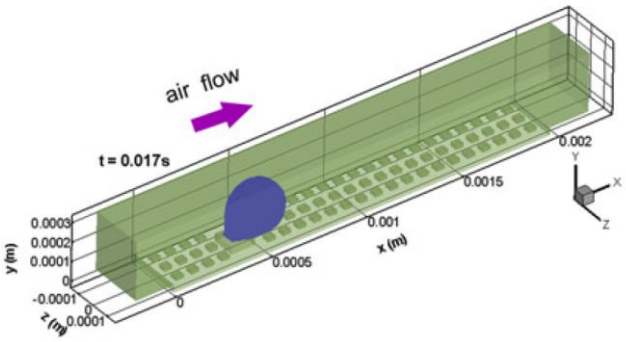

Figure 9: A volume-of-fluid (VOF) simulation of two-phase flow in a PEMFC air channel with structured roughness to mimic GDL surface topology. Droplet detachment dynamics and their effect on cell performance were investigated [30].

2.2. CONSIDERATIONS OF INTERFACIAL MASS TRANSPORT RESISTANCE IN PEMFC PERFORMANCE MODELING

2.2.1. Models Implicitly Solving for the Interfacial Resistance

In numerical models of PEMFCs, GDL and reactant channels should be simulated together for the interfacial oxygen transport resistance to be calculated and incorporated into the results. Fluid flow and mass transport equations should be solved in these domains. In these models, the computational requirements become significantly demanding compared to the ones omitting the simulation of flow in reactant channels. The advantage of simulating the reactant channel is that they can simulate the interfacial phenomena with higher fidelity to reality since the GDL and channel are coupled. Although these models simulate the interfacial transport resistance, this phenomenon is incorporated into the performance prediction results implicitly and the resistance values are not reported explicitly.

There is a wide range of 3D wet PEMFC modeling studies which incorporated the full solution of gas flow in PEMFC flow fields along with electrochemistry equations [31]–[41]. Figure 10 shows an example 3D meshed domain for a PEMFC model [32]. This numerical model incorporates the anode and cathode sides. Two reactant channels on each side represent a portion of serpentine flow fields. However, the bents of the serpentine flow fields were neglected in this model and flow switched direction as it advances in the vertical direction. The meshed domain shows that the reactant channels require a significant number of mesh elements. Hence, the complexity of the cell model is increased significantly to simulate the channels.

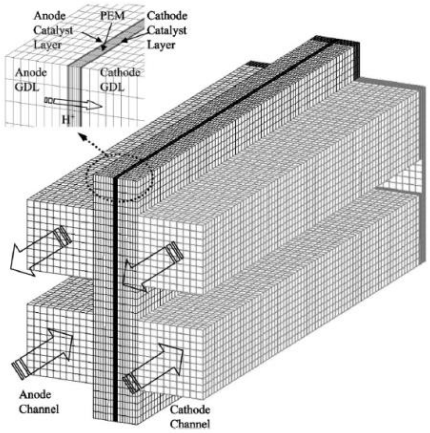

Figure 10: An example of a 3D wet PEMFC model that simulates the PEM, CL,GDL and serpentine reactant channels at anode and cathode sides [32].

Most of the cited 3D wet PEMFC numerical models treated the two-phase nature of water with a mixture fluid approach [31]–[35], [37]–[41]. The transport in the PEMFC was assumed to be governed by a single mixture fluid which is a weighted average of gasses and liquid water. All material properties for fundamental governing equations are calculated with this two-phase mixture model. This technique leads to continuously changing material properties in the two-phase water regions. In reality the material properties change abruptly through two-phase boundaries. However, this condition brings the requirement of tracking two-phase boundaries and thereby, the identification of the corresponding material properties at a given point. Since two-phase boundary tracking is computationally costly, the two-phase mixture model was developed as an alternative [42]. However, this model was later critiqued by not being able to capture the two-phase water transport phenomenon in the GDL coupled with the GDL-reactant channel interface [43]. With this limitation related to the GDL-reactant channel interface, the cited 3D wet models obtained polarization curves, local current densities, species concentration and temperature distributions. Although these models solved for the liquid water in porous components of the cell, such as the GDL, CL and PEM, they had to neglect the effects of liquid water in the reactant channels since the channels are not porous and consequently, mixture model

could not be applied. Moreover, these studies did not report the mass transport resistance which was implicitly solved in the numerical models.

2.2.2. Models Incorporating the Interfacial Resistance as an Input Parameter

In the literature, simplified PEMFC models utilize the Sherwood number as a constant input to save computational resources from the simulation of forced convection in the air channels [44]–[57]. The constant input of Sherwood number is a valid assumption if the flow is fully developed in the reactant channels, such as the absence of liquid water features in high temperature PEMFCs [54]. However, the constant Sherwood number assumption is not always applicable. Kim et al. shared a similar anticipation that the Sherwood number might depend on specific fuel cell operating conditions and configurations [47]. Casalegno et al. [52] in 2010: "The correlations to determine the Sherwood number in the two-phase flow conditions, …, are not available in the literature.".

2.3. INVESTIGATION OF INTERFACIAL MASS TRANSPORT RESISTANCE

2.3.1. Utilization of Heat and Mass Transport Analogy

For a fully developed (FD) flow condition, the heat and mass transfer analogy is applicable, and Sh is equal to the Nusselt number (Nu). Hence, established Nu values can be used as Sh in PEMFC air channels with no limitations as long as the flow is fully developed. The heat and mass transfer analogy has been utilized by several researchers for the fully developed condition [52], [54], [58]. However, Nu-Sh mapping cannot always be easily performed in an air channel since liquid water features in the channel may not allow the flow to be fully developed. In developing flow conditions, Sh and Nu can be the same only if the respective Schmidt (Sc) and Prandtl (Pr)

numbers are the same. In case Sc and Pr are different from each other, the mapping between Sh and Nu should be investigated for specific cases in the PEMFC air channel.

With the use of Sh_{FD}, a preliminary calculation can be made to show the relative importance of interfacial O2 transport resistance with respect to the resistance through the GDL. For the air channel cross section in interest in this study (0.70 mm × 0.40 mm), using the heat and mass transfer analogy leads finding the value of Sh_{FD} to be 3.349. Based on the technique that will be presented in Section 5.1.1.5. , the concentration drop at the interface and through the GDL is calculated to be 0.65 and 0.33 mol m^{-3}, respectively at the current density of 1.5 A cm^{-2}.

2.3.2. Simulation of the Interfacial Transport Resistance

Since the research on the Sherwood number in PEMFC reactant channels has not yet been very well established, only a few numerical simulations are available in the literature. These studies have 2D (parallel plates) and 3D approaches. The results by the 2D models do not reflect realistic results due to fact that PEMFC reactant channels typically have an aspect ratio close to unity. All these studies investigated the effect of air injection/suction at the GDL-air channel interface on the Sherwood number. Depending on the intensity of suction or injection, the flow may remain developing in the channel. Under developing flow conditions, the Sherwood number can vary and hence, has been a subject of investigation.

Both 2D and 3D studies showed a negligible effect of air injection and suction on Sherwood number. 2D numerical studies by Wang et al. [59], Jeng et al. [60] and Hassanzadeh et al. [61] obtained the fully developed Sherwood number values as 5.274 (readjusted Sh with dh instead of the channel height, 6.0, and 5.411, respectively. Only Beale has published results for 3D channels with varying cross sectional aspect ratio [62], [63]. In these publications, Sherwood number was reported in the form of mass transfer driving force. Correlations were established for a wide range of injection/suction intensity and channel aspect ratio. Beale concluded that Sherwood number is not affected by injection and suction conditions in typical PEMFC operating conditions[62].

These findings allow the simulations to neglect any injection or suction at the GDL-reactant channel interface. However, the previous studies neglected the effect of liquid water present in the channel on the Sherwood number.

2.4. REACTANT CHANNEL TWO-PHASE FLOW PATTERNS

In order to study the effect of liquid water features on Sherwood number, visual characterization of the water features is required. After characterizing the shape, size, and motion of the water features, these features can be incorporated into simplified models as obstructions to single-phase gas flow without the need of simulating the complex two-phase flow. The liquid water present in the reactant channels can be characterized through visible-light-transparent PEMFC designs. These are called in-situ experiments since they use an operational fuel cell. The use of visible light provides high spatial and temporal resolution compared to other options, such as X-ray radiography, neutron radiography, and magnetic resonance imaging [64].

In order to control the two-phase flow conditions more accurately, operational fuel cells are transformed into ex-situ experiments that introduce the liquid water into reactant channels through artificial injection [26], [65]. Moreover, there are dedicated fundamental microfluidics studies on droplets, films, and slugs [66]–[71].

2.4.1. In-Situ Visualization of Two-Phase Flow

The two-phase flow visualization in operational PEMFCs has been conducted to observe changes in flow conditions locally in the cell and in response to varying operating conditions. Tüber et al. conducted one of earliest visualization studies by the use of a PEMFC that is as wide as a single reactant channel [55]. Kimball et al. [23] and Dillet et al. [22] experimentally correlated the motion of slugs and changes in local current density.

Different designs of flow fields are experimented with transparent PEMFCS to reveal how the two-phase flow in each flow field design affects the cell performance. Sugiara et al. compared parallel and serpentine channels [72]. The parallel channels were found to suffer from flow

maldistribution. Moreover, flooding water volume for the channels was reported as a figure of merit for flow field designs. Masuda et al. compared flow field designs of single and three parallel, and three serpentine channels [21]. The designs are compared through pattern of voltage fluctuations due to two-phase flow.

In-situ experiments are utilized to establish correlations for the movement of an individual water feature. Yang et al. [73] and Ous and Arcoumanis [74] experimented with PEMFCs utilizing multiple parallel channels and a serpentine channel, respectively. These works mostly focused on droplets and their patterns of growth and departure. Zhang et al. used a PEMFC with multiple parallel channels [75]. They observed droplets, films and slugs. They also built a correlation for the droplet detachment diameter for the tested range of superficial air velocities. Spernjak et al. used serpentine channels and varied the temperature [76] They reported that the superficial gas velocity of 7.4 m s^{-1} led to droplets readily detached in channels with the cross section 0.8 mm × 1.0 mm. Zhan et al. showed that liquid water is removed easily for air velocity larger than 7 m s^{-1} in a channel cross section of 1.5 mm × 1.5 mm [24].

Liquid water features cover the GDL-reactant channel interfacial area and lead to the decrease of cell performance. This area coverage is characterized by in-situ studies to predict the portion of cell performance loss due to mass transport resistance at the interface. Hussaini and Wang identified flow patterns in multiple parallel channels and discussed their effects on the cell performance [27]. They defined a parameter called area coverage ratio which is the visualized area of liquid water in the reactant channels divided by the total GDL-channel interfacial area. The value of ACR was obtained by manual image processing. Lastly, they obtained a flow pattern map as a function of superficial gas and liquid velocities. Nishida et al. used an automated image processing tool to characterize droplet sizes seen on the GDL [77]. Sergi and Kandlikar obtained the area coverage ratio to express the presence of films and slugs by the use of automated image processing tool [25].

The local air flow conditions in the vicinity of a droplet are altered as a function of droplet emergence location along the channel width. It is known that droplets mostly emerge from under the bipolar plate (BPP) lands (ribs) [16], [17]. However, there are studies suggesting that this does not always have to happen. Optical visualization studies documented that the droplets can emerge in the center of the channel width [27], [73], [75], [77], [78]. It was hypothesized that a GDL with a smaller porosity would lead to a droplet emergence more uniformly distributed along the channel width rather than concentrated underneath the BPP lands [79]. As shown in Figure 11, it was proposed to have a groove in the GDL at the channel center width and along the flow direction to create a preferential droplet emergence location and hence increase the cell performance [80]. Based on these observations, droplets can emerge from the channel side wall-GDL corner and GDL-channel interface center width.

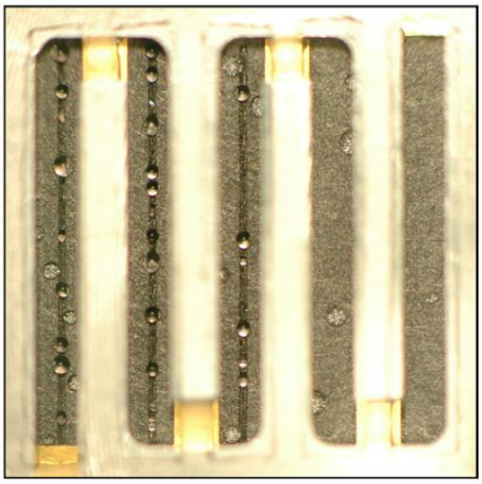

Figure 11: A PEMFC with a grooved GDL that leads to water droplets emerging from the channel center width.

2.4.2. Ex-Situ Visualization of Two-Phase Flow

Ex-situ setups aim to simulate two-phase flow in PEMFC reactant channels by artificially introducing liquid water into PEMFC flow fields through GDLs. By this way the random interactions between water features and air flow are simulated. They are separated from

fundamental experiments by not focusing on a specific water feature but the overall result of water features-air flow interaction.

Le et al. used a serpentine channel design for ex-situ testing and simulating the two-phase flow numerically [65]. The liquid water was injected through a single pore in the vicinity of air channel inlet. The areas prone to flooding were identified. The experimental and numerical results agreed well. Banerjee and Kandlikar used a parallel channel flow field with variable temperature and relative humidity [26]. Similar to a previous study [25], the area coverage ratio was quantified in terms of films and slugs. As an additional contribution, this ratio was quantified at each channel separately. In all values temperature and relative humidity, area coverage ratio decreases consistently with equivalent current density. For a constant current density, the area coverage ratio was observed to decrease with temperature and relative humidity.

2.4.3. Fundamental Experimental Studies on Two-Phase Flow Patterns

Fundamental studies focus on the motion of two-phase flow pattern components, such as a droplet, film, and slug. These studies attempt to recreate the conditions that a water feature would be subjected to in a fuel cell and understand how the water feature behaves when one variable is changed at a time.

Fundamental studies on droplets attempt to answer the question of when droplets detach from the porous GDL surface. In order to provide this answer with proper reasoning, the researchers observe the perimeter of the droplet foot print (gas-liquid-solid). At this perimeter, changes of contact angle are observed as a function of angular position (α). When the droplet is at steady-state without the influence of an external force as shown in Figure 12a, the contact angle (θ) at the droplet contact line is constant. The surface tension due to gas-liquid interface (σ) has a component that is in the plane of the solid (GDL). This constant surface tension distribution creates a zero net force on the aforementioned plane and leads to zero force on the droplet. The aforementioned contact angle is the static contact angle (θ_{st}).

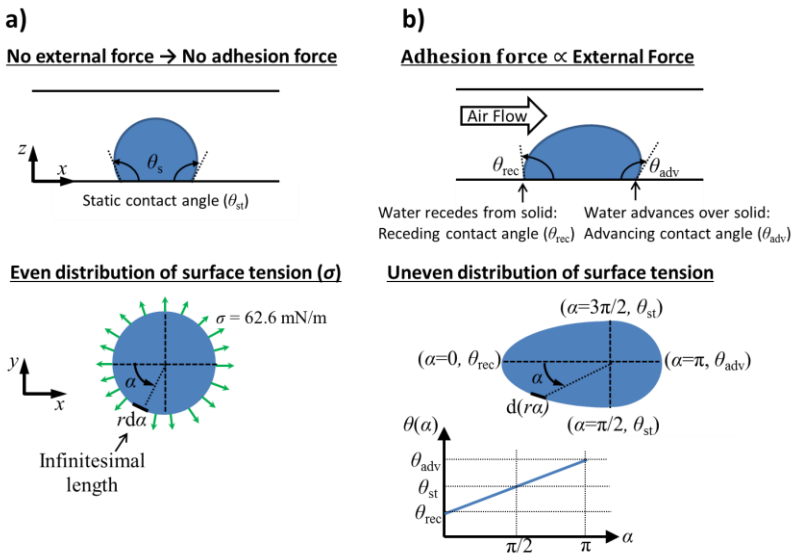

Figure 12: Contact angle distribution on the perimeter of a droplet foot print, under conditions of: a) absence of an external force, b) presence of an external force.

The contact angle of a droplet varies when it is subjected to external forces as shown in Figure 12b. The adhesion force of the droplet to the solid as a reaction force is dependent on how non-uniform the contact angle distribution will be at the droplet foot print perimeter. The non-uniform distribution of contact angle leads to a non-zero net force on the solid plane. The droplet foot print can be divided into two halves. The half that is further to the direction of external force has a contact angle larger than the static contact angle. The maximum value of contact angle on this side is called advancing contact angle (θ_{adv}). On the other half of droplet footprint, the contact angle values become smaller than the static value. The minimum contact angle on this side is called the receding contact angle (θ_{rec}). The adhesion force of the droplet increases with the difference between advancing and receding contact angles. This difference is called contact angle hysteresis.

Gauthier et al. measured contact angle hysteresis when the droplet is reacting to an external force when it is stationary and sliding on the surface [81]. They have shown that contact angle hysteresis is different in static and dynamic conditions. Static contact angle hysteresis can be

measured as in Figure 13 by the help of a tilted surface with a droplet placed on it. Once the tilt angle exceeds the threshold value and droplet starts to accelerate, the dynamic contact angle hysteresis can be measured. Static contact angle hysteresis for carbon paper was shown to be larger than the dynamic one.

Das et al. measured the droplet deformation under gravity and measured the force to initiate sliding in static conditions [70]. The droplet deformation under gravity was reported to be negligible for Bond number (Bo) values under 0.1. Moreover, static contact angle hysteresis and the resulting adhesion force were measured at various GDL samples, including aged ones.

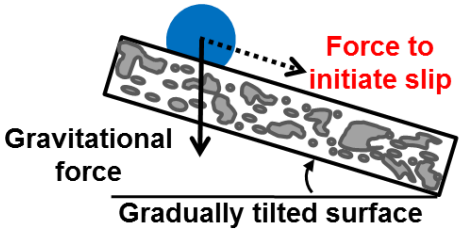

Figure 13: Static and dynamic contact angle measurement setup utilized by several researchers in the literature.

Droplets in a channel are deformed due to the air flow around them. The deformation increases proportional to the intensity of air flow inertia, hence the superficial air velocity. Cho et al. experimentally correlated this droplet deformation [82], [83]. The deformed shape can be expressed as an ellipsoid with a semi-major axis of r_x and a semi-minor axis r_y. The mismatch between the two semi-principal axes is normalized with the average droplet radius $(r_y - r_x) / r$ as shown in Figure 14.

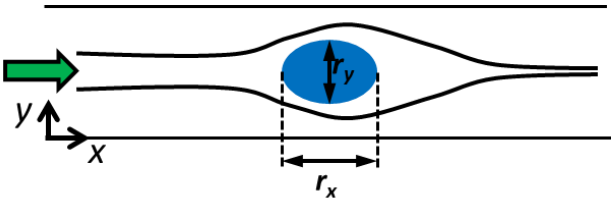

Figure 14: Characterization of droplet deformation through the mismatch of droplet diameter measured in two normal axes.

The droplet in an air flowing channel has a recirculation inside due to shear forces acting on the droplet-air interface. By characterizing this recirculation, the velocity at the droplet-air interface can be extracted. Minor et al. used micro digital particle image velocimetry technique to quantify droplet internal circulation [84]. Figure 15 shows the droplet in the absence and presence of air flow with the use of particle image velocimetry technique. In a channel cross section of 1 mm × 3 mm, the maximum superficial air velocity was 6.000 m s^{-1} which corresponded to a channel based Reynolds number of 580. The maximum velocity in the droplet was recorded to be 0.105 m s^{-1} which is 1.75% of the superficial air velocity. Hence, droplet surfaces under air flow can be assumed to have zero velocity.

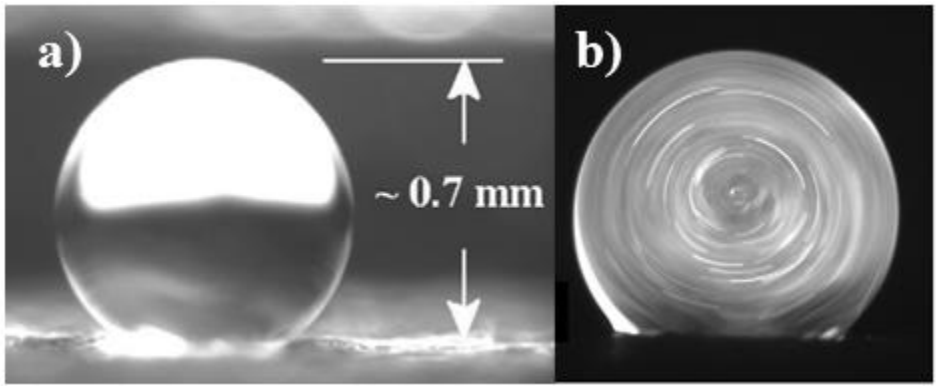

Figure 15: A droplet emerging from a GDL into an air channel: a) No air flow in the channel; b) Air flow in the channel leads to luminescent particles creating streaklines in long exposure.

The evolution of a droplet into a film and then a slug was investigated by Colosqui et al. [85]. It was reported that a droplet attaches to the channel corner due to perturbations by the air flow. The droplet in contact with the channel corner can grow into long films without detaching. The

volumes of the slugs formed were correlated with superficial air and water velocities. Cheah et al. [86] expanded on the work of Colosqui et al. [85] by experimenting with different channel surface energies and cross sections. The following understanding was shared as a result of the experiments: The mass transport losses increase with slug length. However, a slug divided into smaller compartments will need more energy to be removed since there is more interfacial area to create adhesion due to surface tension forces.

Ody has concentrated on the components of reaction forces applied by a traveling slug in a channel [87]. The reaction forces in response to a pressure difference across the slug were shown to consist of viscous dissipation within the slug and surface tension forces resulting from contact angle hysteresis. It was shown that the viscous dissipation starts to dominate the surface tension forces as slug velocity increases. The author established a range of Capillary number which is a non-dimensionalized way of expressing slug velocity to differentiate viscous dissipation and surface tension dominated cases.

CHAPTER 3. OBJECTIVES

The objective is to obtain oxygen transport resistance at the GDL - air channel interface under two-phase flow conditions. The transport resistance is expressed with the non-dimensional Sherwood number and needed in simplified PEMFC performance models. Two-phase flow conditions refer to the presence of water droplets and films. Characterization of Sh in the vicinity of water droplets and films can lead to more accurate predictions in the performance models. Sherwood number needs to be characterized as a function of distance along the flow direction, water feature size, spacing, and fuel cell operating conditions, such as current density, stoichiometry, temperature, and relative humidity. Numerical simulations should be used to obtain local variations of Sh with the aforementioned parameters. The results should ultimately be expressed through mathematical correlations that can be conveniently used by PEMFC performance models. This main objective can be divided into smaller components as below:

3.1. OBTAINING THE TRENDS OF SHERWOOD NUMBER AS A FUNCTION OF DROPLET AND FILM CONFIGURATION BY USING NUMERICAL SIMULATIONS

This study aims to minimize the computational cost of simulating the effect of droplets and films on Sherwood number. For doing so, it is proposed to use obstructions shaped like water features to partially block the single-phase air flow in a channel. The use of obstructions requires the knowledge of water feature shape, detachment conditions, and water-air boundary conditions.

Fundamental microfluidics studies already documented the shapes of droplets and films under air flow that is equivalent to conditions in PEMFC air channels. These shapes can be approximated in a simulation through the sum/subtraction of basic geometrical shapes, such as spheres, cylinders, and rectangular prisms.

Since the numerical models are targeted to be steady-state, adhesion of water features subjected to air flow needs to be ensured. Force of adhesion for a water feature is already

provided in the literature. By comparing the adhesion force from the literature to the drag forces numerically computed, only cases that lead to water feature adhesion can be simulated.

At the interface between air and water, the fluid velocity needs to be known to impose the proper boundary condition on the water feature obstruction. In reality, air flow and water within the droplet are coupled in motion. Since the use of obstructions decouples the motion of two-phases, experimental documentation of droplet internal recirculation needs to be utilized.

3.2. BUILDING CORRELATIONS FOR SHERWOOD NUMBER

The results of Sherwood number in the vicinity of water features are expected to show trends with the variables to be simulated. The aim is to build non-dimensional mathematical correlations to be used in simplified PEMFC performance models. These correlations should reflect the changes in the flow direction and operating conditions. Separate correlations needs to be built for droplets and films. These correlations should be in non-dimensional for them to be used at a wider range of conditions and length scales. These correlations can be used along with the visualization data of operational PEMFCs. The statistical distribution of water features in a channel can indicate where to use the Sherwood number correlations. Therefore, the correlations should be built to be comprehensive enough for the possible visualization outcomes.

3.3. EXPANDING THE USE OF SHERWOOD NUMBER CORRELATIONS

The numerically obtained Sherwood number should be applicable to a range of temperature relative humidity, and their combinations. The temperature and relative humidity affect the air Schmidt number (Sc) for which Sherwood number is specific. Therefore, it is easier to study the effect of temperature and relative humidity through varying Schmidt number. By investigating the sensitivity of Sherwood number on Schmidt number, the variation of Sherwood number within cell operating conditions will be predicted.

Sherwood number results for oxygen can be applicable to vapor transport. The Schmidt number for vapor transport will be different than oxygen transport. The sensitivity analysis of Sherwood number on Schmidt number can also provide a prediction on how different oxygen and vapor Sherwood numbers are.

CHAPTER 4. APPROACH

4.1. PHYSICAL MODEL

The air properties were kept constant in the simulations and calculated at the temperature (T) and relative humidity (RH) of 80 ^{o}C and 100%, respectively. The density (ρ) and dynamic viscosity (μ) of the air were calculated from the correlations provided by Tsilingiris [88]. The diffusivity of oxygen in the air ($D_{O2\text{-}air}$) was approximated based on the molar-averaged diffusivities of major air constituents within each other [89]: oxygen, vapor, and nitrogen. The constituent molar fractions and diffusivities were calculated with correlations by Mench (saturation pressure of vapor) [13] and Fuller et al. [90], respectively. With the use of the aforementioned air properties, Schmidt number ($Sc = \mu \rho^{-1} D_{O2\text{-}air}^{-1}$) was calculated for a temperature range from 0 to 80°C. Table 1 shows all the air properties mentioned above as a function of temperature.

Table 1: Properties of fully humidified air for the temperature range from 0 to 80°C: mass density (ρ), dynamic viscosity (μ), and Schmidt (Sc) number.

T [°C]	ρ [kg m^{-3}]	μ [μPa s]	$D_{O2\text{-}air}$ [cm^2 s^{-1}]	Sc
0	1.293	17.157	0.174	0.762
20	1.194	17.958	0.200	0.753
40	1.100	18.374	0.227	0.735
60	0.987	18.034	0.262	0.699
80	0.828	16.253	0.310	0.632

Fully humidified air properties in Table 1 appear to change significantly with temperature. Figure 16 also shows the trend of Schmidt number with temperature. As the molar fraction of vapor is reduced at lower temperatures, the change of Schmidt number with temperature is also reduced. Therefore, the low temperature fully humidified air properties closely approximate low temperature dry air properties. In order to simulate the impact of Schmidt number on Sherwood number in a computationally inexpensive way, air density and viscosity were always kept

constant at 80°C while oxygen diffusivity in the air was varied. This change corresponds to the cumulative effect of changes in air density and viscosity, and oxygen diffusivity. The details of this method will be presented in Section 5.3.

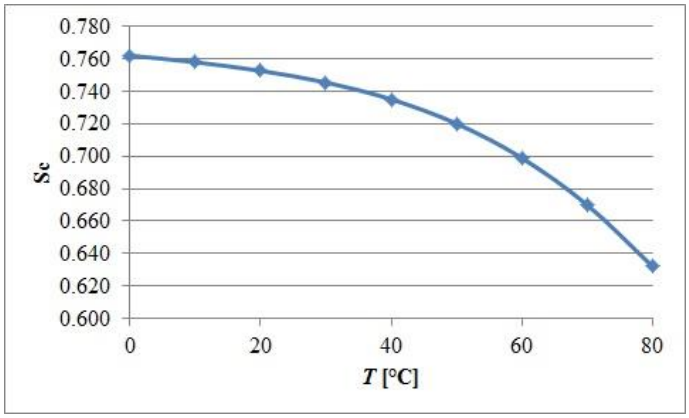

Figure 16: Temperature dependence of Schmidt number (Sc) for fully humidified air.

The investigation of Sherwood number was numerically conducted in an isolated air channel with single-phase air flow and water-feature-shaped obstructions inside. These obstructions will be called droplets or films for convenience in the following text. The effect of conjugate air flow through the channel and the gas diffusion layer (GDL) was also numerically simulated by incorporating a GDL to the channel with water features. Figure 17 shows the channel and flow field (FF) dimensions. The electrochemically active area (A_{ac}) is a repeating pattern that covers the width of the GDL-air channel interface and a bipolar plate land (rib) width. The land width (W_{land}), channel width (W_{ch}), and channel height (H_{ch}) were taken to be 0.50 mm, 0.70 mm, and 0.40 mm, respectively [91]. The active area length (L_{ac}) was taken as 183.00 mm [91] for calculating boundary conditions. These dimensions were taken from the parallel flow field study to meet the U.S. Department of Energy performance targets [91].

Figure 18a and Figure 19a respectively show multiple droplets and films placed in a row in the channel and numbered in the flow direction. The number of water features (N) varied based on the uniform droplet and film spacing (Δx_d and Δx_f, respectively). This led to a variable

simulated channel length (L_{ch}). In order to comply with the computational limitations, N was selected high enough for the results not to differ significantly in the flow direction by the last water feature.

A minimum distance from the channel inlet to the water feature and from the water feature to the channel outlet was enforced. The first water feature was placed 63.00 mm downstream of the channel inlet ($x_{d,1} = x_{f,1}$ = 63.00 mm) to obtain a fully developed flow upstream. The minimum distance between the last water feature and the channel exit was kept 10.00 mm to allow the secondary flows in the wake of the last water feature to be simulated. The water features cover a portion of the GDL-channel interface width (W_{wet}).

4.1.1. Geometric Configuration for Droplet-GDL-Channel Conjugate Simulations

The conjugate simulations of air flow through a channel, GDL, and around a droplet present benchmark cases for other simulations that neglect the GDL and injection/suction effects. In the domain presented in Figure 17, two types of investigations were conducted: i) how injection and suction applied to the bottom surface of GDL affect the Sherwood number in the channel with no water features; ii) how the air permeation into GDL due to a droplet affects the local Sherwood number.

No droplet obstruction was used for objective (i). For objective (ii), a single droplet was used. The droplet was represented with a sphere that had the radius (r) and placed at the center width of the channel ($y_d = W_{ch}/2$). The sphere was truncated to obtain the desired static contact angle on the GDL, $\theta_{st,GDL}$ = 147°. The contact angle was selected as a representative value of the GDL characterized by Gopalan and Kandlikar [69] and Das et al. [70].

The GDL properties were taken to represent Toray TGP-H 120^{TM}. The thickness (t_{GDL}), porosity (ε_{GDL}), and permeability (K_{GDL}) of the GDL were taken as 200 μm, 0.8, and 10^{-11} m^2, respectively. Oxygen diffusivity in the GDL ($D_{O2\text{-}GDL}$) was $D_{O2\text{-}GDL} = D_{O2\text{-}air}/1.5$ [13].

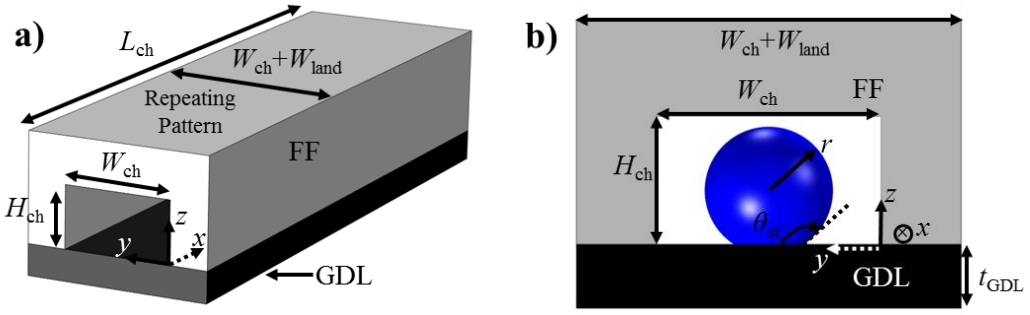

Figure 17: a) Geometry of a repeating pattern taken from the simulated fuel cell cathode side; b) Cross sectional view of the channel with droplet-shaped obstruction.

4.1.2. Geometric Configuration for Droplet Simulations

The effect of droplets was investigated with three different scenarios: single, two, and multiple droplet studies. Each provided a different understanding: In single-droplet studies, the entire wake region of a droplet was analyzed. The second droplet was placed close enough to the former droplet to obtain the interaction between them. The wake region analysis from single-droplet simulations suggested an appropriate range of distance for the second droplet. Two-droplet studies showed how much downstream of the first droplet remains the same in single and two-droplet simulations. Hence, the level of interaction between two droplets was quantified and then, the need for multiple-droplet studies was justified. Multiple droplet studies investigate the evolution of Sherwood number in the flow direction as the droplets continuously alter the air flow.

Droplets were constructed in the same way presented in the previous section. The number of droplets in a channel (N) was varied in different case studies. The value of N can be inferred from the names of the single and two-droplet cases. In multiple-droplet studies, N was 11 for the uniform droplet spacing values of 1.00 and 2.00 mm, and it was 5 for 5.00 mm. The droplets were centered along the channel width ($y_{d,n} = W_{ch}/2$). Since droplets were centered, the simulation domain allowed the use of a symmetry plane to save computational resources.

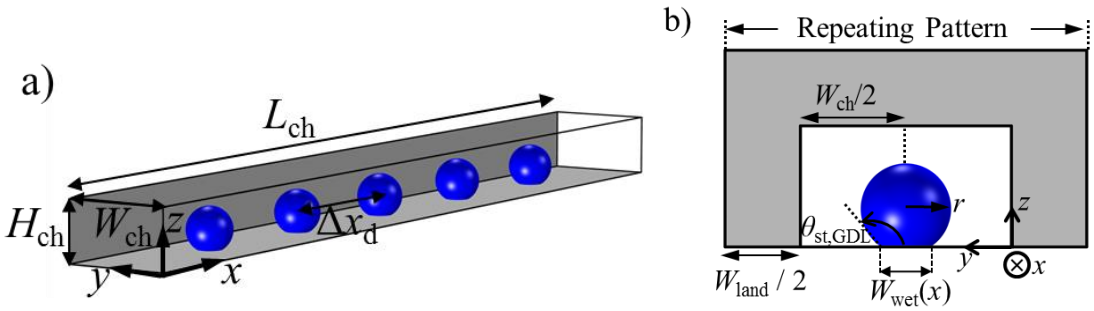

Figure 18: a) The dimensions of the simulated channel with uniformly spaced droplets; b) The dimensions for the channel and bipolar plate cross section. The bipolar plate was not simulated.

4.1.3. Geometric Configuration for Film Simulations

The effect of films was studied in the scenarios of single and multiple films. In multiple film simulations, consecutive films were placed on alternating sides of the channel ($y_f = 0$ and $y_f = W_{ch}$). None of the film scenarios led to a computational domain that can be divided by a symmetry plane, unlike the droplet cases. Hence, the entire problem geometry was simulated.

Each film was built out of the following basic geometrical shapes: spheres, cylinders, and a rectangular prism. This allows a convention to define the film shape and dimension. The built geometry was subtracted from the rectangular-prism-shaped channel to simulate single-phase air flow as in the droplet cases. Figure 19a demonstrates the building components of a film. In the flow direction, the end sections of the first film are made out of a sphere placed under a cylinder (oriented in the z direction). The sphere and cylinder share the same radius (r) which also defines the film width (W_f) as shown in Figure 19b. The width of a film (W_f) indicates the largest distance that the film covers on the top channel wall along the direction of channel width. The middle section of the film is made out of a cylinder (oriented in the x direction) placed under a rectangular prism. The length of this section (L_f) corresponds to the film length. As the length goes to zero, the film becomes a droplet at the channel corner.

The position of a film (x_f) refers to the center position of the first sphere used down the channel direction. Figure 19a presents an example of the first film position down the channel

direction ($x_{f,1}$). The uniform spacing between the films (Δx_f) is measured from the centers of the two closest spheres corresponding to neighboring films.

These films are numbered in the flow direction with the variable, n. The Sh profile changes in the flow direction and ultimately merges into a repeating pattern after a certain number of films. The total number of films (N) was selected to be large enough for the results not to differ significantly in the flow direction by the last film. It was found that the required number of films for the Sh profile to merge into a repeating pattern is dependent on Δx_f. Hence, N was selected based on each value of Δx_f.

Minimum distances from the channel inlet and channel outlet to the respective closest water films were enforced. The first water feature was placed 65.00 mm downstream of the channel inlet ($x_{f,1}$ = 65.00 mm) to obtain a fully developed flow upstream. The minimum distance between the last film and the channel exit was kept at 10.00 mm to allow the secondary flows in the wake of the last film to be completely simulated.

The spheres and the cylinder which were in contact with the GDL-air channel interface were truncated in such a way that the apparent static contact angle ($\theta_{st,GDL}$) is 147°. The GDL contact angle was selected as a representative value of the GDLs characterized by Gopalan and Kandlikar [69] and Das et al. [70]. Graphite was selected as the channel wall material. The advancing and receding contact angles on a graphite plate were measured to be 85° and 61° respectively [69]. The static contact angles on the graphite channel side ($\theta_{st,side}$) and top walls ($\theta_{st,top}$) were assumed to be 90°. The static angles were used to generate the film-shaped obstructions. The advancing and receding angles were used to calculate the contribution of side and top walls to the film adhesion force. The film width and the aforementioned static contact angle on the GDL leads to an interfacial width coverage ($W_{wet}(x)$) as defined in Eq. (6).

$$W_{\text{wet}}(x) = \begin{cases} \left(x_{\text{f},n} \le x \le x_{\text{f},n} + L_{\text{f}}\right) \rightarrow W_{\text{f}} \cos\left(\pi \dfrac{\theta_{\text{st,GDL}} - 90°}{180}\right) \\ \text{Else} \rightarrow 0 \end{cases} \quad (6)$$

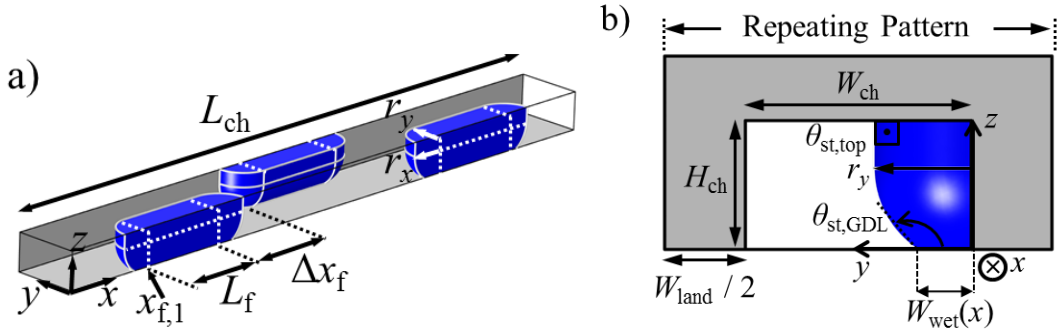

Figure 19: a) The dimensions of the simulated channel with uniformly spaced films; b) The dimensions for the channel and bipolar plate cross section. The bipolar plate was not simulated.

4.2. VARIABLES AND THEIR NON-DIMENSIONALIZATION

The objective of this work is to find the oxygen concentration drop (ΔC) for a given magnitude oxygen flux (j) at the GDL-air channel interface. Non-dimensional variables are used to reduce the number of simulations and obtain correlations that are applicable to a wider range of conditions. The non-dimensionalization is initially going to be introduced within the context of the multiple droplet problem and then applied to the multiple film problem as well. All dependent and independent parameters for this problem with a constant channel aspect ratio are ρ, μ, Δx_{d}, $D_{\text{O2-air}}$, r, u_{m}, d_{h}, ΔC, and j. These parameters were non-dimensionalized by using the Buckingham Pi Theorem [92]. It was aimed to obtain Sherwood number as one of the Π groups. This was possible by choosing the following repeating parameters: d_{h}, ΔC, $D_{\text{O2-air}}$, and ρ. The resulting set of Π groups were Schmidt number ($\text{Sc} = \mu\, \rho^{-1}\, D_{\text{O2-air}}^{-1}$), non-dimensional droplet radius ($r^* = r\, d_{\text{h}}^{-1}$), non-dimensional droplet spacing ($\Delta x_{\text{d}}^* = \Delta x_{\text{d}}\, d_{\text{h}}^{-1}$), Péclet number ($\text{Pe} = d_{\text{h}}\, u_{\text{m}}\, D_{\text{O2-air}}^{-1}$), and Sherwood number ($\text{Sh} = j\, d_{\text{h}}\, \Delta C^{-1}\, D_{\text{O2-air}}^{-1}$).

In the multiple film problem, some variables change names such as non-dimensional droplet radius (r^*) and spacing (Δx_d) become non-dimensional film width (W_f) and spacing (Δx_f), respectively. Additionally, a new variable of non-dimensional film length (L_f^*) is introduced.

For the numerical evaluation of Sh, the local oxygen transport resistance is calculated at every point on the GDL-air channel interface. For a given j, the corresponding transport resistance is ΔC which is the difference between the O_2 concentration at interface ($C_{int} = C(z=0)$) and the mean value at a channel cross section (C_m). This resistance is expressed with the mass transfer coefficient (h_M) which is a component of the Sherwood number definition.

$$h_M(x,y) = \frac{j}{\Delta C} = \frac{j}{(C_m - C_{int})} \tag{7}$$

$$C_m(x) = \frac{\int_{\substack{\text{Channel} \\ \text{cross section}}} C u \mathrm{d}A}{\int_{\substack{\text{Channel} \\ \text{cross section}}} u \mathrm{d}A} \tag{8}$$

In simulations, h_M is zero at the portion of the GDL-channel interface covered by a water feature: $W_{wet}(x)$. An effective mass transfer coefficient ($h_{M,eff}$) was defined to have an assigned value of h_M everywhere on the interface ($z = 0$).

$$h_{M,eff}(x,y) = \begin{cases} \text{Dry Interface} & h_M \\ \text{Wet Interface} & 0 \end{cases} \tag{9}$$

In Eq. (10), the variations of $h_{M,eff}(x,y)$ were averaged along the dry GDL-channel interface width (W-$W_{wet}(x)$) into the dry-region-averaged mass transfer coefficient ($\overline{h_M}(x)$) to express its variation in the flow direction.

$$\overline{h_{\mathrm{M}}}(x) = \frac{1}{W - W_{\mathrm{wet}}} \int_{y=0}^{\mathrm{W}} h_{\mathrm{M,eff}}\, \mathrm{d}y \tag{10}$$

The dependency of $\overline{h_{\mathrm{M}}}$ on d_{h} and $D_{\mathrm{O2\text{-}air}}$ was eliminated with the use of Sherwood number ($\mathrm{Sh} = \overline{h_{\mathrm{M}}} d_{\mathrm{h}} / D_{\mathrm{O2-air}}$). For expressing the variations of Sh along the flow direction in a more compact manner, Sh was averaged in between two consecutive droplets (*n* and *n*+1 in the row) into down-the-channel-averaged Sh ($\mathrm{Sh}_{\mathrm{av},n}$) as shown in Eq.(11).

$$\mathrm{Sh}_{\mathrm{av},n} = \frac{1}{W - W_{\mathrm{wet}}} \int_{x=x_{\mathrm{d},n}}^{x_{\mathrm{d},n}+\Delta x_{\mathrm{d}}} \mathrm{Sh}\mathrm{d}x \tag{11}$$

4.3. NUMERICAL MODEL

4.3.1. Governing Equations

In this numerical study, convective mass transport was modeled with steady-state and 3D formulation of governing equations. The air was assumed to be compressible. The corresponding continuity equation, as shown in Eq. (12), was solved in both air channel and GDL. For the momentum transport in the air channel and GDL, the respective equations are solved: Navier-Stokes equation (Eq. (13)) and Brinkman equation (Eq. (14)). The oxygen transport in both air channel and GDL was governed by advection-diffusion equation as presented in Eq. (15). The diffusive component is modeled by Fick's law. This is a simplified formulation of Maxwell-Stefan equation. This simplification is justified for a condition of transported species being dilute in the mixture as stated by Krishna and Wesselingh [93]. Since, oxygen had a molar fraction of 0.11 at the channel inlet, Fick's law could be utilized.

$$\rho \nabla \cdot \mathbf{u} = 0 \tag{12}$$

$$\rho(\mathbf{u} \cdot \nabla)\mathbf{u} = \nabla \cdot [-p\mathbf{I} + \mu(\nabla \mathbf{u} + (\nabla \mathbf{u})^T)] \tag{13}$$

$$\frac{\rho}{\varepsilon_{\mathrm{GDL}}}(\mathbf{u} \cdot \nabla)\frac{\mathbf{u}}{\varepsilon_{\mathrm{GDL}}} = -\nabla p + \nabla \cdot \left[\frac{\mu}{\varepsilon_{\mathrm{GDL}}}(\nabla \mathbf{u} + (\nabla \mathbf{u})^T)\right] - \frac{\mu}{K}\mathbf{u} \tag{14}$$

$$\mathbf{u} \cdot \nabla C = \nabla \cdot (D_{\mathrm{O2-air}} \nabla C) \tag{15}$$

In order to reduce the computational cost of the numerical solution, the governing equations were solved separately, the entire length of the domain was treated in shorter and separate components, and a symmetry boundary condition was utilized. Firstly, constant air properties allowed the separate solutions of the governing equations. Eqs. (12) and (14) were initially solved together, and then followed by Eq. (15). Secondly, the entire length of the channel was divided into three sections and the resulting shorter channel sections were simulated in sequence along the flow direction. The resulting flow profiles at the exit of the first and second sections were mapped as inlet conditions for the second and third sections, respectively. The third section housed the droplets or films that were placed in a row starting from 3.00 mm away from the channel inlet. For convenience, x = 0 and 3.00 mm will refer to the third channel inlet and the location of the water feature, respectively in the following text. This technique was verified by comparing two approaches that simulated the entire channel either as a single domain and three separate domains. As the final technique to reduce the computational requirements, a symmetry boundary condition was imposed at the $y = W/2$ plane.

Figure 20 shows the mesh for the symmetric half of the channel that is housing hollow droplet-shaped obstructions with a radius of 0.15 mm. Along with tetrahedral mesh elements, boundary layer mesh elements were used on the channel walls and droplet boundary to increase accuracy. The maximum mesh element size in this domain is 58.7 μm that was established as a result of a mesh independency study as presented in Section 4.3.4.1.

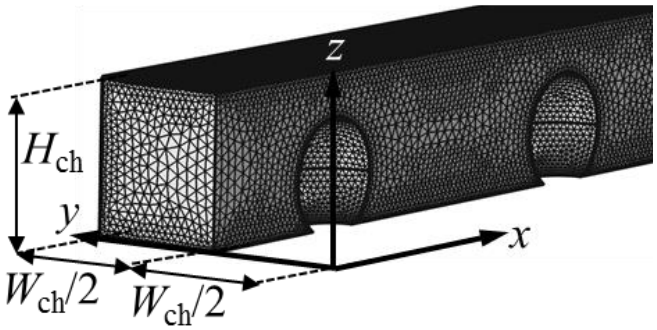

Figure 20: The meshed domain as the result of mesh independency study. The droplet radius is r = 0.15 mm and uniform droplet spacing Δx_d = 1.00 mm. The first droplet is moved closer to the inlet for easier demonstration.

4.3.2. Boundary Conditions (BCs) for the Numerical Model

4.3.2.1. BC at the reacting surface of the GDL

The O_2 flux into the CL ($j_{O2,ac}$) is a function of the local current density (i) at the repetitive unit CL area. The current density was assumed to be constant over the entire active area and ranged from 0.05 to 1.5 A cm^{-2}. The current density was assumed to be constant over the flow direction. The available literature provides the extent of current density variation along the channel width. The numerical work by Um and Wang showed that the current density variation is 23% at 1.01 A cm^{-2} [94]. The experimental work by Wang and Liu demonstrated that current density variations are less than 18% for average current densities larger than 0.30 A cm^{-2} [95]. Since the current work mostly covers current densities larger than 0.30 A cm^{-2}, the aforementioned findings are relevant to this work. As a result, the current density was assumed to be uniform along the channel width.

Superficial velocities of oxygen ($u_{O2,ac}$) and water vapor ($u_{H2O,ac}$) at the active area are required to be expressed to calculate the net air velocity as a boundary condition at the GDL-channel interface. They are dependent on their respective molar fluxes and ultimately, current density. While oxygen is consumed at the cathode side, water is produced. Hence, these fluxes have the opposite direction. Molar flux of oxygen ($j_{O2,ac}$) and vapor ($j_{H2O,ac}$) are expressed in Eqs. (16) and (17), respectively. Exchanged number of electrons per reacting/produced molecule (τ) is

4 and 2, for oxygen and water, respectively. F_c is the Faraday's constant relating the magnitude of electric charge per mole of electrons. Depending on the thermal condition of the cell, a portion of water (ξ) is in the vapor state. For maximum, injection and suction, ξ corresponds to 1 and 0, respectively.

$$j_{\mathrm{O2,ac}} = \frac{i}{\tau_{\mathrm{O2}} F_{\mathrm{c}}} \tag{16}$$

$$j_{\mathrm{H2O,ac}} = \xi \frac{i}{\tau_{\mathrm{H2O}} F_{\mathrm{c}}} \tag{17}$$

The calculated magnitude of oxygen flux at the active area corresponds to the range of $j_{O2,ac}$ = 0.130×10^{-2} – 3.886×10^{-2} mol m^{-2} s^{-1}. These values assigned as a boundary condition in conjugate simulations with GDL. The magnitude of water vapor flux was only used in the calculation of other boundary conditions: channel inlet and GDL-air channel interface (when neglecting the GDL). The magnitude of vapor flux at ξ=1 corresponds to: $j_{H2O,ac}$ = 0.260×10^{-2} – 7.772×10^{-2} mol m^{-2} s^{-1}.

Molar fluxes of species at the active area can be transformed into superficial velocities with the use of respective molar concentrations at channel the inlet (C_{in}): $u_{ac} = j_{ac}\, C_{in}^{-1}$. In order to calculate the molar concentration of species in the air at the inlet, the ideal gas law was utilized in Eq. (18). The molar concentration of an ideal gas (C) is p / ($R_u \times T$) where universal gas constant R_u = 8.314 J $^{\circ}C^{-1}$ mol^{-1} and C is the molar concentration of the gas in interest in mol m^{-3}.

$$C_{k,\mathrm{in}} = C_{\mathrm{air}} \times \omega_k = \left(\frac{p_{\mathrm{air}}}{R_{\mathrm{u}} \times T}\right) \times \omega_k \tag{18}$$

The molar fractions of O_2 (ω_{O2}) and vapor (ω_{H2O}) in air are required to utilize Eq. (18). In order to obtain ω_{O2}, the first step was to calculate ω_{H2O}. The partial pressure of water vapor (p_{H2O}) is equal to the saturation pressure (p_{sat} = 101325 Pa) since relative humidity is 100%:

$$\omega_{H_2O} = \frac{p_{H2O}}{p_{air}} = \frac{p_{sat}}{p_{air}} \tag{19}$$

Saturation pressure of water vapor is given as a function of temperature in °C [13]:

$$p_{sat} = -2846.4 + 411.24T - 10.554T^2 + 0.16636T^3 \text{ [Pa]} \tag{20}$$

The remaining portion of the gas is dry air and treated with a N_2/O_2 molar ratio of 79/21:

$$\begin{matrix} \omega_{O2} \\ \omega_{N2} \end{matrix} = \begin{cases} 0.21(1 - \omega_{H2O}) \\ 0.79(1 - \omega_{H2O}) \end{cases} \tag{21}$$

The molar fraction (ω) averaged velocity of the air is calculated with superficial oxygen ($u_{O2,ac}$) and vapor ($u_{H2O,ac}$) velocities at the active area as expressed in Eq. (22). During this calculation, superficial nitrogen velocity is zero ($u_{N2,ac}$ = 0) since there is no transport of nitrogen.

$$u_{air,ac} = u_{O2,ac} \times \omega_{O2} + u_{H2O,ac} \times \omega_{H2O} + u_{N2,ac} \times \omega_{N2} \tag{22}$$

4.3.2.2. BC at the GDL-reactant channel interface

This interface was treated with a boundary condition for simulations that neglected the GDL. The assumption of constant current density at the active area (from the previous section) was translated to the GDL-channel interface as a constant oxygen flux condition since channel width was larger than the land width.

The flux of species through the GDL-air channel interface (j_{int}) is a scaled-up value of the flux at the electrochemically active area under a channel and a land (j_{ac}). As shown in Figure 17, the active area is a repeating pattern that covers the width of the GDL-air channel interface and a bipolar plate land (rib) width. The land width (W_{land}) was taken to be 0.50 mm [91]. The scaling-up from j_{ac} to j_{int} stems from the fact that the unit active area narrows down for a width of land. Moreover, the water features restricts the mass transport further more by covering the interfacial area. The aforementioned effects are incorporated in Eq. (23). As a result, magnitude of oxygen flux at the interface ($j_{O2,int}$) can be calculated with Eq. (23).

$$j_{\text{int}} = j_{\text{ac}} \frac{A_{\text{ac}}}{A_{\text{int}}} = j_{\text{ac}} \frac{(W + W_{\text{land}})L}{[W - W_{wet}(x)]L} = j_{\text{ac}} \frac{(W + W_{\text{land}})}{[W - W_{wet}(x)]} \tag{23}$$

With the use of Eq. (16) and (23), the corresponding range of O_2 flux at the GDL-air channel interface was found to be $j_{O2\text{-}int} = 0.222\times10^{-2}$ - 6.662×10^{-2} mol m^{-2} s^{-1} for the current density range of 0.05 – 1.5 A cm^{-2}.

Injection or suction of air was imposed at the GDL-air interface only in some cases plain channels with no water features. For cases with water features, no injection and suction was imposed at the interface. The superficial air velocity at the active area ($u_{air,ac}$) can be mapped to the value at the GDL-channel interface ($u_{air,int}$) in isolated channel simulations through a similar use of Eq. (23). The air velocity at the GDL-channel interface is presented with non-dimensional interfacial Reynolds number ($Re_{int}=u_{air,int}\times d_h\times\rho\times\mu^{-1}$). Table 2 shows the respective channel Reynolds number ($Re_{ch}=u_m\times d_h\times\rho\times\mu^{-1}$), and the maximum possible absolute Re_{ch} corresponding to ξ = 0 and 1. The calculation of superficial air velocity in the channel (u_m) will be provided in the following section. Each case of current density was simulated with the corresponding $|Re_{int}|$ which was applied as both injection and suction.

Table 2: Simulated current densities with the corresponding channel (Re_{ch}) and absolute interfacial ($|Re_{int}|$) Reynolds numbers.

i (A cm^{-2})	0.1	0.4	0.7	1.0	1.5
Re_{ch}	41.31	110.16	192.78	275.15	412.85
$\|Re_{int}\|\times10^2$	0.34	1.34	2.34	3.35	5.01

4.3.2.3. BCs at the channel inlet and outlet

Uniform velocity profile was imposed at the channel inlet with the corresponding superficial air velocity (u_m). The velocity can be derived from the volumetric flow rate of air at the inlet (Q_{air}) through $u_m = Q_{air} / (W_{ch}\times H_{ch})$. The volumetric flow rate through a single channel should be at least as much as the volumetric air consumption rate by the repetitive active area. If the stoichiometric ratio (λ) is 1, the air flow rate ($Q_{air,\lambda=1}$) is equal to the air consumption rate. However, this does not allow the PEMFC to operate due to excessive mass transport losses. Therefore, the stoichiometric ratio was taken as 2 for the entire current density, except it was 3 for 0.05 and 0.1 A cm^{-2}. Eq. (24) shows the calculation of air flow rate at the inlet as a function of molar oxygen consumption rate at the active area ($J_{O2,ac}$), molar concentration of oxygen in the air at the inlet ($C_{O2,in}$), and the stoichiometric ratio (λ).

$$Q_{\mathrm{air}} = Q_{\mathrm{air},\lambda=1} \times \lambda = \left(\frac{J_{\mathrm{O2,ac}}}{C_{\mathrm{O2}}}\right) \times \lambda \tag{24}$$

The molar consumption at the active area was calculated as $J_{O2,ac} = j_{O2,ac}\times(W_{ch}+W_{land})\times L_{ac}$. The active area length (L_{ac}) was taken as 183.00 mm [91]. By using the equations above, the superficial air velocity at the channel inlet was calculated. Table 3 presents the velocity values and the corresponding Péclet numbers.

Table 3: Mapping from current density (i) to superficial air velocity (u_m) and Péclet number (Pe) for fully humidified air at 80 °C.

i [A cm^{-2}]	0.05	0.10	0.20	0.30	0.40	0.70	0.80	1.00	1.50
u_m [m s^{-1}]	0.80	1.59	2.12	3.18	4.24	7.41	8.48	10.59	15.89
Pe	13.16	26.16	34.88	52.32	69.75	121.91	139.51	174.22	261.42

The temperature 80 °C leads to an approximately two times the superficial fully humidified air velocity at 20 °C. It has been previously stated that as the flow is far away from being fully developed, Sherwood number can differ more significantly. Hence, using a velocity range with larger values revealed the maximum possible variations in Sherwood number. As to be presented in the following sections, velocities below 1.59 m s^{-1} led to very similar results at 1.59 m s^{-1}. Hence, the selected velocity range at 80 °C can also be useful for high current densities at 20 °C.

The correlation between current density and the superficial air velocity in a channel was based on the even distribution of air flow from the manifold to parallel channels. In reality, the blockage of a few channels can increase the air velocity in the unblocked channels. The selected maximum velocity was high enough for the following reason: Droplets were analyzed if they can remain in the spherical shape as the air velocity increases. The analysis showed that any velocity larger than 15.89 m s^{-1} did not allow even the smallest simulated droplet to remain as a sphere. This analysis will be shown in the following sections.

Constant O_2 concentration (3.83 mol m^{-3}) was imposed at the inlet. Zero gauge pressure was imposed at the outlet. At this boundary, species transport took place only by advection.

4.3.2.4. BC at the channel walls and water feature surface

No-slip boundary condition was imposed at channel side walls, top wall, and water feature surfaces. The no-slip boundary condition on the droplet surface can be justified with the experimental study that documented the internal recirculation velocity of a droplet [84]. The maximum velocity of the recirculation was at most 2% of the superficial air flow velocity in the

channel. Even though films were expected to have a higher interfacial velocity than the droplets, the increase was not expected to be large enough to violate the aforementioned assumption.

Since the O_2 transport through the water feature is negligible compared to the one in at the GDL-air channel interface, the O_2 flux (j_{O2}) was imposed to be zero on the water feature interface with air. Moreover, side walls and top wall of the channel had zero j_{O2}.

4.3.3. Selection of Input Parameters

4.3.3.1. Droplet representation

Certain sets of droplet size and superficial air velocity were excluded from the simulation matrix as being unrealistic cases. The minimum droplet radius was chosen to be 0.10 mm that was governed by the maximum GDL pore size of 0.10 mm [78]. The maximum droplet radius was dependent on the specific superficial air velocity value since a set of these parameters had to comply with the following conditions: 1) the droplets should remain in the form a sphere, and 2) droplets should remain attached to the GDL-air channel interface. When these conditions were satisfied, the use of droplet-shaped obstructions could be justified.

4.3.3.1.1 *Droplet shape*

For the droplets to be assumed spherical, the surface tension force on the droplet should dominate gravitational and inertial forces. The Bond number (Bo) was used to characterize how dominant the gravitational force was over the surface tension force: $Bo = \rho_{H2O} g r^2/\sigma$ where g and σ are gravitational acceleration and surface tension between water and air (62.6 mN m^{-1}), respectively. Das et al. experimentally showed that the droplet shape can be assumed to be spherical on a hydrophobic GDL surface for a Bo value up to 0.1 [70]. This observation leads to the independency of droplet shape from the gravitational force up to a droplet height equal to the channel height. A droplet at the channel height corresponds to the droplet radius of approximately 0.20 mm and this value may be further reduced depending on the air velocity.

The air flow can deform a droplet from the perfect spherical shape. The deformation of the droplet was experimentally characterized by Cho et al. with the mismatch between the two radii of curvature normalized by the non-deformed droplet radius (r_y - r_x) / r [82], [83]. The deformed shape can be expressed as an ellipsoid with a semi-major axis of r_x and a semi-minor axis r_y. The mismatch between the two semi-principal axes is normalized with the average droplet radius (r_y - r_x) / r. The authors correlated these normalized deformations with the Weber number (We) and channel blockage ratio (ξ). The Weber number expresses how dominant the air flow inertia is over the surface tension (σ = 62.6 mN m^{-1}). The channel blockage ratio takes the increased air flow velocity into account when a droplet constricts the channel. Eq. (25) provides the aforementioned correlation in which θ is in radians.

$$\frac{(r_y - r_x)}{r} = \frac{\mathrm{We}}{4}\xi^2 = \left(\frac{\rho u_\mathrm{m}^2 r}{4\sigma}\right)\left(\frac{W_\mathrm{ch}H_\mathrm{ch}}{W_\mathrm{ch}H_\mathrm{ch} - r^2(\theta - \cos\theta\sin\theta)}\right)^2 \tag{25}$$

Table 4 shows the calculated normalized deformation values for a set of droplet radius and superficial air velocity. The emboldened values indicate cases with deformations larger than 0.105. These cases were not simulated as the spherical droplet assumption was not valid.

Table 4: The deformation of a droplet characterized as the normalized mismatch between the radii of curvature (r_y - r_x) / r, and tabulated for sets of droplet radius (r) and superficial air velocity (u_m). The emboldened values indicate cases that were not simulated due to deformations larger than 0.105.

r [mm]	u_m [m s^{-1}]					
	1.59	4.24	7.41	8.48	10.59	15.89
0.10	0.001	0.007	0.023	0.030	0.047	0.105
0.12	0.001	0.010	0.031	0.040	0.063	**0.141**
0.15	0.002	0.016	0.048	0.062	0.097	**0.219**
0.18	0.004	0.025	0.077	0.101	**0.158**	**0.356**
0.20	0.005	0.037	**0.113**	**0.148**	**0.230**	**0.518**

4.3.3.1.2 *Droplet adhesion*

The cases that did not lead to a significant droplet deformation were simulated. After conducting single-droplet simulations, numerically calculated drag forces were used to check if the droplets can remain adhered to the GDL-air channel interface. The numerically calculated drag forces were compared against experimentally obtained adhesion forces from the available literature. The droplet-adhesion-force-per-unit-footprint-perimeter was provided by Das et al. for aged SGL 24BA and 24DA GDL samples as 22 and 17 μN mm^{-1}, respectively [70]. An average value of 20 μN mm^{-1} was used in the adhesion force calculations.

Since the adhesion force was acquired through an experiment with a GDL, the value, and hence the simulation, took the GDL surface roughness into account. Table 5 shows the numerically calculated drag force (F_x) for each droplet size and superficial mean air velocity. The adhesion forces calculated for the given droplet radius range (r = 0.10-0.20 mm) are 6.84, 8.21, 10.27, 12.32, and 13.69 μN. The adhesion forces always remained larger than the numerically obtained drag forces (F_x) except u_m = 8.48 m s^{-1} and r = 0.18 mm. This exception was still treated as an attachment case to increase the richness of the processed data. Hence, the droplet obstruction method can be used with this simulation matrix.

Table 5: The numerically obtained air drag on a droplet in the flow direction (F_x [μN]) as a function of superficial mean air velocity (u_m) and droplet radius (r). (The empty elements indicate the cases that were not simulated due to the deformation in droplet shape).

r [mm]	u_m [m s^{-1}]								
	0.80	1.59	2.12	3.18	4.24	7.41	8.48	10.59	15.89
0.10	0.09	0.21	0.31	0.54	0.80	1.82	2.25	3.16	6.01
0.12	0.15	0.34	0.49	0.85	1.28	2.94	3.60	5.11	
0.15	0.29	0.66	0.94	1.62	2.42	5.57	6.83	9.69	
0.18	0.58	1.32	1.91	3.24	4.77	10.74	13.16		
0.20	0.92	2.12	3.10	5.44	8.20				

4.3.3.1.3 *Uniform droplet spacing*

The uniform spacing between the droplets was varied in between the values that were documented to exist in an operational fuel cell and also led to meaningful changes in Sherwood number. Visualization studies of operational PEMFCs reported in literature were used to extract a representative value for the minimum droplet spacing. The droplet images provided by Yang et al. [73] and Zhang et al. [75] suggest that 1.00 mm is a reasonable droplet spacing. The maximum droplet spacing needs to be chosen in such a way that two consecutive large droplets should be close enough to interact even at low superficial air velocities. When the velocity was 4.24 m s^{-1} and the droplet radius was 0.20 mm, Sherwood number was only marginally affected 5.00 mm downstream of the droplet. Therefore, the maximum droplet spacing was chosen to be 5.00 mm. As an intermediate value of droplet spacing, 2.00 mm was selected since most of the maximum local Sherwood number values were seen 2.00 mm downstream of a droplet.

4.3.3.1.4 *Test matrix*

As shown in Table 5, there are 37 cases to be simulated for each droplet spacing value. Along with the three droplet spacing values, the total number of simulated cases was 111.

4.3.3.2. Film representation

Film width (W_f) was varied from 0.20 to 0.50 mm (corresponding to non-dimensional values of 0.39 to 0.98, respectively). The length of the film (L_f) took the value of 0 to represent a droplet on the side wall of the channel. Non-zero film length and uniform film spacing values were were 1.00, 2.00, and 5.00 mm (non-dimensionally: 1.96, 3.92, and 9.80, respectively).

4.3.3.2.1 *Film adhesion*

Figure 21 shows a typical film viewed from two orthonormal axes: *z* (top of the channel) and *y* (side of the channel). The triple-phase contact lines (TPCLs) are shown with solid lines on the top and side channel walls in Figure 21a and Figure 21b, respectively. TPCL on the GDL is

shown with a line of dashes and dots in Figure 21a. The length of the film (L_f) was assigned to be zero to represent the earlier stages of water emergence from the GDL (not shown in Figure 21). For curved TPCLs, two angular position variables were defined (α_y and α_z). These angles are measured in between the normal to the TPCL and flow direction. As the convention, the angle α = 0 is directed towards the upstream of the air flow.

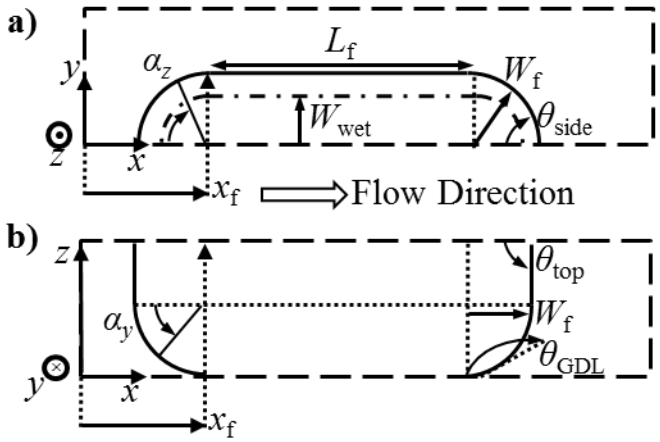

Figure 21: Film dimensions, TPCLs, contact angles and conventions of positioning which are shown from a) the top (*z* axis) and b) the side (*y* axis) channel walls. (Long dashed lines: channel wall boundaries; Solid lines: TPCLs on the top and side channel wall; Dashed-dotted lines: TPCL on the GDL surface)

The adhesion force of a film (F_{ad}) has components from the GDL ($F_{ad,GDL}$), channel side wall ($F_{ad,side}$) and top wall ($F_{ad,top}$): $F_{ad} = F_{ad,GDL} + F_{ad,side} + F_{ad,top}$. TPCLs on the GDL at the positions of $x<x_f$ and $x>x_f+L_f$, correspond to the footprint of truncated spheres and hence, are the split components of a droplet footprint. The GDL component of the adhesion force was calculated through the adhesion force per unit footprint perimeter which is provided by Das et al. [70]: 20 $\mu N\ mm^{-1}$.

The adhesion force due to the air channel side wall and top wall can be calculated using the contact angle hysteresis obtained for the wall material. The contact angles on the channel walls range from θ_{rec} to θ_{st} as α varies from 0 to $\pi/2$. For values of $\pi/2 \leq \alpha \leq \pi$, θ varies from θ_{st} to θ_{adv}. Utilizing Eqs. (26) – (29), contributions to the adhesion force from the aforementioned walls can

be calculated at curved TPCLs. Eqs. (27) and (28) assume a linear variation from the advancing to receding contact angle points at the TPCL. For straight TPCLs that are normal to the *x* axis, the entire line takes either an advancing or a receding contact angle value.

$$F_{\mathrm{ad}} = \sigma W_{\mathrm{f}} \int_{\alpha=0}^{\pi} \cos\alpha \cos\theta \, \mathrm{d}\alpha \tag{26}$$

$$\theta = \theta_{\mathrm{ramp}}[\theta_{\mathrm{adv}} - \theta_{\mathrm{rec}}] + \theta_{\mathrm{rec}} \tag{27}$$

$$\theta_{\mathrm{ramp}} = \alpha/\pi \tag{28}$$

$$\alpha = \begin{cases} (x \le x_{\mathrm{f}}) \rightarrow \cos^{-1}[(x_{\mathrm{f}} - x)/W_{\mathrm{f}}] \\ [x_{\mathrm{f}} < x < (x_{\mathrm{f}} + L_{\mathrm{f}})] \rightarrow \pi/2 \\ [x \ge (x_{\mathrm{f}} + L_{\mathrm{f}})] \rightarrow \cos^{-1}[(x_{\mathrm{f}} + L_{\mathrm{f}} - x)/W_{\mathrm{f}}] \end{cases} \tag{29}$$

The integral in Eq. (26) needs to be calculated at each curved TPCL as shown in Figure 21, except the ones on the GDL. The contributions to adhesion force from the side and top walls, and the GDL are presented in Table 6. At the smallest film width, the side walls contribute the most to the adhesion force. The GDL provides the highest contribution for $W_{\mathrm{f}} \geq 0.25$ mm. These contributions are independent of the film length.

Table 6: The net adhesion on a film (F_{ad}) [μN] with its components: GDL (F_{GDL}), channel side wall (F_{side}) and top wall (F_{top}).

W_{f} [mm]	$F_{\mathrm{ad,GDL}}$	$F_{\mathrm{ad,side}}$	$F_{\mathrm{ad,top}}$	F_{ad}
0.20	6.83	8.76	3.18	18.78
0.25	8.55	8.47	3.97	20.99
0.30	10.26	8.17	4.77	23.20
0.35	11.98	7.87	5.56	25.41
0.40	13.69	7.57	6.36	27.63
0.45	15.40	7.27	7.15	29.83
0.50	17.12	6.98	7.94	32.04

The drag force on films ($F_{\mathrm{D,f}}$) with variable width (W_{f}) and length (L_{f}) at variable superficial air velocities (u_{m}) was numerically calculated. Table 7 – Table 10 show films with the lengths: L_{f}

= 0, 1.00, 2.00 and 5.00 mm. Table 7 the drag force on zero-length films that correspond to droplets at corners. For a given W_f, u_m was increased incrementally until the first condition of detachment was achieved. The drag forces presented in Table 7 can be interpreted as the pressure difference up and downstream of films.

Table 7: Drag force $F_{D,f}$ [μN] on a film with a length L_f = 0 at variable film width (W_f) and superficial air velocity (u_m).

W_f [mm]	u_m [m s^{-1}]									
	1.59	2.12	3.18	4.24	5.30	7.41	8.48	10.59	12.72	15.89
0.20	0.37	0.70	1.23	1.42	2.57	3.21	5.25	5.49	9.94	10.25
0.25	0.72	1.06	1.88	2.86	4.00	6.73	8.31	11.90	15.94	**23.17**
0.30	1.04	1.55	2.76	4.23	5.94	10.07	12.48	17.97	**24.18**	
0.35	1.48	2.21	3.96	6.10	8.61	14.68	18.22	**26.35**		
0.40	2.08	3.11	5.62	8.68	12.29	21.07	26.20	**38.00**		
0.45	2.93	4.39	7.96	12.33	17.50	30.10	**37.49**			
0.50	4.16	6.23	11.35	17.62	25.06	**43.21**				

As films elongate (L_f > 0), the drag has an additional contribution due to the shear applied to the side of the film. All the cases shown in Table 7 were simulated for non-zero film lengths. Table 8 shows the drag forces for a film length of L_f = 1.00 mm. The drag forces are approximately doubled from with the introduction of 1.00 mm film length to corner droplets.

Table 8: Drag force $F_{D,f}$ [μN] on a film with a length L_f = 1.00 mm at variable film width (W_f) and superficial air velocity (u_m). (Emboldened values indicate detachment)

W_f [mm]	u_m [mm]									
	1.59	2.12	3.18	4.24	5.30	7.41	8.48	10.59	12.72	15.89
0.20	1.08	1.53	2.51	3.61	4.83	7.58	9.12	12.45	16.15	**22.28**
0.25	1.56	2.21	3.67	5.33	7.18	11.42	13.82	19.03	**24.85**	**34.60**
0.30	2.20	3.13	5.26	7.70	10.44	16.78	20.36	**28.26**	**37.06**	
0.35	3.09	4.42	7.47	10.99	14.99	24.27	**29.56**	**41.19**		
0.40	4.34	6.23	10.59	15.63	21.43	**34.85**	**42.61**	**59.51**		
0.45	6.15	8.84	15.07	22.35	**30.67**	**50.17**	**61.35**			
0.50	8.90	12.78	21.82	**32.40**	**44.53**	**73.00**				

Table 9 shows drag forces on films with a length of L_f = 2.00 mm. The shear rate at the side of the film approaches to a constant value as the flow becomes closer to fully developed. Hence, for a given case the increase from Table 8 to Table 9 is smaller than the increase from Table 7 to Table 8.

Table 9: Drag force $F_{D,f}$ [μN] on a film with a length L_f = 2.00 mm at variable film width (W_f) and superficial air velocity (u_m). (Emboldened values indicate detachment)

W_f [mm]	u_m [mm]									
	1.59	2.12	3.18	4.24	5.30	7.41	8.48	10.59	12.72	15.89
0.20	1.69	2.35	3.77	5.32	7.03	10.81	12.90	17.40	**22.32**	**30.44**
0.25	2.39	3.33	5.40	7.70	10.25	15.97	19.17	**26.08**	**33.72**	**46.42**
0.30	3.34	4.68	7.64	10.98	14.69	23.14	**27.88**	**38.21**	**49.66**	
0.35	4.66	6.54	10.75	15.53	20.89	**33.15**	**40.06**	**55.17**		
0.40	6.53	9.20	15.18	21.98	**29.69**	**47.32**	**57.41**	**79.24**		
0.45	9.28	13.06	21.60	**31.37**	**42.41**	**67.91**	**82.39**			
0.50	13.46	18.95	31.35	**45.56**	**61.60**	**98.75**				

Table 10 shows the film drag values for L_f = 5.00 mm. The highest simulated film length, L_f = 5.00 mm led to two cases of detachment at the highest superficial air velocity and highest two film width.

Table 10: Drag force $F_{D,f}$ [μN] on a film with a length L_f = 5.00 mm at variable film width (W_f) and superficial air velocity (u_m). (Emboldened values indicate detachment)

W_f [mm]	u_m [mm]									
	1.59	2.12	3.18	4.24	5.30	7.41	8.48	10.59	12.72	15.89
0.20	3.51	4.79	7.45	10.23	13.27	**19.72**	**23.32**	**30.71**	**38.88**	**51.85**
0.25	4.88	6.66	10.42	14.45	18.80	**28.34**	**33.58**	**44.75**	**56.95**	**76.94**
0.30	6.75	9.23	14.52	20.23	**26.45**	**40.22**	**47.85**	**64.23**	**82.24**	
0.35	9.35	12.81	20.22	**28.29**	**37.10**	**56.81**	**67.77**	**91.46**		
0.40	13.07	17.94	**28.39**	**39.77**	**52.33**	**80.37**	**96.18**	**130.09**		
0.45	18.58	25.49	**40.38**	**56.68**	**74.57**	**114.85**	**137.39**			
0.50	27.07	**37.14**	**58.83**	**82.56**	**108.59**	**167.15**				

4.3.3.2.2 *Test Matrix*

Non-zero length films were assumed to detach when their respective zero-length analysis predicted the detachment. Utilizing the aforementioned detachment prediction, each film length had 58 simulated cases as shown in Table 7. As there were 4 film lengths simulated, a total of 232 simulations were performed. For building Sh correlations, combinations of W_f-u_m were selected to match the attachment cases presented for zero film lengths in Table 7. A total of 208 data points were used to build the correlations.

Multiple film cases were selected based on the data set used for single film Sh correlations. All the attachment resulting combinations of W_f-u_m obtained from Table 7 were simulated for variable film spacing (Δx_f) and length (L_f). Some of the W_f-u_m conditions could not be numerically simulated due to continuous flow disruption by multiple films. Hence, these cases were not included in the results. Table 11 presents the W_f-u_m combinations that were analyzed.

Table 11: Combinations of film width (W_f) and superficial air velocity (u_m) that were simulated for each permutation of film length (L_f) and uniform spacing (Δx_f).

W_f [mm]	u_m [mm]						
	1.59	2.12	3.18	4.24	7.41	10.59	15.89
0.20	x	x	x	x	x	x	
0.30	x	x	x	x	x	x	
0.40	x	x	x	x	x		
0.50	x	x	x	x			

4.3.4. Mesh Independency and Validation

4.3.4.1. Mesh independency of droplets

The numerical technique was checked for mesh independency for the figure of merits that were unique to this study and have not been established in the literature. Following the mesh independency, well established figures of merit from the literature were compared to the numerical results from the fully developed flow region. The mesh independency study was

performed on a case that led to the strongest flow disruption affiliated to high Sh and $F_{D,d}$. Droplets centered along the channel width create stronger disruption than films. Among the multiple droplets in a row, the strongest flow disruption was obtained by the case of u_m = 10.59 m s^{-1}, r = 0.15 mm and Δx_d = 2.00 mm. In the mesh independency study with these conditions, Sh and $F_{D,d}$ were observed to reach their asymptotic values by the sixth and third droplets, respectively. The asymptotic values mean less than 1.0% variation of the figure of merits in the flow direction. Among the three simulated mesh cases, the droplet on which the asymptotic $F_{D,d}$ was reached led to the largest $F_{D,d}$ variation in between the two meshes with the highest number of elements. Table 12 presents the three mesh configurations and their corresponding $F_{D,d}$ values at the third droplet. Mesh cases 2 and 3 led to $F_{D,d}$ values 0.5% different than each other and hence, showed mesh independency.

Table 12: The mesh configurations used for the multiple mesh independency study and the corresponding maximum drag forces exerted on the third droplet in the domain.

Mesh Case	Number of Elements	Max. Element Size [μm]	Drag on the 3rd Droplet, $F_{D,d}$ [μN]
1	365,280	114.0	10.05
2	690,958	87.6	10.30
3	1,725,467	58.7	10.45

Figure 22 depicts the Sh variation along the flow direction for the analyzed mesh cases. It is shown that the overall trend of Sh is the same for all mesh cases. The largest Sh deviation between the mesh cases can be seen in the wake of the third droplet (7.00 mm < x < 9.00 mm) which was also the most mesh-dependent droplet for the calculation of drag force. The comparison of Mesh 2 and 3 shows that the maximum Sh deviation in between the second and third droplets is 2.2%. Despite the marginal Sh and $F_{D,d}$ variation between Mesh 2 and 3, a conservative approach was taken and Mesh 3 was used for all droplet simulations in this work.

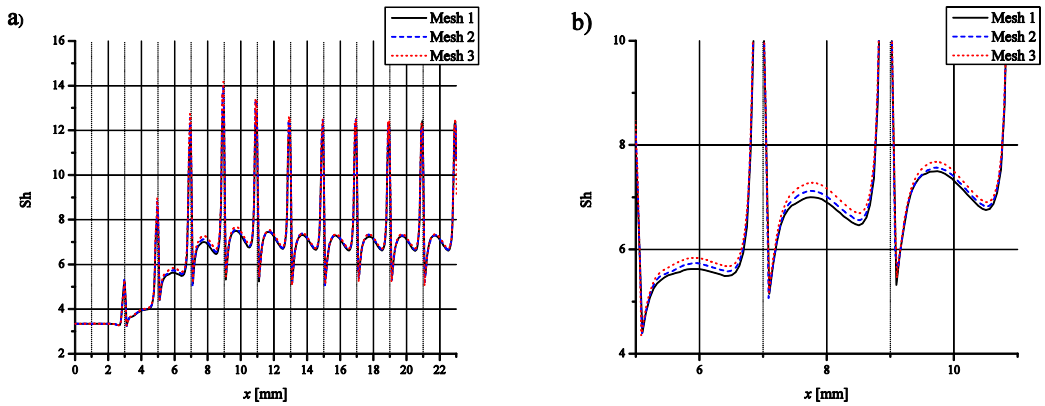

Figure 22: The Sherwood number (Sh) mesh independency study for the droplet radius r = 0.15 mm, superficial air velocity u_m = 10.59 m s^{-1}, and uniform droplet spacing Δx_d = 2.00 mm. The position of the first droplet $x_{d,1}$ = 3.00 mm. a) Depiction of the overall Sh trend, b) A close-up view of Sh in the wake of the seventh droplet ($x_{d,7}$ = 7.00 mm)

4.3.4.2. Mesh and geometry independency of films

Similar to the mesh independency study for multiple droplets, a similar was conducted for films. A zero-length film (corner droplet) is placed in a channel with the respective film width and superficial air velocity: 0.50 mm and 10.59 m s^{-1}. Table 13 shows the three mesh cases and their corresponding drag forces on the film ($F_{D,f}$). It can be concluded that there is no significant variance of $F_{D,f}$.

Table 13: The mesh configurations used for the single-film mesh independency study and the corresponding maximum drag forces exerted on the film.

Mesh Case	Number of Elements	Max. Element Size [μm]	Drag on the Film, $F_{D,f}$ [μN]
1	346,034	132.0	78.50
2	632,013	102.0	78.40
3	1,588,861	68.6	78.30

Local Sh profiles were also compared for the aforementioned mesh cases. There was no significant difference seen in between Mesh 2 and 3. Hence, Mesh 2 was used for all film simulations.

Following the mesh independency verification, the effect of film entrance type on local Sh was investigated. Figure 23 exemplifies the entrance type which helps to establish a convention for defining the film shape. The convention dictates the length of semi-principle axes, r_x and r_y, as shown in Figure 23. In the first geometrical configuration, r_x and r_y were selected to be equal. This geometrical configuration is referred to as "Sharp Entrance" and shown in Figure 23a. The second geometrical configuration represents physical conditions of large air velocities. This configuration has a relationship between r_x and r_y as $r_x = 2r_y$. The resulting geometry is referred to as "Smooth Entrance" and shown in Figure 23b. In both configurations, the film width (W_f) is equal to r_y which was kept constant at 0.50 mm while the air velocity was kept at 10.59 m s^{-1}. The rationale behind selecting high values of u_m and W_f was obtaining a high dependency of local Sh on the film entrance type. The aforementioned entrance types were used to conduct simulations and then compare local Sh profiles.

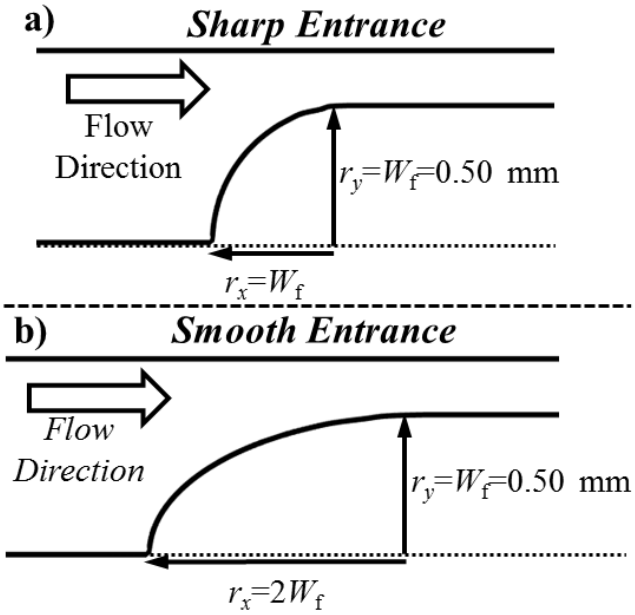

Figure 23: Different film entrance types that are represented by a varying semi-principle axis, r_x while the other, r_y is kept constant.

Figure 24 shows the effect of entrance types as described in the paragraph above on Sh. At the location where a film reaches its full width (x_f = 5.00 mm), local Sh values reach their respective maxima. After a distance of W_f downstream of the Sh peak, the maximum difference between local Sh values remains within 10%. Hence, the effect of film entrance type on Sh can be neglected in this study. For the convenience of defining the film geometry, "Sharp Entrance" convention was selected to be used for the simulations.

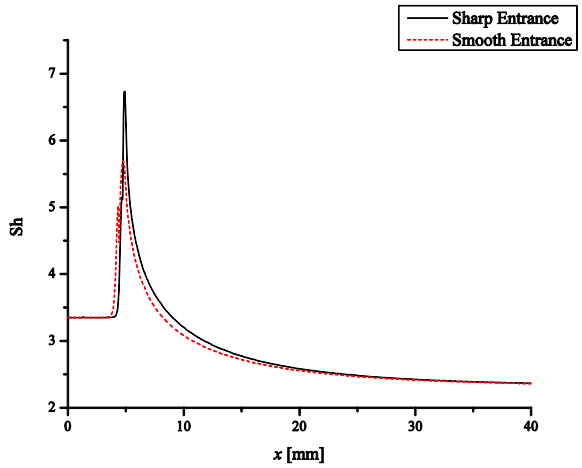

Figure 24: Effect of film entrance types on local Sherwood number (x_f = 5.00 mm).

4.3.4.3. Validation

Following the mesh independency study, the numerical method was validated through the use of fully developed values of Sh and Poiseuille (Po) numbers, backward-facing step problem, and entrance region values of Nusselt number (Nu) under injection/suction.

Since Sh is equal to Nu in the fully developed region, the numerical study on Nu by Dharaiya and Kandlikar [96] was utilized to validate Sh_{FD}. The correlation provided by this study [96] was developed for constant heat flux boundary condition that is equivalent to the constant O_2 flux. The values of Nu_{FD} = 3.584 [96] and Sh_{FD} = 3.349 deviate within 7.0% and hence, agree well. The value of Po_{FD} = 15.127 was provided by Shah and Sekulic [97]. This value agrees with the numerically obtained value Po_{FD} = 15.155 within 0.2% error.

The mesh selection was also validated through the use of a flow over backward-facing step problem which was visualized with laser Doppler velocimeter. Droplets and films disrupt the flow similar to forward and backward-facing steps neighboring each other. However, no such benchmarking has been established in the literature. Therefore, backward-facing step benchmark was utilized with a Reynolds number (343) very close to the maximum channel Reynolds number in this study (412.85 as shown in Table 2). Armaly et al. documented the flow velocity distributions in the channel described in Figure 25a [98]. The velocity component *u* was recorded at the line described by the non-dimensional position in Figure 25a.

Since droplet and film simulations do not have the same length scale and topology as the benchmark problem, the following criterion was used to bring the benchmark and droplet/film simulations on the same ground. The ratio of mesh size at the step to the step height (*S*) was chosen to be larger than the ratio of mesh size at the droplet/film position to the droplet/film height/width. Hence, if the benchmark problem can be simulated accurately so the droplet/film problem can be. The maximum and minimum mesh size to step size ratios in the benchmark simulation were 0.4863 and 0.0984, respectively. The maximum and minimum mesh size to droplet height ratios in the droplet simulation were 0.1889 and 0.0257, respectively. The maximum and minimum mesh size to film width ratios in the film simulation were 0.1711 and 0.03637, respectively. Therefore, the droplet and film domains were meshed with a finer mesh than the benchmark problem.

Figure 25b compares the experimental velocity distribution at the probing line [98] and numerical values. The maximum difference between the values is 7%. Therefore, the numerical technique utilizing mesh configurations obtained in the mesh independency sections was validated against experimental data and proven to be mesh-independent.

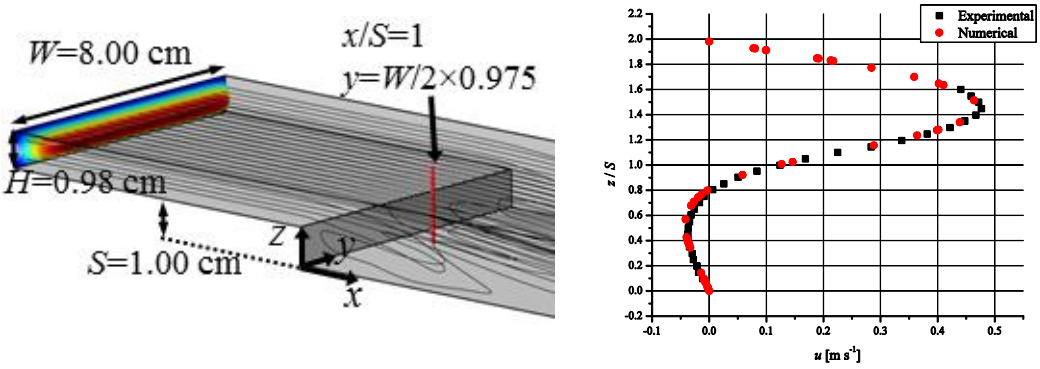

Figure 25: Flow over backward-facing step problem. a) Description of the problem geometry and flow conditions; b) Experimental vs. numerical comparison of velocity in the *x* direction (*u*) with respect to non-dimensionalized height (*z*/*S*).

The last validation was performed for insulated channels with injection/suction applied at the GDL-air channel interface. The numerical model was validated against experimental injection and suction studies. Since there was no experimental study available on the exact problem that is studied here, the heat transfer analogue of the problem was used for validation. Experiments by Cheng and Hwang [99] and Hwang et al. [100] provided heat transfer data under injection and suction conditions, respectively. The film simulation mesh configuration was used to simulate the two aforementioned experimental works and investigate the effects of injection/suction on Sherwood number. The channel cross section for films was meshed with 13 × 8 mesh elements corresponding to 0.70 mm × 0.40 mm dimensions, respectively. This configuration was complemented with 2 boundary layer mesh elements over the 4 channel walls. A mesh configuration of 8 × 8 mesh elements along with 2 boundary layer mesh elements were used for the experimental channel cross section of 20 mm × 20 mm [99], [100].

The heat transfer at the porous surface was characterized with Nusselt number (Nu) which is the heat transfer analogue of Sherwood number. The aforementioned studies reported mean Nusselt number (Nu_m) in the streamwise direction, in the developing entrance region of the flow. The mathematical definition of Nu_m at a given streamwise position, x_1 is $Nu_m|_{x_1} = \left(\int_{x=0}^{x_1} Nu\, dx\right) x_1^{-1}$.

The entrance region Nu_m profiles are shown in Figure 26 and Figure 27 for conditions of injection and suction, respectively. The streamwise distance in the channel is presented in a normalized way with hydraulic diameter (d_h), channel-based Reynolds number (Re_{ch}), and Prandtl number (Pr). These two cases are challenging enough as validation cases since their Re_{ch} values was almost identical (Re_{ch}=400.00) or higher (Re_{ch}=500.00) than the maximum Re_{ch}=412.85 used in the present study (as shown in Table 2).

Figure 26 shows the streamwise Nu_m variation for the case with injection, Re_{int} = 20.00. The values at each point are lower compared to the case with no injection. The reason behind this trend can be explained by the temperature difference between the mean fluid temperature and interfacial temperature. The fluid injected to the channel is at the same temperature with the interface. In the vicinity of the interface, temperature values start resembling the interface more closely due to injection. Consequently, the temperature drop needs to become larger. The largest error in the simulation results is 17% while all other points have an error equal or below 10%.

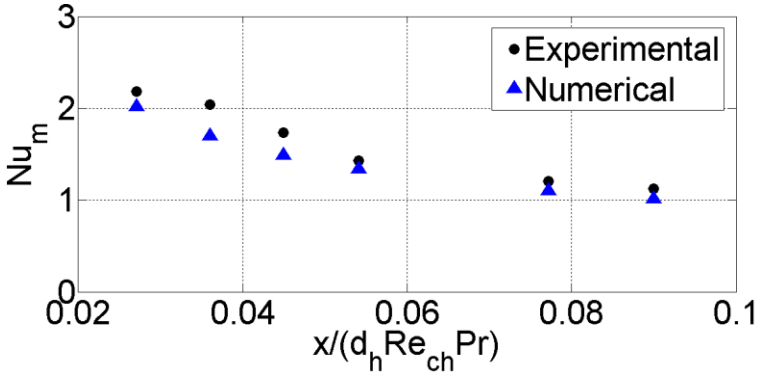

Figure 26: Comparison of experimental [99] and numerical mean Nusselt number (Nu_m) at channel Reynolds number of Re_{ch} = 400.00 and the interfacial Reynolds number of Re_{int} = 20.00 (corresponding to injection).

Figure 27 presents the comparison of experimental and numerical data for suction conditions, Re_{int} = -5. The values of Nu_m were obtained to be higher than the case with no suction. The reasoning behind this observation can be borrowed from the paragraph above and be applied

to suction conditions. The maximum numerical error is 7%. Both simulations suggest that the numerical technique is accurate.

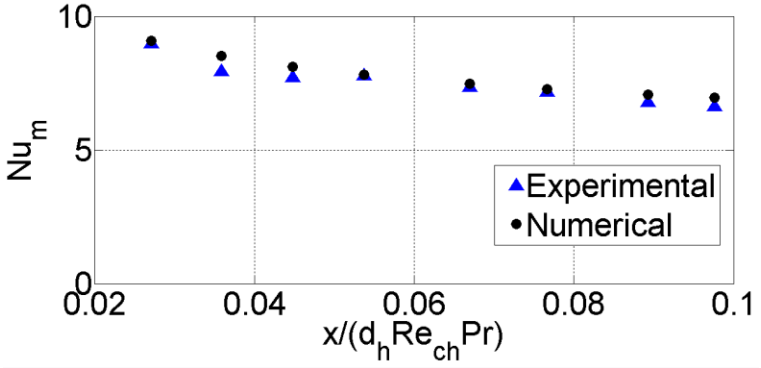

Figure 27: Comparison of experimental [100] and numerical mean Nusselt number (Nu_m) at channel Reynolds number of Re_{ch} = 500.00 and the interfacial Reynolds number of Re_{int} = -5.00 (corresponding to suction).

CHAPTER 5. RESULTS

5.1. TRENDS OF SHERWOOD NUMBER

5.1.1. Effect of Droplets

5.1.1.1. Single-droplet

Figure 28 shows variations of Sherwood number in the flow direction as a function of Pe at r^* = 0.29. The Sherwood number goes through a maximum, then a minimum, followed by another maximum. The maximum Sherwood number downstream of the droplet is referred to as $Sh_{1,max}$ and is significant as it indicates how far downstream the droplet effect persists. At the lowest Pe, there is no detectable overshoot of Sherwood number downstream of the droplet. It can be inferred that there is a need for a minimum Pe to achieve an overshoot of Sherwood number.

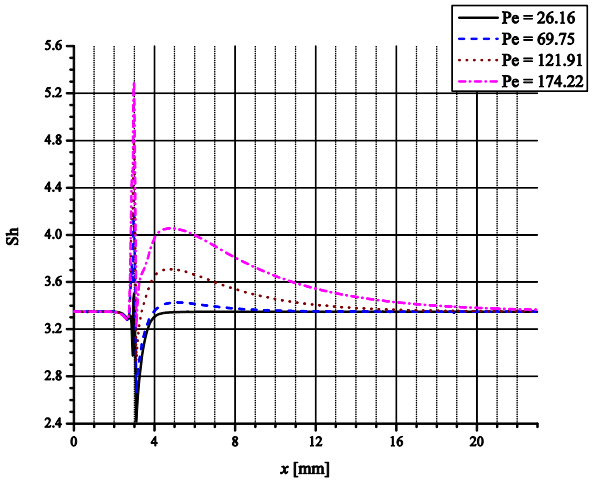

Figure 28: The effect of Péclet number (Pe) on the Sherwood number (Sh) for the non-dimensional droplet radius, r^* = 0.29 (the droplet position, $x_{d,1}$=3.00 mm).

Table 14 shows the variations of $Sh_{1,max}$ and the values of 3.349 indicate the cases that do not lead to any overshoot of Sh downstream of a droplet. The case Pe = 139.51 and r^* = 0.29 leads to

the highest $Sh_{1,max}$. All tabulated values of $Sh_{1,max}$ increase with r^* and Pe except in one case (Pe = 69.75 and r^* = 0.35). This irregularity will be discussed in Section 5.1.1.4.1.

Table 14: The maximum Sh downstream of a droplet ($Sh_{1,max}$) as a function of Péclet number (Pe) and non-dimensional droplet radius (r^*). (The empty cells indicate the cases that were not simulated due to droplet deformation.)

r^*	Pe				
	26.16	69.75	121.91	139.51	261.42
0.20	3.349	3.362	3.385	3.412	3.461
0.24	3.349	3.379	3.449	3.538	
0.29	3.349	3.428	3.710	4.055	
0.35	3.349	3.391	4.001		
0.39	3.353	3.465			

5.1.1.2. Two-droplets

Two droplets studies were conducted to show the effect of droplet spacing on Sherwood number. The goal was to present relatively large increases in Sherwood number in the wake of both droplets to easily highlight how much Sherwood number can differ in PEMFC air flow channels. Hence, the cases to be simulated in this section were chosen according to the Sherwood number values downstream of the single-droplet cases. Locations of 1.00, 2.00, and 5.00 mm (non-dimensional: Δx_d^* = 1.96, 3.92, and 9.80, respectively) downstream of the droplet were checked for at least 5% of Sherwood number increase. The cases satisfying this condition at all of the checked locations were Pe = 121.91 for r^* = 0.29 and 0.35, and Pe = 174.22 for r^* = 0.24 and 0.29.

Figure 29 demonstrates the effect of droplet spacing on Sh for the case Pe = 174.22 and r^* = 0.29. In particular, the overshoot of Sherwood number in the wake of the second droplet, ($Sh_{2,max}$) is shown and $Sh_{2,max}$ is used to compare the effect of spacing in different cases. The effect of droplet spacing on Sherwood number was consistent among all sets of Pe and r^*. The droplet spacing Δx_d=2.00 mm leads to the highest $Sh_{2,max}$, followed by the spacing values of Δx_d=5.00 mm and 1.00 mm.

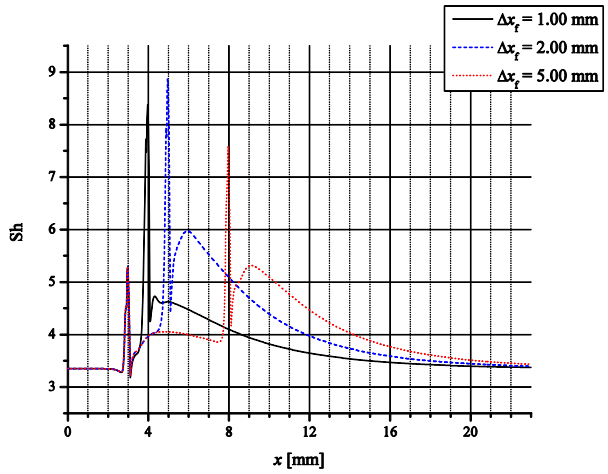

Figure 29: The effect of droplet spacing (Δx_d) on the Sherwood number (Sh) for two consecutive droplets at Péclet number, Pe = 174.22 and the non-dimensional droplet radius, r^* = 0.29 (the first and the second droplet positions: $x_{d,1}$ = 3.00 mm and $x_{d,2} = x_{d,1}+\Delta x_d$, respectively).

To characterize the effect of droplet spacing, overshoot values of Sherwood number in the two droplet wakes ($Sh_{n,max}$) were compared against each other by defining a Sherwood number enhancement factor ($Sh_{2,max}/Sh_{1,max}$). Table 15 shows this enhancement factor of Sherwood number by the second droplet. The highest enhancement factor among all was achieved by the case Pe = 174.22, r^* = 0.29, and Δx_d = 2.00 mm. For each condition of Pe and r^*, the highest respective enhancement factor was achieved when Δx_d was 2.00 mm. The second highest enhancement factor for a particular Pe and r^* condition was not consistently achieved by Δx_d = 1.00 mm or 5.00 mm. Only the condition of Pe = 121.91 and r^* = 0.35, Δx_d = 1.00 mm led to the second highest enhancement factor.

Table 15: The enhancement factor of Sherwood number by the second droplet ($Sh_{2,max}/Sh_{1,max}$) as a function of droplet spacing (Δx_d) and given for different Péclet number (Pe) and non-dimensional droplet radius (r^*) cases.

Pe	r^*	Δx_d [mm]		
		1.00	2.00	5.00
121.91	0.29	1.081	1.194	1.093
121.91	0.35	1.140	1.249	1.113
174.22	0.24	1.052	1.133	1.088
174.22	0.29	1.141	1.473	1.311

5.1.1.3. Multiple-droplets

5.1.1.3.1 *Sherwood number trends based on the critical superficial air velocity*

The effect of multiple droplets was characterized with the down-the-channel-averaged Sherwood number (Sh_{av}). The value of Sh_{av} can be larger or smaller than the fully developed value (Sh_{FD}=3.349) depending on the Péclet number (Pe) with respect to the critical Pe. The critical value of Pe changes slightly with the set of droplet size and spacing. The values of Sh_{av} among the droplets were found to be lower than Sh_{FD} at a Pe lower than the critical value.

Values of Sh_{av} for a non-dimensionalized droplet radius of r^* = 0.39 were compared against each other as the Péclet number was varied from 26.16 to 69.75 at each given uniform droplet spacing. Figure 30 shows the Sh_{av} profiles at r^* = 0.39, Δx_d^* = 1.96, and Pe = 26.16 and 69.75. The case of Pe = 26.16 led to a decrease in Sh_{av} with respect to the fully developed value. Contrarily, the case Pe = 69.75 led to an increase. The variations of Sh_{av} were reduced considerably by the fourth droplet. In between the last two droplets, $Sh_{av,10}$ ($Sh_{av,N-1}$) was 24.6% higher at Pe = 69.75 compared to Pe = 26.16. At other values of non-dimensional droplet spacing (Δx_d^* = 3.92 and 9.80), the $Sh_{av,N-1}$variation between of the corresponding Pe values was less than the reported one for Δx_d^* = 1.96.

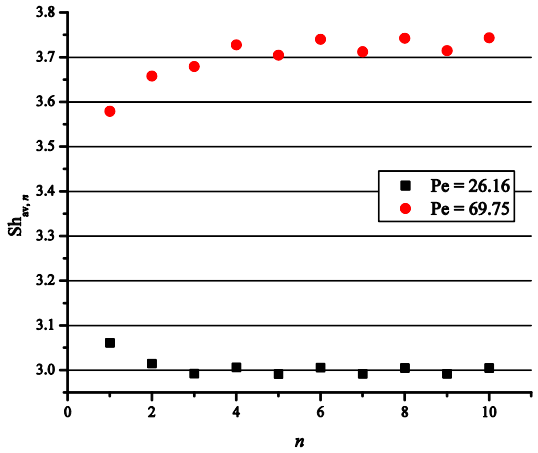

Figure 30: The down-the-channel-averaged Sherwood number ($Sh_{av,n}$) for the non-dimensional droplet radius $r^* = 0.39$, uniform droplet spacing $\Delta x_d^* = 1.96$, and Péclet number Pe = 26.16 and 69.75.

5.1.1.3.2 *The effect of droplet spacing on the Sherwood number*

Figure 31 shows the effect of uniform droplet spacing on Sh and Sh_{av} while r^* and Pe are 0.29 and 69.75, respectively. The number of simulated droplets (N) was 11 for $\Delta x_d^* = 1.96$ and 3.92, and 5 for $\Delta x_d^* = 9.80$. Figure 31a uses a non-dimensional distance parameter to show variations of Sh for all droplet spacing values in a common domain. The non-dimensional distance parameter (x^*) expresses the first droplet position to be zero and the distance relative to the first droplet is normalized with Δx_d : $x^* = (x - x_{d,1}) / \Delta x_d$.

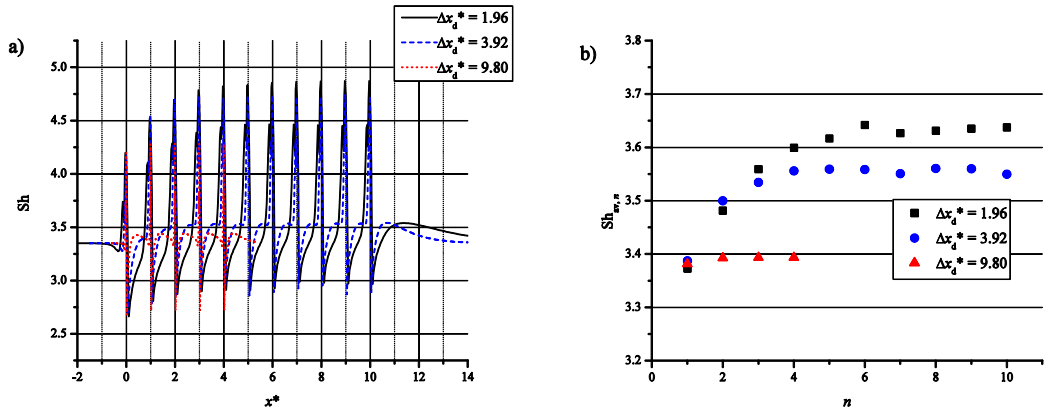

Figure 31: The effect of uniform non-dimensional droplet spacing (Δx_d*) on the Sherwood number (Sh) and down-the-channel-averaged Sh ($Sh_{av,n}$) at the Péclet number, Pe = 69.75, non-dimensional droplet radius, r* = 0.29: a) Sh against the non-dimensional distance parameter (x* = (x - $x_{d,1}$) / Δx_d); b) $Sh_{av,n}$ against the droplet number in the flow direction (n).

Local variations of Sh in Figure 31a are averaged in down the channel direction into $Sh_{av,n}$. Figure 31b shows values of $Sh_{av,n}$ corresponding to the averaged values of Sh between the n and n+1st droplets. The values of $Sh_{av,n}$ reach an asymptotic value ($Sh_{av,\infty}$) towards the channel exit. In this particular case, $Sh_{av,\infty}$ is inversely proportional to Δx_d*. However, it will later be shown that no such linear proportionality exists for all cases. The rate of Sh_{av} convergence to the respective asymptotic value was observed to be higher with Δx_d*. The analysis of the entire data set will show in Section 5.2.1.2. that this conclusion is applicable to all cases.

5.1.1.3.3 *The asymptotic Sherwood number*

Among all the simulated cases, the maximum change of Sh_{av} in between the last two sets of consecutive droplets was less than 2.0% except the case r* = 0.20, Pe = 261.42, and Δx_d* = 9.80 with a change of 3.4%. The reported change in Sh_{av} values show that the selected number of droplets was high enough to achieve Sh_{av} convergence for any uniform droplet spacing. The converged value is called the asymptotic Sh_{av} ($Sh_{av,\infty}$). Table 16 - Table 18show values of $Sh_{av,\infty}$ for all simulated cases while each table is given for a Δx_d*. There are sets of r* and Pe values leading to $Sh_{av,\infty} < Sh_{FD}$. The remaining sets of r* and Pe lead to the opposite condition of $Sh_{av,\infty} > Sh_{FD}$. There is no critical value of r* that can clearly distinguish $Sh_{av,\infty}$ values with respect to

Sh_{FD}. However, the range of Pe = 52.32 – 69.75 can be used to separate the entire Pe range into three.

Table 16: Asymptotic values of down-the-channel-averaged Sherwood number ($Sh_{av,\infty}$) at the uniform non-dimensional droplet spacing of $\Delta x_d^* = 1.96$ as a function of non-dimensional droplet radius (r^*) and Péclet number (Pe).

r^*	Pe								
	13.16	26.16	34.88	52.32	69.75	121.91	139.51	174.22	261.42
0.20	3.118	3.110	3.114	3.152	3.236	3.794	4.200	4.536	5.292
0.24	3.050	3.045	3.062	3.153	3.335	4.409	4.830	5.525	
0.29	2.967	2.983	3.023	3.232	3.638	5.601	6.198	6.995	
0.35	2.927	2.973	3.007	3.164	3.590	6.106	6.792		
0.39	2.925	3.005	3.085	3.335	3.743				

In the range of Pe < 52.32, $Sh_{av,\infty}$ values are always smaller than Sh_{FD}. These values can be as low as $0.87Sh_{FD}$. As shown by Figure 32 and supported by Table 16 - Table 18, $Sh_{av,\infty}$ increases with Δx_d^*. Figure 32 also shows the quadratic relation between $Sh_{av,\infty}$ and r^* at three Δx_d^* values. Values of $Sh_{av,\infty}$ first decrease with r^*, reach a minimum value, and then increase. In Figure 32a, the family of plots at Pe = 13.16 shows one symmetric half of a quadratic function. In Figure 32b, data points exist at both sides of the minimum $Sh_{av,\infty}$ at Pe = 26.16. This is due to the position of the $Sh_{av,\infty}$ minimum shifting towards smaller values of r^* with increasing Pe. The same shift happens consistently as Pe is increased to 34.88.

Table 17: Asymptotic values of down-the-channel-averaged Sherwood number ($Sh_{av,\infty}$) at the uniform non-dimensional droplet spacing of $\Delta x_d^* = 3.92$ as a function of non-dimensional droplet radius (r^*) and Péclet number (Pe).

r^*	Pe								
	13.16	26.16	34.88	52.32	69.75	121.91	139.51	174.22	261.42
0.20	3.235	3.227	3.227	3.242	3.281	3.628	3.838	4.391	6.113
0.24	3.199	3.198	3.205	3.249	3.349	4.191	4.680	5.861	
0.29	3.162	3.171	3.190	3.300	3.550	5.356	6.130	7.438	
0.35	3.150	3.186	3.207	3.268	3.511	5.759	6.498		
0.39	3.153	3.217	3.271	3.392	3.547				

Table 18: Asymptotic values of down-the-channel-averaged Sherwood number ($Sh_{av,\infty}$) at the uniform non-dimensional droplet spacing of $\Delta x_d^* = 9.80$ as a function of non-dimensional droplet radius (r^*) and Péclet number (Pe).

r^*	Pe								
	13.16	26.16	34.88	52.32	69.75	121.91	139.51	174.22	261.42
0.20	3.303	3.301	3.301	3.305	3.316	3.396	3.444	3.573	4.074
0.24	3.290	3.289	3.291	3.305	3.380	3.540	3.663	4.021	
0.29	3.274	3.279	3.286	3.321	3.393	3.968	4.299	5.171	
0.35	3.270	3.289	3.302	3.327	3.397	4.225	4.681		
0.39	3.270	3.301	3.329	3.388	3.443				

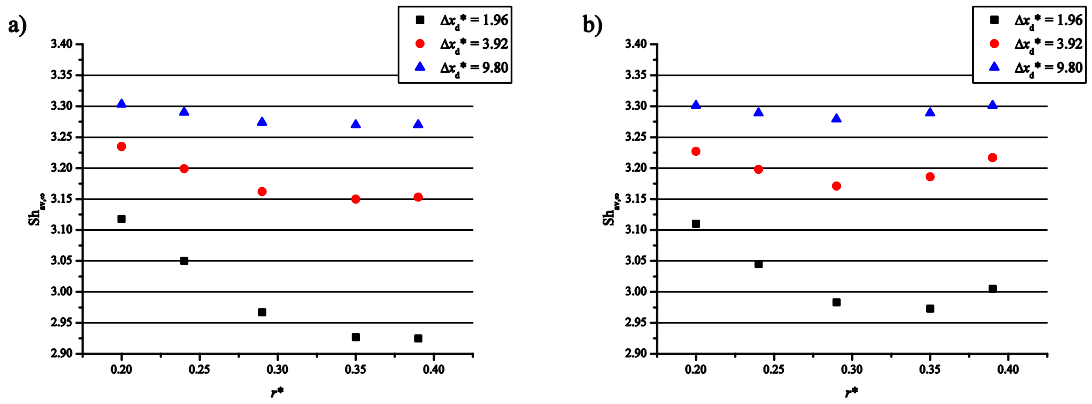

Figure 32: The quadratic behavior of $Sh_{av,\infty}$ with the non-dimensional radius (r^*) at the Péclet number of a) Pe = 13.16 and b) Pe = 26.16.

In the range of Pe > 69.75, $Sh_{av,\infty}$ values are always larger than Sh_{FD}. Values can be as high as $2.22Sh_{FD}$. Family of plots in Figure 33 and Table 16 - Table 18 show that $Sh_{av,\infty}$ is always the lowest at $\Delta x_d^* = 9.80$ compared to the other two Δx_d^*. However, $Sh_{av,\infty}$ can reach its highest value at a different Δx_d^* value (1.96 or 3.92) based on the remaining set of parameters: r^* and Pe. There is also a strong decrease of $Sh_{av,\infty}$ observed with Δx_d^* approaching 9.80. Values of $Sh_{av,\infty}$ are linearly dependent on r^*. This dependency is valid for the entire range of Pe > 69.75. Moreover, $Sh_{av,\infty}$ increases consistently with Pe. This relationship manifests itself by increasing the slope of $Sh_{av,\infty}$ - r^* plots with Pe.

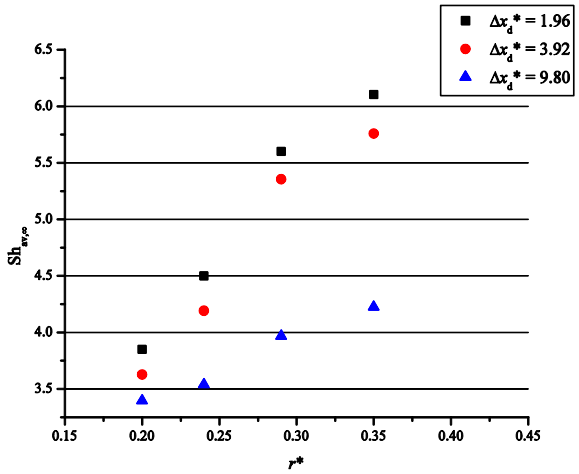

Figure 33: The linear behavior of $Sh_{av,\infty}$ with the non-dimensional radius (r^*) at the Péclet number of Pe = 121.91.

In the range of $52.32 \leq Pe \leq 69.75$, a transition happens from the trend at $Pe < 52.32$ to the one at $Pe > 69.75$. For instance, values of $Sh_{av,\infty}$ inconsistently decrease when r^* makes a transition from 0.29 to 0.35 at Pe = 69.75. Under these transitions, it is not possible express the changes in $Sh_{av,\infty}$ with consistent relationships. The values of $Sh_{av,\infty}$ deviate from Sh_{FD} at most 11% in this Pe range. Consequently, a constant value of Sh_{FD} can be assumed in an application within this Pe range.

5.1.1.4. Effect of single and multiple droplets on the velocity and O_2 concentration profiles

5.1.1.4.1 *Effect of a single droplet*

To understand the reported results in Section 5.1.1. , the following additional background provides useful insight. In this numerical study, the enforced constant O_2 flux boundary condition ensures a constant O_2 concentration gradient at the GDL-air channel interface. The mean O_2 concentration of the flow is independent of flow conditions and will change linearly in the flow

direction. The only unknown required to calculate Sh is the mean concentration at the interface. This value is dependent on the local flow conditions and calculated numerically. The Sherwood number is calculated to be higher with the increasing interfacial concentration. Figure 34 shows how a droplet affects the air flow in the case u_m = 10.59 m s^{-1} (Pe = 174.22) and r = 0.15 mm (r* = 0.29). While Figure 34a focuses on the velocity field, Figure 34b complements the understanding of Figure 34a with the concentration field.

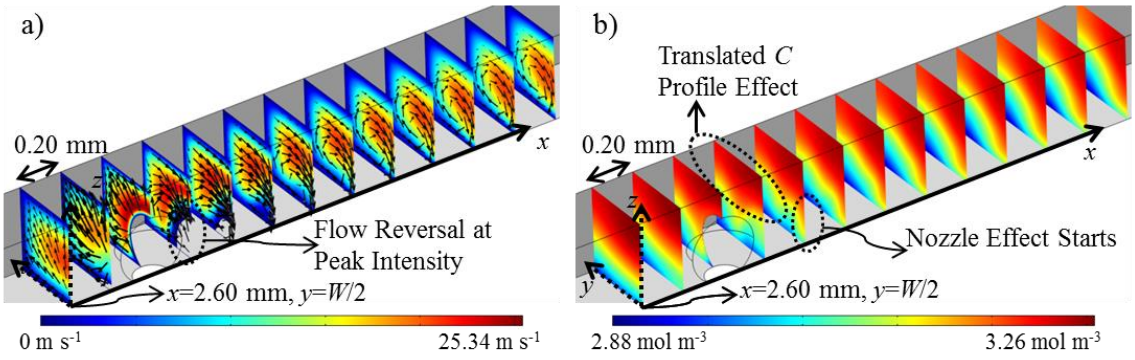

Figure 34: The flow conditions for the superficial mean air velocity u_m = 10.59 m s^{-1}, and the droplet radius, r = 0.15 mm. yz direction of the velocity is shown by arrows of which lengths are logarithmically proportional with the velocity magnitude in the yz cross section. Each slice is separated for 0.20 mm, and the color map corresponds to a) $+x$ velocity magnitude ($-x$ velocity areas are left blank on the slices), and b) O_2 concentration (C).

Figure 34a shows a map of the velocity magnitude in the $+x$ direction at given slices that are separated from each other by 0.20 mm. The regions in slices with an incomplete filling correspond to a flow in the $-x$ direction (flow reversal). The flow reversal can be seen at slices x = 2.80, 3.20 and 3.40 mm. The arrows on the slices show the direction of the flow in the yz plane. The lengths of the arrows are logarithmically proportional to the velocity magnitude in a yz cross section. The air closer to the symmetry line on the interface (y = W/2 and z = 0) is brought back from x = 3.40 mm towards the droplet and recirculated back to the high velocity region at x = 3.20 mm. The high velocity region is directed towards the symmetry line on the interface ($-z$

direction). Moreover, downstream of x = 3.40 mm, the air starts to recirculate around the $+x$ axis close to the symmetry line on the interface.

Figure 34b shows the impact of the velocity field on the concentration profile. Upstream of the droplet, the concentration does not show a significant variation along the channel width (the y direction). However, in the immediate droplet wake (x = 3.20 mm), the symmetry line and channel corner on the interface ($y = W$ and $z = 0$) show a lower concentration of O_2. The low concentration leads to a reduction in Sh. The shifting of the high concentration region away from the interface is referred to here as the translated concentration profile effect. The O_2 rich air closer to the top channel wall ($z = H$), is directed to the symmetry line on the interface by a strong convection at $x \geq 3.40$ mm. The strong convection that brings O_2-rich air towards the interface is referred to here as the nozzle effect. In the flow direction, the nozzle effect transforms into a recirculation around $+x$ axis. The recirculation distributes O_2 towards the channel bottom corner. The Sherwood number increases as a result of the aforementioned convective effects. The recirculation does not affect the channel corners strongly. Hence, the recovery of the O_2 profile at the bottom channel corner depends on the diffusion more than at the symmetry line.

5.1.1.4.2 *Effect of multiple droplets*

Figure 35 provides insight about how the local Sh increases with the introduction of droplets at high Pe. The conditions in Figure 35 are Pe = 261.42, r^* = 0.20, and Δx_d^* = 3.92. Figure 35a shows an air streamline in the symmetric half of the channel. For providing distinguishable images of droplets, one droplet is skipped to be shown for every other shown droplet. The streamline follows a straight line path upstream of the droplets. Downstream of the droplets, the streamline follows a helical path. In down the channel direction, air rotates around $+x$ axis that goes through the center of the helical path. This helical path of the air flow alters the local Sh. The alteration can be understood with the normalized oxygen concentration profile in the channel.

Figure 35b shows two *yz* cross sections taken at the channel inlet and in between the fifth and sixth droplets. The O_2 concentration is normalized with the mean concentration at the respective cross sections (C/C_m). Down the channel, the helical air flow path brings the high O_2 concentration from the vicinity of the top wall towards the GDL-channel interface as shown in Figure 35b. In this particular case, the Sherwood number is increased since the O_2 concentration at the interface is increased.

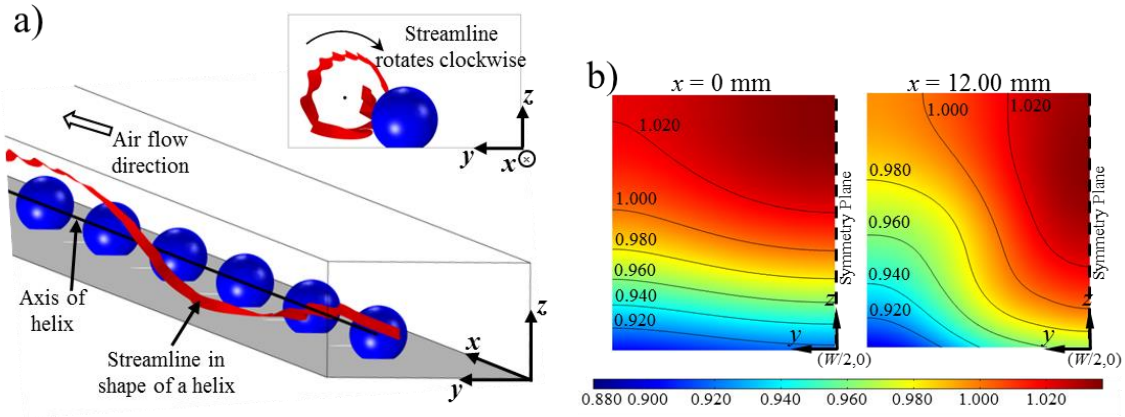

Figure 35: The effect of helical air flow path on local O_2 concentration profile: The Péclet number Pe = 261.42, non-dimensional droplet radius r^* = 0.20, non-dimensional uniform droplet spacing Δx_d^* = 3.92. a) The streamline originated at x = 0, y = 0.10 mm, z = 0.15 mm; b) Oxygen concentration normalized with the mean concentration (C/C_m) at a *yz* cross section from the symmetric half of the channel. C_m is 3.520 and 3.394 mol m^{-3} at x = 0 and 12.00 mm, respectively.

Figure 36 provides an explanation for the decrease of Sh below the Sh_{FD} value at low Pe values. As a representative condition, Pe, r^*, and Δx_d^* are selected to be 13.16, 0.39, and 1.96, respectively in Figure 36. Figure 36a shows streamlines that are placed at z = 0.19 mm that is slightly below the half-height of the channel ($H/2$ = 0.20 mm) and evenly distributed along the channel width. The streamlines creep over the top of the droplets since their originating height is slightly above the *xy* plane that crosses the droplet from its widest cross section (z = 0.17 mm). Among the consecutive droplets, no streamlines are directed towards the GDL-air channel interface. The effect of this flow pattern on the normalized O_2 profile is shown in Figure 36b. The

fully developed concentration profile is compared against the one in the wake of the 9th droplet at x = 11.50 mm. It can be seen that the normalized O_2 concentration at the interface is reduced due to droplets, a condition opposite to the one in high Pe.

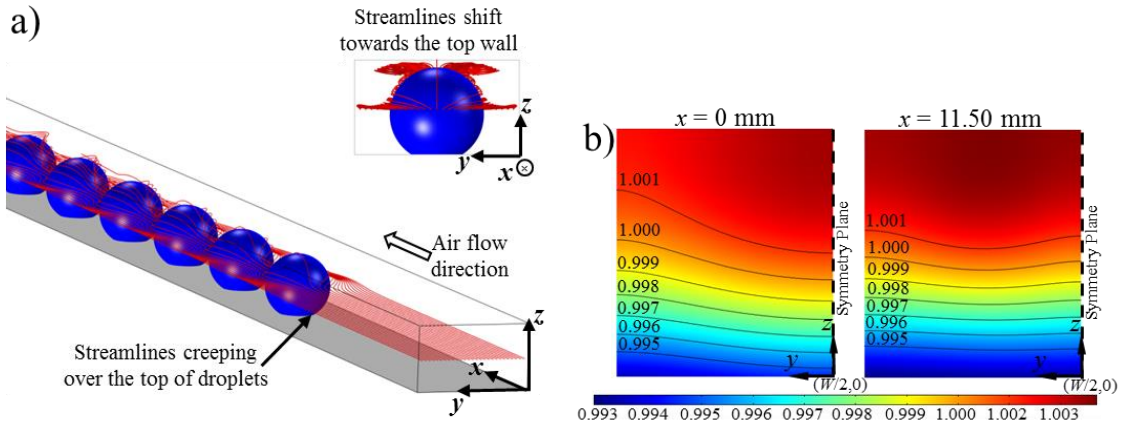

Figure 36: The effect of creeping air flow over the droplets on local O_2 concentration profile: The Péclet number Pe = 13.16, non-dimensional droplet radius r^* = 0.39, and non-dimensional uniform droplet spacing Δx_d^* = 1.96. a) Streamlines originated at x = 0, 0 < y < 0.70 mm, z = 0.19 mm; b) Oxygen concentration normalized with the mean concentration (C/C_m) at a yz cross section from the symmetric half of the channel. C_m is 3.626 and 3.464 mol m^{-3} at x = 0 and 11.50 mm, respectively.

5.1.1.5. Estimation of the effect of the Sherwood number variations on cell performance

The effect of multiple droplets on the cell performance is a function of the O_2 concentration drop from the channel mean (C_m) to the average interfacial value ($C_{int,av} = W^{-1}\int_{y=0}^{W} C_{int} dy$). The difference between C_m and $C_{int,av}$ adversely affects the cell voltage for a given current density. Figure 37 shows C_m and $C_{int,av}$ at the current density of 1.5 A cm^{-2} and, Pe of 26.16 and 174.22. C_m varies from 3.83 to 1.92 mol m^{-3} at the inlet and outlet, respectively. This variation does not depend on Pe since the stoichiometry is kept at 2. Figure 37 focuses on the first 21.00 mm of the channel. Values of $C_{int,av}$ vary with Pe while r^* and Δx_d^* are 0.29 (0.15 mm) and 3.92 (2.00 mm), respectively. Both plots of $C_{int,av}$ have the same fully developed concentration drop

upstream of the first droplet (x < 3.00 mm) and the average slope of C_m. $C_{int,av}$ at Pe = 26.16 follows the trend of the fully developed region in between the droplets. In the immediate proximity of droplets, $C_{int,av}$ decreases with respect to the fully developed line. $C_{int,av}$ at Pe = 174.22 shows an increase with respect to the fully developed line. This results in a smaller concentration drop at the interface and thereby, an increase in the performance of the fuel cell.

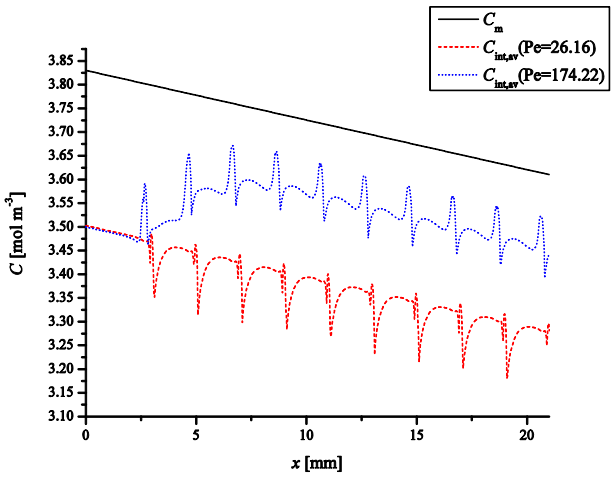

Figure 37: The comparison between O_2 concentration drop from the channel cross sectional mean value (C_m) to interfacial average one ($C_{int,av}$) at two different Péclet numbers: 26.16 and 174.22. Non-dimensional droplet radius and uniform spacing are 0.29 (0.15 mm) and 3.92 (2.00 mm), respectively.

The varying O_2 concentration drop at the GDL-channel interface affects the voltage drop in the fuel cell. Eq. (30) determines the decrease in voltage due to a decrease in O_2 concentration in the cathode catalyst layer (CL). The calculations focus on the channel outlet since the transport losses will be more severe there. The O_2 concentration at the CL was calculated by applying reductions to the O_2 concentration at the channel outlet (1.92 mol m^{-3}) at the interface and within the GDL. Eq. (30) uses Faraday's (F_c) and universal gas (R_u) constants with respective values of 96,485 C mol^{-1} and 8.314 J mol^{-1} K^{-1}. C_1 and C_2 represent two values of O_2 concentration in the cathode CL. The resulting voltage change due to this concentration difference is expressed with $\Delta V_{1\text{-}2}$.

$$\Delta V_{1-2} = \frac{R_u T}{F_c} \ln\left[\frac{C_2}{C_1}\right] \quad (30)$$

For the calculations of O_2 concentration loss within the GDL, the PEMFC was assumed to have a dry, 200 μm thick GDL with an O_2 diffusivity of $D_{O2\text{-}GDL} = D_{O2\text{-}air}/1.5$ [13]. The Fick's diffusion of O_2 in the GDL causes 0.65 mol m^{-3} of an O_2 concentration drop at the current density of 1.5 A cm^{-2}.

For the calculation of interfacial O_2 concentration drop, three values of Sh are used: the fully developed: Sh_{FD} = 3.349, the minimum: $Sh_{av,\infty}$ = 2.925, and the maximum: $Sh_{av,\infty}$ = 7.438. The minimum and maximum values of $Sh_{av,\infty}$ were not obtained at the Pe value equivalent to the current density of 1.5 A cm^{-2}. However, due to possible flow maldistribution in parallel flow channels, it is safe to consider the possibility that those Sh values may exist at the aforementioned current density. Values of Sh were transformed into the interfacial O_2 concentration drop (ΔC) with the following dimensionalization process: $\Delta C = j\ (\mathrm{Sh}\ D_{O2\text{-}air}\ d_h^{-1})^{-1}$ in which j was 6.663×10^{-2} mol m^{-2} s^{-1}.

The voltage drop due to the inclusion of fully developed interfacial O_2 resistance is 9.0 mV. Since the minimum $Sh_{av,\infty}$ is lower than the fully developed value, this case creates an additional voltage drop of 1.6 mV. The maximum $Sh_{av,\infty}$ reduced the original voltage drop 5.3 mV which is a 58.9% reduction in the voltage drop. The findings suggest that the variations in Sh can lead to non-negligible variations in cell voltage at the current density of 1.5 A cm^{-2}. This effect can be stronger at higher current densities.

5.1.2. Effect of Injection/Suction at the GDL-Air Channel Interface

5.1.2.1. Effect of injection and suction on Sherwood number in an isolated channel

In the baseline condition, in which there is no injection or suction at the GDL-air channel interface, fully developed Sherwood number was obtained to be $Sh_{FD,0}$ = 3.35. This value was also obtained for all injection/suction cases shown in Table 2. Therefore, it can be claimed that injection and suction due to oxygen consumption or vapor generation are not strong enough to alter baseline fully developed Sherwood number.

Table 19 presents fully developed Sherwood numbers calculated at injection ($Sh_{FD,inj}$) and suction ($Sh_{FD,suc}$) conditions and normalized with the baseline value, $Sh_{FD,0}$. The results are presented as a function of absolute interfacial Reynolds number ($|Re_{int}|$). Since Re_{int} changes its sign at injection and suction conditions, the absolute value of Re_{int} is utilized. When suction has an intensity larger than 0.4 (Re_{int} < -0.4), advection overtakes diffusion. Hence, Table 19 compares Sh up to $|Re_{int}|$ = 0.4. The lowest $|Re_{int}|$ was selected as the highest $|Re_{int}|$ from Table 2. Since all $|Re_{int}|$ values in Table 2 led to the same result, the highest value is representative of other $|Re_{int}|$ values.

Table 19: Values of fully developed Sherwood number in injection ($Sh_{FD,inj}$) and suction ($Sh_{FD,suc}$) conditions ($|Re_{int}| \leq 0.4$) normalized with baseline fully developed value ($Sh_{FD,0}$).

$\|Re_{int}\|$	5.01×10^{-2}	10^{-1}	2×10^{-1}	4×10^{-1}
$Sh_{FD,inj}/Sh_{FD,0}$	1.00	0.99	0.98	0.96
$Sh_{FD,suc}/Sh_{FD,0}$	1.00	1.01	1.02	1.03

Table 19 leads to the conclusion that suction cannot lead to a significant change in Sherwood number under conditions that diffusion is not completely replaced by advection due to strong suction.

Table 20 extends the intensity of injection to a Re_{int} value of 5 and shows Sherwood number as a function of Re_{int}. By analyzing the data in Table 19 and Table 20 together, it can be seen that

Sherwood number deviates from the fully developed value at least 11% when injection Re_{int} exceeds 1. For the entire range of injection shown in Table 19 and Table 20, a linear variation of Sherwood number is seen. The same trend is valid for the suction cases in Table 19. Moreover, all values in Table 19 and Table 20 match with the correlation provided by Beale [62].

Table 20: Values of fully developed Sherwood number in injection ($Sh_{FD,inj}$) conditions ($6\times10^{-1} \leq |Re_{int}| \leq 5$) normalized with baseline fully developed value ($Sh_{FD,0}$).

$\lvert Re_{int} \rvert$	6×10^{-1}	8×10^{-1}	1	2.5	5
$Sh_{FD,inj}/Sh_{FD,0}$	0.93	0.91	0.89	0.73	0.52

The results in this section justify the approach of simulating Sherwood number by neglecting the injection/suction due to electrochemical reactions. It has been shown injection/suction at the GDL-channel interface is too weak to lead to significant changes in Sherwood number.

5.1.2.2. Effect of a droplet on Sherwood number in a channel coupled with GDL

A single droplet was placed in a channel with a GDL adjacent to it. Flow could go through the GDL as the channel was constricted by the droplet. The average interfacial velocity induced by the droplet is expressed by interfacial Reynolds number (Re_{int}). Figure 38 shows a typical interfacial velocity profile from the case Re_{ch} = 275.15 and r = 0.15 mm. Upstream of the droplet (x<3.00 mm), suction can be seen with the maximum intensity of nearly Re_{int}=-10. Downstream of the droplet (x>3.00 mm), injection is present with a maximum intensity almost half of the suction. Injection, downstream of the droplet is more evenly distributed along the length of the channel compared to the suction upstream.

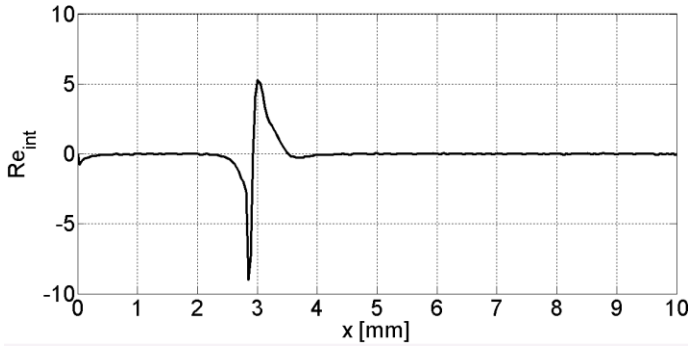

Figure 38: Induced injection and suction by the droplet with a radius of r = 0.15 mm at a channel based Reynolds number of Re_{ch} = 275.15. Droplet induced injection/suction is expressed by interfacial Reynolds number (Re_{int}).

The highest intensity of suction and injection was obtained in the case of Re_{ch} = 412.85 and r = 0.10 mm with the corresponding values of Re_{int} = -9.6 and 5.6, respectively. The lowest intensities were obtained in Re_{ch} = 110.16 and r = 0.20 mm with the intensities of Re_{int} = -3.0 and 2.9, respectively. All the aforementioned intensities of injection and suction led to significant changes in Sh_{FD} as presented in Table 20. The Sh variation in the vicinity of the droplet was analyzed with expectations parallel to results in Table 20.

Figure 39 compares local Sherwood number variations under conditions of Re_{ch}=275.15 and r=0.15 mm for channel-only and channel-GDL simulations. The fully developed Sherwood number under zero injection/suction ($Sh_{FD,0}$) differed slightly. Channel-only and channel-GDL cases led to $Sh_{FD,0}$ of 3.35 and 3.20, respectively. Local Sh values are normalized with the respective $Sh_{FD,0}$ to provide a better comparison ground.

Results in Figure 39 show that injection and suction caused led to increase and decrease, respectively in the immediate vicinity of the droplet. This trend was seen in all three configurations of Re_{ch} and r. Contrarily, an opposite trend was obtained in Section 5.1.2.1. when injection/suction was enforced as a boundary condition. Therefore, velocity profile caused by the droplet is a stronger effect than the local injection and suction. This trend is consistent in the remaining two cases.

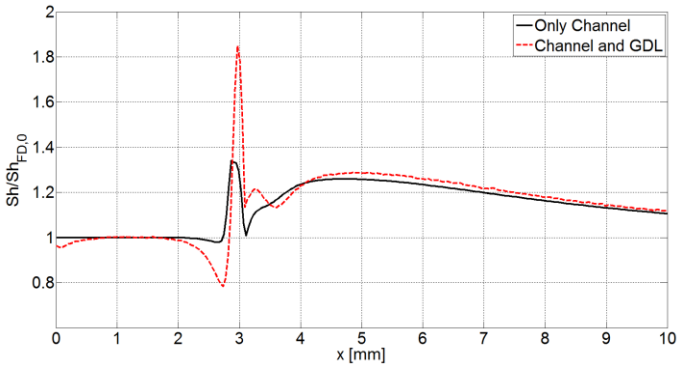

Figure 39: Normalized local Sherwood numbers (Sh) with the respective zero injection/suction fully developed values ($Sh_{FD,0}$). Changes induced by a droplet with a radius of 0.15 mm at channel based Reynolds number of 275.15. Comparison made between channel-only and channel-GDL simulations.

With the addition of the GDL into the simulation, the local maximum of Sherwood number that is seen in the wake of the droplet was increased negligibly in all simulated configurations of Re_{ch} and r. This maximum Sherwood number affects a significant channel length downstream. The negligible change in this parameter allows the investigation of two-phase flow Sherwood number in isolated air channels by neglecting the GDL effect.

5.1.3. Effect of Films

5.1.3.1. Zero-length films (corner droplets)

The first set of simulations was performed for zero length (L_f = 0) films. They represent the initial stage of a droplet emerging from the GDL-channel corner and contacting the channel top wall. Figure 40 shows two trends in Sherwood number (Sh) among the simulated cases. Figure 40a and Figure 40b show cases with absence and presence of Sh overshoot, respectively. The presence of the overshoot is a function of Péclet number (Pe) and non-dimensional film width (W_f*). The characteristic points on the plots are annotated in Figure 40. In the film wake, a Sh minimum (Sh_{min}) is observed at the position, x_{min}. In certain cases, this minimum is followed by a maximum (Sh_{max}) at the position, x_{max}. When within 1% range, Sh was assumed to converge to $Sh_{FD,ch}$.

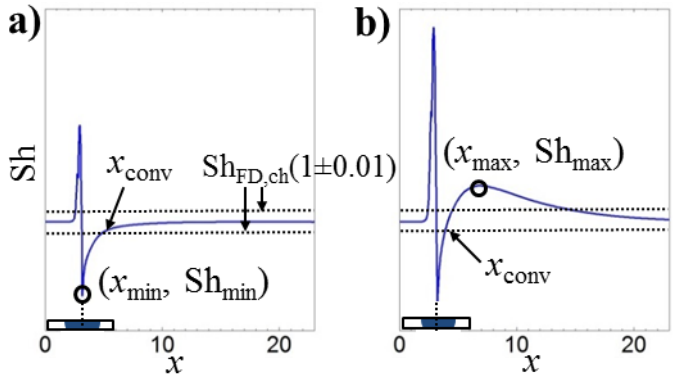

Figure 40: Characteristic points are shown in two scenarios of Sherwood number (Sh) profile due to a single film with zero length (L_f = 0): a) No Sh overshoot, b) Overshoot of Sh.

The presence of Sherwood number overshoot in the film wake was only seen in the shortest film length (L_f = 0), and high Pe and W_f* values. The highest maximum Sherwood number in the film wake (Sh_{max}) was simulated to be 3.46 at the conditions Pe = 174.22 and W_f* = 0.78. Since this value corresponds only to a 3% increase above $Sh_{FD,ch}$, the conditions that lead to Sh overshoot were post-processed without reporting Sh_{max} values.

Table 21 and Table 22 respectively show Sh_{min} and the distance required to converge to $Sh_{FD,ch}$ downstream of Sh_{min}. The aforementioned variables are presented at fewer points in between the maximum and minimum Pe values compared to the complete set of simulated Pe values. The number of data points presented was reduced as they are sufficient to show the trends. The correlations to be presented will cover the entire set of data points simulated.

Table 21 shows Sh_{min} normalized with $Sh_{FD,ch}$ = 3.35, $Sh_{min}/Sh_{FD,ch}$, as a function of W_f* and Pe. The values, which range from 0.46 to 0.92, decrease with W_f* and increase with Pe. The emboldened values indicate a Sh overshoot in the film wake as shown in Figure 40b. These cases are the minority since the films detach before the Pe and W_f* can become sufficiently high.

Table 21: Minimum Sh (Sh_{min}) in the film wake normalized with fully developed channel Sh ($Sh_{FD,ch}$), $Sh_{min}/Sh_{FD,ch}$, as a function of Péclet number (Pe) and non-dimensional film width (W_f*). (Emboldened values indicate cases with Sh overshoot. Empty cells indicate conditions in which films detach.)

W_f*	Pe				
	26.16	69.75	121.91	174.22	261.42
0.39	0.78	0.82	0.85	0.88	0.92
0.59	0.64	0.68	0.73	**0.76**	
0.78	0.53	0.58	**0.63**		
0.98	0.46	0.51			

Table 22 shows the distance that is required for Sh to converge to $Sh_{FD,ch}$ ($x_{conv} - x_{min}$). For conditions with no Sh overshoot, this distance, which ranges from 1.51 to 5.33 mm, increases with both Pe and W_f*. The film-affected distances are many times larger than the size of the films inducing this effect. For conditions with Sh overshoot (shown with emboldened values), the distance to reach convergence in $Sh_{FD,ch}$ is shortened drastically. The difference between Figure 40a and Figure 40b exemplifies this shortened convergence length. The term "convergence" is used as a superficial one to refer to the point where the Sh profile crosses $Sh_{FD,ch}$ for the first time. This crossing occurs upstream of the overshoot position. The actual convergence occurs downstream of the overshoot. However, downstream of the overshoot is not an area of interest since the overshoot is not strong enough to diverge from $Sh_{FD,ch}$ significantly.

Table 22: The distance of Sh convergence point with respect to minimum Sh position (x_{conv} - x_{min}) [mm] in the film wake. (Empty cells indicate a condition in which films detach. Emboldened values indicate conditions with Sh overshoot in the film wake.)

W_f*	Pe				
	26.16	69.75	121.91	174.22	261.42
0.39	1.51	2.81	3.94	4.59	3.67
0.59	1.99	4.47	4.80	**1.13**	
0.78	2.48	5.33	**1.51**		
0.98	2.81	5.14			

5.1.3.2. Films with a length larger than zero

Figure 41 shows a typical Sh profile for films with lengths larger than zero ($L_f > 0$). This profile has characteristic points that are shared by films with zero length ($L_f = 0$): x_{max}, x_{min}, and x_{conv}. In addition to these shared points, there is another characteristic point which is specific to films with lengths larger than zero. This point indicates the Sh (Sh_{ext}) in the vicinity of film exit (x_{ext}) where film width starts tapering off to zero from full width (W_f) in the flow direction.

Sh on the side of a film ($x_f \leq x \leq x_f+L_f$) exponentially decreases in the flow direction as shown in Figure 24. If the length of the film (L_f) is large enough, the value of Sh_{ext} can reach to a fully developed film Sh ($Sh_{FD,f}$). It is important to underline the difference between $Sh_{FD,f}$ and $Sh_{FD,ch}$. The value of $Sh_{FD,ch}$ is singular and specific to the dry channel cross section of 0.70 mm × 0.40 mm. On the contrary, the value of $Sh_{FD,f}$ is plural and varies with the cross section of the channel that is left after the partial occupancy by a film. For the aforementioned reason, $Sh_{FD,f}$ varies with the film width. Table 23 presents $Sh_{FD,f}$ as a function of W_f*. Values of $Sh_{f,FD}$ are inversely proportional to W_f*.

Table 23: Fully developed film Sherwood number in a sufficiently long film ($Sh_{FD,f}$) with a variable non-dimensional film width (W_f*).

W_f*	0.39	0.59	0.78	0.98
$Sh_{FD,f}$	2.71	2.47	2.33	2.32

A film with non-zero length creates a strong variation of local Sh from its entrance to its exit. Comparison between Sh_{max} and Sh_{ext} can be made using the tables below. The values of Sh_{max} and Sh_{ext} are located in the immediate vicinity of a film inlet and exit, respectively. Hence, the positions of Sh_{max} and Sh_{ext} can be assumed to be $x_{max} = x_f$ and $x_{ext} = x_f+L_f$, respectively.

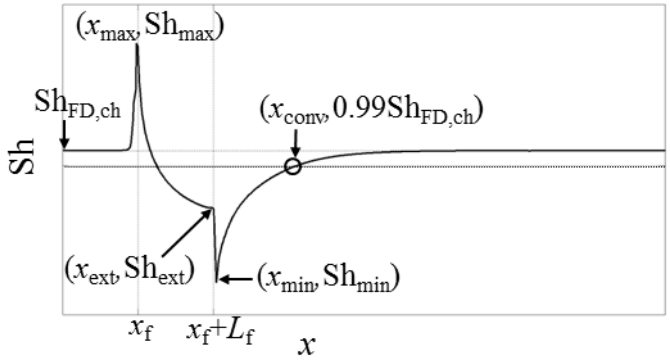

Figure 41: Characteristic points shown on a Sherwood number profile due to a single film with a length larger than zero ($L_f > 0$).

Sh_{max} is independent of film length and a function of Pe and W_f*. Values of Sh_{max} are first normalized with the corresponding $Sh_{FD,f}$ and then presented in Table 24. All $Sh_{max}/Sh_{FD,f}$ values are larger than unity, a result indicating that Sh_{max} is larger than the corresponding $Sh_{FD,f}$. The maximum value of $Sh_{max}/Sh_{FD,f}$ was obtained to be 2.25 at the conditions of Pe = 121.91 and W_f* = 0.78.

Table 24: Maximum Sherwood number (Sh_{max}) upstream of a film that is normalized by fully developed film Sherwood number ($Sh_{FD,f}$): $Sh_{max}/Sh_{FD,f}$.

W_f*	Pe				
	26.16	69.75	121.91	174.22	261.42
0.39	1.25	1.38	1.47	1.55	1.65
0.59	1.43	1.66	1.85	2.00	
0.78	1.58	1.95	2.25		
0.98	1.71	2.19			

Table 25 - Table 27 show Sh_{ext} after it is normalized with the corresponding $Sh_{FD,f}$ for varying L_f*. Sh_{ext} is a function of how much the air flow is developed from the film inlet to exit. Hence, the value is dependent on Pe, W_f*, and L_f*. Both Pe and W_f* increase $Sh_{ext}/Sh_{FD,f}$ while L_f* decreases it. The largest deviation of Sh_{ext} from $Sh_{FD,f}$ is 15%, which occurs at L_f* = 9.80.

Table 25: Film-exit Sherwood number (Sh_{ext}) normalized with the corresponding fully developed film Sherwood number ($Sh_{FD,f}$): $Sh_{ext}/Sh_{FD,f}$. The film length is L_f^* = 1.96 while Péclet number (Pe) and non-dimensional film width (W_f^*) are varied.

W_f^*	Pe				
	26.16	69.75	121.91	174.22	261.42
0.39	1.05	1.13	1.18	1.23	1.29
0.59	1.09	1.21	1.32	1.41	
0.78	1.13	1.32	1.49		
0.98	1.18	1.41			

Table 26: Film-exit Sherwood number (Sh_{ext}) normalized with the corresponding fully developed film Sherwood number ($Sh_{FD,f}$): $Sh_{ext}/Sh_{FD,f}$. The film length is L_f^* = 3.92 while Péclet number (Pe) and non-dimensional film width (W_f^*) are varied.

W_f^*	Pe				
	26.16	69.75	121.91	174.22	261.42
0.39	1.02	1.07	1.12	1.16	1.22
0.59	1.04	1.13	1.22	1.30	
0.78	1.06	1.20	1.34		
0.98	1.09	1.27			

Table 27: Film-exit Sherwood number (Sh_{ext}) normalized with the corresponding fully developed film Sherwood number ($Sh_{FD,f}$): $Sh_{ext}/Sh_{FD,f}$. The film length is L_f^* = 9.80 while Péclet number (Pe) and non-dimensional film width (W_f^*) are varied.

W_f^*	Pe				
	26.16	69.75	121.91	174.22	261.42
0.39	1.00	1.02	1.05	1.05	1.11
0.59	1.00	1.04	1.09	1.09	
0.78	1.01	1.07	1.15		
0.98	1.02	1.11			

Values of $Sh_{min}/Sh_{FD,ch}$ in Table 28 - Table 30 show the same dependency on Pe and W_f^* as observed in zero-length films. Values of $Sh_{min}/Sh_{FD,ch}$ either remain the same or decrease with the non-dimensional film length (L_f^*). When the flow is nearly fully developed on the side of a film (low Pe and low W_f^*), $Sh_{min}/Sh_{FD,ch}$ show either no difference or an insignificant difference with L_f^*. For other conditions, the larger the L_f^* value is the smaller $Sh_{min}/Sh_{FD,ch}$ becomes. The minimum $Sh_{min}/Sh_{FD,ch}$ = 0.39 was obtained at conditions of Pe = 26.16, W_f^* = 0.98, and L_f^* =

3.92 and 9.80. Due to this low value, the Sh convergence length in the film wake has high transport resistance.

Table 28: Minimum Sherwood number (Sh_{min}) in the film wake normalized with fully developed channel Sherwood number ($Sh_{FD,ch}$): $Sh_{ext}/Sh_{FD,ch}$. The film length is L_f^* = 1.96 while Péclet number (Pe) and non-dimensional film width (W_f^*) are varied.

W_f^*	Pe				
	26.16	69.75	121.91	174.22	261.42
0.39	0.72	0.73	0.75	0.77	0.81
0.59	0.59	0.61	0.64	0.67	
0.78	0.50	0.52	0.56		
0.98	0.42	0.45			

Table 29: Minimum Sherwood number (Sh_{min}) in the film wake normalized with fully developed channel Sherwood number ($Sh_{FD,ch}$): $Sh_{ext}/Sh_{FD,ch}$. The film length is L_f^* = 3.92 while Péclet number (Pe) and non-dimensional film width (W_f^*) are varied.

W_f^*	Pe				
	26.16	69.75	121.91	174.22	261.42
0.39	0.72	0.72	0.73	0.75	0.78
0.59	0.55	0.56	0.58	0.61	
0.78	0.45	0.46	0.50		
0.98	0.39	0.41			

Table 30: Minimum Sherwood number (Sh_{min}) in the film wake normalized with fully developed channel Sherwood number ($Sh_{FD,ch}$): $Sh_{ext}/Sh_{FD,ch}$. The film length is L_f^* = 9.80 while Péclet number (Pe) and non-dimensional film width (W_f^*) are varied.

W_f^*	Pe				
	26.16	69.75	121.91	174.22	261.42
0.39	0.70	0.68	0.68	0.69	0.71
0.59	0.56	0.55	0.56	0.58	
0.78	0.47	0.45	0.48		
0.98	0.39	0.40			

Results in Table 31 - Table 33 reveal that Pe, W_f^*, and L_f^* positively affect the convergence length (x_{conv}-x_f-L_f). All the tabulated convergence lengths show that films, regardless their lengths, affect a downstream distance much longer than the respective film length. This distance can be as long as 13.48 mm for a film with L_f^* = 9.80 when Pe and W_f^* were 174.22 and 0.59, respectively.

Table 31: Convergence length of Sherwood number with respect to film exit (x_{conv}-x_f-L_f) [mm] for a film length of L_f* = 1.96. Péclet (Pe) and non-dimensional film width (W_f*) are varied.

W_f*	Pe				
	26.16	69.75	121.91	174.22	261.42
0.39	1.93	3.85	5.52	6.67	7.25
0.59	2.45	5.20	8.08	9.55	
0.78	2.83	6.54	9.62		
0.98	3.28	7.44			

Table 32: Convergence length of Sherwood number with respect to film exit (x_{conv}-x_f-L_f) [mm] for a film length of L_f* = 3.92. Péclet (Pe) and non-dimensional film width (W_f*) are varied.

W_f*	Pe				
	26.16	69.75	121.91	174.22	261.42
0.39	2.02	4.33	6.44	8.17	9.70
0.59	2.53	5.61	8.87	11.37	
0.78	2.98	6.82	10.73		
0.98	3.37	7.85			

Table 33: Convergence length of Sherwood number with respect to film exit (x_{conv}-x_f-L_f) [mm] for a film length of L_f* = 9.80. Péclet (Pe) and non-dimensional film width (W_f*) are varied.

W_f*	Pe				
	26.16	69.75	121.91	174.22	261.42
0.39	2.06	4.86	7.74	10.29	13.61
0.59	2.57	6.14	9.97	13.48	
0.78	3.08	7.29	11.95		
0.98	3.46	8.31			

5.1.3.3. Effect of interfacial coverage on Sh

For simplified PEMFC performance models incorporating the effects of films, the use of Sh_{eff} instead of Sh is important to account for the loss of interfacial area. A typical difference between Sh and Sh_{eff} is presented in Figure 42 for the case of Pe = 69.75, W_f* = 0.78 (W_f = 0.40 mm), and L_f* = 9.80 (L_f = 5.00 mm). The film is positioned at x_f = 5.00 mm and extends to x_f+L_f = 10.00 mm. Sh and Sh_{eff} begin to differentiate at x = 4.60 mm and remerge at x = 10.40 mm. The difference between Sh and Sh_{eff} profiles is Sh_{eff} = Sh×0.69. This 31% difference stems from the film width of W_f = 0.40 mm. Sh peaks at the entrance of the film to 4.91 which is significantly higher than $Sh_{FD,f}$. This peak gradually tapers off to 2.50 within the film. The change of Sh throughout the length of the film corresponds to 51%. This change is larger than the one caused

by interfacial area loss. Therefore, local variations of Sh and interfacial area loss should be integrated into Sh_{eff} for a better prediction of PEMFC performance.

The interfacial area loss due to water film coverage is also useful to understand the Sh trend in the film wake. In the aforementioned region of the channel, there is no interfacial area coverage by the film. The discontinuity of Sh at the film exit can be explained by a Sh_{eff} plot. Sh_{eff} plot shows almost no discontinuity at the film exit contrary to Sh plot. This means that the flow exiting the film cannot expand along the width of the channel fast enough. Although, there is no interfacial coverage in the film wake, the effective O_2 transport towards one of the corners of the channel is still almost zero.

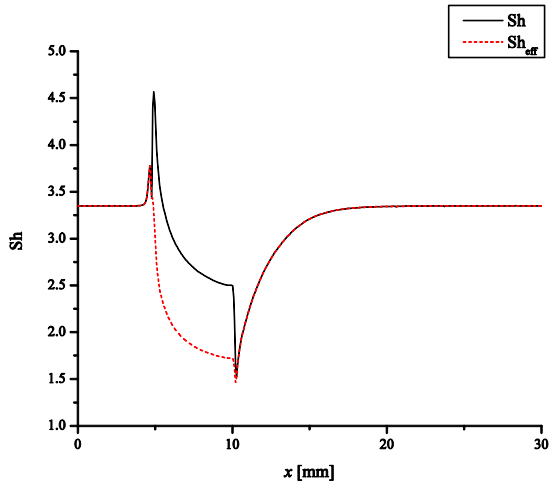

Figure 42: The comparison between dry-region-averaged (Sh) and effective (Sh_{eff}) Sherwood numbers for a film at x_f = 5.00 mm. Conditions are Pe = 69.75, W_f* = 0.78 (W_f = 0.40 mm), and L_f* = 9.80 (L_f = 5.00 mm).

5.1.3.4. Typical multiple-film results

Multiple-film results can resemble single-film ones as the uniform film spacing (Δx_f) becomes large enough or the set of Pe-W_f* values becomes small enough. In multiple-film simulations, the non-dimensional uniform film spacing (Δx_f*) took values of 1.96, 3.92, and 9.80 (corresponding to dimensional values of Δx_f = 1.00, 2.00, and 5.00 mm).

Figure 43 depicts a typical profile of Sh for the condition of $W_f^* = 0.39$, $L_f^* = 9.80$ ($L_f = 5.00$ mm), and $\Delta x_f^* = 9.80$ ($\Delta x_f = 5.00$ mm). A single-film condition is presented for Pe = 26.16. In the family of plots for multiple-films, Pe varied from 26.16 to 174.22. The results show that at the lowest Pe value, the multiple-film result matches the single-film one. However, with the increase of Pe, Sh profiles do not resemble low Pe ones. Therefore, multiple-film Sh profiles diverge from single-film ones at high Pe vales.

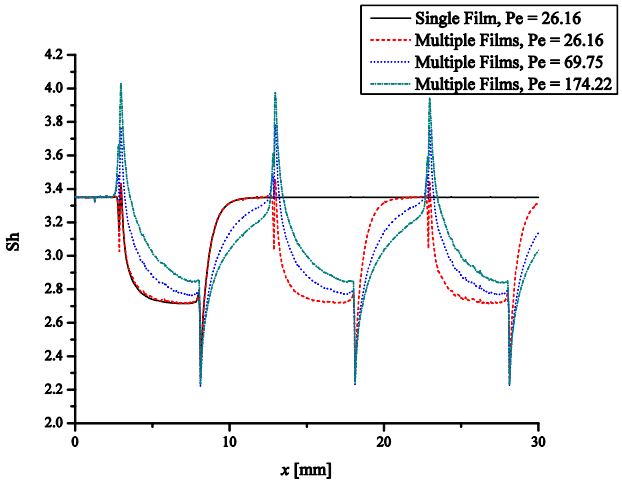

Figure 43: Sh results for a single-film scenario and multiple-film scenarios. All results have the condition of $W_f^* = 0.39$, $L_f^* = 9.80$ ($L_f = 5.00$ mm), and $\Delta x_f^* = 9.80$ ($\Delta x_f = 5.00$ mm). The first film is positioned at $x_{f,1} = 5.00$ mm.

5.1.3.5. Estimation of the effect of the Sherwood number variations on cell performance

Variations of Sh_{eff} in air channel due to the presence of films lead to changes in local performance in a fuel cell. The change in performance can be expressed with a change in voltage for a given current density (i). Calculations of performance loss in PEMFC were borrowed from Section 5.1.1.5.

As a baseline reference, the value of $Sh_{FD,ch} = 3.349$ causes a voltage loss of 9.0 mV at $i = 1.5$ A cm^{-2} relative to the condition of no interfacial transport resistance ($C_{int} \rightarrow C_m$). A film with the configuration of $W_f^* = 0.98$ ($W_f = 0.50$ mm) and $L_f^* = 9.80$ ($L_f = 5.00$ mm) was selected along

with the superficial air velocity corresponding to Pe = 69.75. The resulting critical points in the flow direction are $Sh_{max} = 2.19 \times Sh_{FD,f} = 2.19 \times 2.32 = 5.08$, $Sh_{ext} = 1.11 \times Sh_{FD,f} = 1.11 \times 2.32 = 2.58$, $Sh_{min} = 0.40 \times Sh_{FD,ch} = 0.40 \times 3.35 = 1.34$. Effective Sh is calculated as: $Sh_{max,eff} = Sh_{max} \times 0.61 = 3.10$ and $Sh_{ext,eff} = Sh_{ext} \times 0.61 = 1.57$. At the aforementioned i, the additional voltage drops at the positions x_{max}, x_{ext}, and x_{min} are 1, 15, and 22 mV, respectively. These values show that there is a significant voltage drop within the 5.00 mm long film. Moreover, the voltage drop at the immediate wake of the film lasts approximately 8.31 mm. Hence, the effect of the voltage drop 22 mV lasts more than the film length itself.

A comparison can be made between the impact of interfacial blockage by films and variations of Sh on the side of films. In a scenario of $W_f = 0.50$ mm and $i = 1.5$ A cm^{-2}, which is the largest film width in this study, the available interfacial width is $0.61W_{ch}$. A sufficiently long film has a $Sh_{FD,f}$ of 2.32 which is equivalent to $0.69Sh_{FD,ch}$. If Sh is assumed to be $Sh_{FD,ch}$ on the side of a film and only the interfacial blockage is considered, Sh_{eff} of $0.61Sh_{ch,FD}$ leads to a voltage drop 8 mV. If the interfacial blockage is neglected and only the variation of Sh is considered, Sh_{eff} of $0.69Sh_{FD,ch}$ leads to a voltage drop of 5 mV. Due to the logarithmic dependence of voltage loss on the transport resistance, the combination of the aforementioned resistances is significantly detrimental. A Sh_{eff} of $0.61Sh_{FD,f} = 0.61 \times 0.69Sh_{FD,ch} = 0.42Sh_{FD,ch}$ leads to a voltage loss of 20 mV.

5.2. SHERWOOD NUMBER CORRELATIONS

5.2.1. Droplet Correlations

5.2.1.1. Correlations for the maximum Sherwood number in the wake of a single droplet

The maximum Sherwood number in the wake of a single droplet ($Sh_{1,max}$) is correlated with the equations below with a maximum deviation of 0.657%. Values of $Sh_{1,max}$ corresponding to r^*

= 0.39 exceeded the aforementioned maximum error due to reasons explained in Section 5.1.1.4.1.

$$\mathrm{Sh}_{1,\max}(\mathrm{Pe}, r^*) = f(r^*) + g(r^*)\mathrm{Pe} \tag{31}$$

$$f(r^*) = -437.02{r^*}^2 + 43.075r^* + 2.2657 \tag{32}$$

$$g(r^*) = -2.72 \times 10^4 {r^*}^3 + 7.19 \times 10^3 {r^*}^2 - 5.23r^* + 11.712 \tag{33}$$

5.2.1.2. Correlations for the down-the-channel averaged Sherwood number

For each spacing between two consecutive droplets (n^{th} and n+1st), $\mathrm{Sh}_{av,n}$ can be predicted through the use of correlations in this section. The input variables are Pe, r^*, and Δx_d^*. Based on the number of simulated droplets, $\mathrm{Sh}_{av,n}$ can be predicted with a maximum error of 11% at 999 data points corresponding to the interfacial area left in between two droplets.

As it was seen in Figure 30 and Figure 31b, Sh_{av} starts with an initial value ($\mathrm{Sh}_{av,1}$) and converges to an asymptotic value in between the last two droplets ($\mathrm{Sh}_{av,\infty}$) with a variable convergence rate (α). Eq. (34) expresses the down the channel variation of $\mathrm{Sh}_{av,n}$. The three parameters that constitute the Eq. (34) were correlated separately to the input parameters.

$$\mathrm{Sh}_{av,\boldsymbol{n}} = \mathrm{Sh}_{av,1} + \left(\mathrm{Sh}_{av,\infty} - \mathrm{Sh}_{av,1}\right)\left(1 - e^{-(n-1)/\alpha}\right) \tag{34}$$

The values of $\mathrm{Sh}_{av,1}$ are correlated separately at Pe $\leq$ 34.88 and Pe $\geq$ 121.91. However, extrapolating the use these correlations respectively up to Pe $\leq$ 52.32 and Pe $\geq$ 69.75 is also possible while remaining within 11% error. For the remaining range of Pe (52.32 < Pe < 69.75), $\mathrm{Sh}_{av,1}$ can be assumed to be Sh_{FD}. The errors still remain below 11%. Irrespective of the Pe value,

$Sh_{av,1}$ correlations behave quadratically with r^* as shown in Eq. (35). Coefficients of Eq. (35) are defined in Eq. (36) as a function of the matrix, **M** and Δx_d^*. Eq. (36) reveals that $Sh_{av,1}$ decreases with Δx_d^* in the entire Pe range.

$$Sh_{av,1} = a_1 r^{*2} + b_1 r^* + c_1 \tag{35}$$

$$\begin{bmatrix} a_1 \\ b_1 \\ c_1 \end{bmatrix} = \mathbf{M} \begin{bmatrix} (\Delta x_d^*)^{-1} \\ 1 \end{bmatrix} \tag{36}$$

The matrix, **M** in Eq. (37) is a function of Pe and its dependency of Pe changes at different ranges of Pe. The correlations for **M** are given in Eq. (37) and operate at two ranges of Pe (Pe $\leq$ 52.32 and Pe $\geq$ 69.75).

$$\mathbf{M} = \begin{cases} \text{Pe} \leq 52.32 & \begin{bmatrix} 10.481 & \dfrac{\text{Pe}^{2.13}}{558.24} \\ 0.0565\text{Pe} - 8.6652 & -\dfrac{\text{Pe}^{2.094}}{1015.2} \\ -0.0119\text{Pe} + 0.8786 & \dfrac{\text{Pe}^{0.043}}{0.3313} \end{bmatrix} \\ \text{Pe} \geq 69.75 & \begin{bmatrix} 0.6877\text{Pe} + 28.471 & 0.9231\text{Pe} - 120.64 \\ -0.2235\text{Pe} - 17.431 & -0.3925\text{Pe} + 54.264 \\ 0.02\text{Pe} + 1.8361 & 0.0424\text{Pe} - 2.7638 \end{bmatrix} \end{cases} \tag{37}$$

Values of $Sh_{av,\infty}$ takes the same value with $Sh_{av,1}$ at the conditions of Pe $<$ 69.75 since $Sh_{av,\infty}$ and $Sh_{av,1}$ are very close to each other in this Pe range. For conditions of Pe $\geq$ 69.75, Eqs. (38) – (41) express $Sh_{av,\infty}$. Eq. (38) shows that $Sh_{av,\infty}$ increases linearly with r^*. The coefficients for Eq. (38) are dependent on the matrices **K** and **L**, and Δx_d^*. With the help of Eqs. (39) - (41), it can be stated that the coefficients a_2 and b_2 are quadratically dependent on Δx_d^* and Pe.

$$Sh_{av,\infty} = a_2 r^* + b_2 \tag{38}$$

$$\begin{bmatrix} a_2 \\ b_2 \end{bmatrix} = \begin{bmatrix} \mathbf{K} \\ \mathbf{L} \end{bmatrix} \begin{bmatrix} (\Delta x_d^*)^2 \\ (\Delta x_d^*) \\ 1 \end{bmatrix} \tag{39}$$

$$\mathbf{K}^T = \begin{bmatrix} -2.224 \times 10^{-4} & 5.371 \times 10^{-2} & -3.3943 \\ 2.732 \times 10^{-3} & -0.6604 & 40.5 \\ -3.792 \times 10^{-3} & 1.042 & -56.55 \end{bmatrix} \begin{bmatrix} \mathrm{Pe}^2 \\ \mathrm{Pe} \\ 1 \end{bmatrix} \tag{40}$$

$$\mathbf{L}^T = \begin{bmatrix} 4.333 \times 10^{-5} & -1.075 \times 10^{-2} & 0.7054 \\ -5.216 \times 10^{-4} & 0.1272 & -8.051 \\ 6.422 \times 10^{-4} & -0.162 & 11.67 \end{bmatrix} \begin{bmatrix} \mathrm{Pe}^2 \\ \mathrm{Pe} \\ 1 \end{bmatrix} \tag{41}$$

The parameter for the rate of $\mathrm{Sh}_{av,n}$ convergence (α) is expressed through Eqs. (42) -(44). The value of α is independent of Pe and decreases with r^* and Δx_d^*. For a given r^*, α becomes less dependent of the droplet spacing as the spacing increases.

$$\alpha = \alpha_{\max} - (\alpha_{\max} - \alpha_{\min}) \left(1 - e^{(1.96 - \Delta x_d^*)/1.8} \right) \tag{42}$$

$$\alpha_{\max} = 0.0735 r^{*-2.6} \tag{43}$$

$$\alpha_{\min} = 0.1708 r^{*-1.036} \tag{44}$$

5.2.2. Film Correlations

In this section, correlations of Sh are provided for the side of a film that remains exposed to air flow and the film wake. They are expressed non-dimensionally for increasing their applicability. The first step to correlate Sh_{eff} is to relate Sh_{eff} and Sh by using Eqs. (45) and (46). The conditional statement in Eq. (46) outputs a non-zero W_{wet} value when down-the-channel position corresponds to a film.

$$\mathrm{Sh}_{\mathrm{eff}}(x) = \mathrm{Sh}(x)[W_{\mathrm{ch}} - W_{\mathrm{wet}}(x)]W_{\mathrm{ch}}^{-1} \tag{45}$$

$$W_{\mathrm{wet}}(x) = \begin{cases} \left(x_{\mathrm{f},n} \le x \le x_{\mathrm{f},n} + L_{\mathrm{f}}\right) \rightarrow W_{\mathrm{f}} \cos\left(\pi \frac{\theta_{\mathrm{st,GDL}} - 90^{\circ}}{180}\right) \\ \mathrm{Else} \rightarrow 0 \end{cases} \tag{46}$$

5.2.2.1. Correlations of Sh on the side of a film

Eq. (47) provides the correlation for $\mathrm{Sh}_{\mathrm{FD,f}}$. Local Sh on the side of a film is expressed with respect to $\mathrm{Sh}_{\mathrm{FD,f}}$ in Eq. (15). The variation of $\mathrm{Sh}/\mathrm{Sh}_{\mathrm{FD,f}}$ along the flow length resembles the Graetz problem. This resemblance allows a logarithmic correlation between the non-dimensional distance along the film ($x_{\mathrm{f},n}$*) and the value of $\mathrm{Sh}/\mathrm{Sh}_{\mathrm{FD,f}}$.

$$\mathrm{Sh}_{\mathrm{FD,f}} = 1.5234 {W_{\mathrm{f}}^{*}}^{2} - 2.7649 W_{\mathrm{f}}^{*} + 3.5643 \tag{47}$$

Eq. (48) utilizes $x_{\mathrm{f},n}$* that is measured along the length of a film ($x_{\mathrm{f},n} < x < x_{\mathrm{f},n}+L_{\mathrm{f}}$). The definition of $x_{\mathrm{f},n}$* is provided in Eq. (49). The coefficients a_1 and b_1 are expressed in Eq. (50). The use of Eq. (48) within the film region leads to a $\mathrm{Sh}/\mathrm{Sh}_{\mathrm{FD,f}}$ value that is larger than unity at the film entrance. As $x_{\mathrm{f},n}$* grows in the flow direction, there is a value of $x_{\mathrm{f},n}$* at which $\mathrm{Sh}/\mathrm{Sh}_{\mathrm{FD,f}}$ reaches to unity. For any value of $\mathrm{x}_{\mathrm{f},n}$* further downstream, Eq. (48) should continue outputting unity. In order to ensure that the logarithmic function does not output any value lower than unity, Eq. (48) is written as a conditional statement.

$$\frac{\mathrm{Sh}}{\mathrm{Sh}_{\mathrm{FD,f}}} = \begin{cases} \left\{\left[a_1 \log_{10}\left(x_{\mathrm{f},n}^{*}\right) + b_1\right] \le 1\right\} \rightarrow a_1 \log_{10}\left(x_{\mathrm{f},n}^{*}\right) + b_1 \\ \left\{\left[a_1 \log_{10}\left(x_{\mathrm{f},n}^{*}\right) + b_1\right] \ge 1\right\} \rightarrow 1 \end{cases} \tag{48}$$

The non-dimensional distance, $x_{f,n}$* is a function of film number (n) in the flow direction (in case of multiple films), uniform film spacing (Δx_f) and length (L_f). The dimensional distance by a film is non-dimensionalized with d_h and Pe.

$$x_{f,n}^* = \left[x - x_{f,1} - (n-1)(\Delta x_f + L_f)\right] d_h^{-1} \mathrm{Pe}^{-1} \tag{49}$$

$$\begin{bmatrix} a_1 \\ b_1 \end{bmatrix} = \begin{bmatrix} a_2 & b_2 \\ a_3 & b_3 \end{bmatrix} \begin{bmatrix} \mathrm{Pe} \\ 1 \end{bmatrix} \tag{50}$$

$$\begin{bmatrix} a_2 \\ b_2 \end{bmatrix} = \begin{bmatrix} -0.0031 & 0.0005 \\ -0.2175 & -0.0528 \end{bmatrix} \begin{bmatrix} W_f^* \\ 1 \end{bmatrix} \tag{51}$$

$$\begin{bmatrix} a_3 \\ b_3 \end{bmatrix} = \begin{bmatrix} 0.004 & -0.0072 & 0.0016 \\ 0.1187 & -0.2031 & 0.9438 \end{bmatrix} \begin{bmatrix} W_f^{*2} \\ W_f^* \\ 1 \end{bmatrix} \tag{52}$$

5.2.2.2. Correlations of Sh in the film wake

Similarly to the previous section, Sh trends in the film wake resembles the Graetz problem. Local Sh is normalized with $\mathrm{Sh}_{FD,ch}$ and then correlated to non-dimensionional distance measured from the start of the film end ($x_{w,n}$*). The logarithmic correlation between $\mathrm{Sh}/\mathrm{Sh}_{FD,ch}$ and $x_{w,n}$* is presented in Eq. (53). The definition of $x_{w,n}$* is provided in Eq. (54).

$$\frac{\mathrm{Sh}}{\mathrm{Sh}_{FD,ch}} = \begin{cases} \left\{\left[a_1 \log_{10}\left(x_{w,n}^*\right) + b_1\right] \le 1\right\} \rightarrow a_1 \log_{10}\left(x_{w,n}^*\right) + b_1 \\ \left\{\left[a_1 \log_{10}\left(x_{w,n}^*\right) + b_1\right] \ge 1\right\} \rightarrow 1 \end{cases} \tag{53}$$

$$x_{w,n}^* = \left[x - x_{f,1} - nL_f - (n-1)\Delta x_f\right] d_h^{-1} \mathrm{Pe}^{-1} \tag{54}$$

The correlations for a_2, a_3, b_2, and b_3 are available for two different ranges of Pe, namely Pe ≤ 69.75 and Pe ≥ 69.75. The aforementioned correlations for Pe ≤ 69.75 are presented in Eqs. (55) – (59). For the range of Pe > 69.75, Eqs. (60) - (65) can be used for the aforementioned coefficients.

$$\begin{bmatrix} a_2 \\ b_2 \end{bmatrix} = \begin{bmatrix} -0.0096a_4 & 0.0009b_4 \\ 0.8926a_5 & -0.0393b_5 \end{bmatrix} \begin{bmatrix} W_{\mathrm{f}}^* \\ 1 \end{bmatrix} \tag{55}$$

$$\begin{bmatrix} a_4 \\ b_4 \\ a_5 \\ b_5 \end{bmatrix} = \begin{bmatrix} 0.7083 + (5.955 - 0.7083)\exp(-1.13L_{\mathrm{f}}^*) \\ 0.8889 + (81.89 - 0.8889)\exp(-1.682L_{\mathrm{f}}^*) \\ 0.865 + (6.033 - 0.865)\exp(-1.345L_{\mathrm{f}}^*) \\ -1.677 + (66.05 + 1.677)\exp(-1.37L_{\mathrm{f}}^*) \end{bmatrix} \tag{56}$$

$$\begin{bmatrix} a_3 \\ b_3 \end{bmatrix} = \begin{bmatrix} 0.0163a_6 & -0.0282b_6 & 0.0071c_6 \\ -0.9007a_7 & 1.7209b_7 & 0.732c_7 \end{bmatrix} \begin{bmatrix} W_{\mathrm{f}}^{*2} \\ W_{\mathrm{f}}^* \\ 1 \end{bmatrix} \tag{57}$$

$$\begin{bmatrix} a_6 \\ b_6 \\ c_6 \end{bmatrix} = \begin{bmatrix} 0.0274 & -0.338 & 1.0138 \\ 0.0216 & -0.2722 & 1.0193 \\ 0.0222 & -0.2837 & 1.0259 \end{bmatrix} \begin{bmatrix} L_{\mathrm{f}}^{*2} \\ L_{\mathrm{f}}^* \\ 1 \end{bmatrix} \tag{58}$$

$$\begin{bmatrix} a_7 \\ b_7 \\ c_7 \end{bmatrix} = \begin{bmatrix} 0.0145 & -0.1445 & 1.0089 \\ 0.0103 & -0.1138 & 1.0288 \\ -0.0084 & 0.0994 & 0.9771 \end{bmatrix} \begin{bmatrix} L_{\mathrm{f}}^{*2} \\ L_{\mathrm{f}}^* \\ 1 \end{bmatrix} \tag{59}$$

$$\begin{bmatrix} a_2 \\ b_2 \end{bmatrix} = \begin{bmatrix} 0.0099a_4 & -0.0086b_4 & 0.0014c_4 \\ -0.701a_5 & 1.1288b_5 & -0.211c_5 \end{bmatrix} \begin{bmatrix} W_{\mathrm{f}}^{*2} \\ W_{\mathrm{f}}^* \\ 1 \end{bmatrix} \tag{60}$$

$$\begin{bmatrix} a_4 \\ b_4 \\ c_4 \end{bmatrix} = \begin{bmatrix} 0.0523 & -0.7199 & 1.9882 \\ 0.056 & -0.762 & 2.2791 \\ 0.0805 & -1.0929 & 3.1905 \end{bmatrix} \begin{bmatrix} L_{\mathrm{f}}^{*2} \\ L_{\mathrm{f}}^* \\ 1 \end{bmatrix} \tag{61}$$

$$\begin{bmatrix} a_5 \\ b_5 \\ c_5 \end{bmatrix} = \begin{bmatrix} 0.0547 & -0.7215 & 2.3618 \\ 0.0243 & -0.3001 & 1.5204 \\ 0.0262 & -0.3078 & 0.985 \end{bmatrix} \begin{bmatrix} L_{\mathrm{f}}^{*2} \\ L_{\mathrm{f}}^* \\ 1 \end{bmatrix} \tag{62}$$

$$\begin{bmatrix} a_3 \\ b_3 \end{bmatrix} = \begin{bmatrix} 0.0241a_6 & -0.0165b_6 & 0.0023c_6 \\ -1.6684a_7 & 1.6517b_7 & 0.7465c_7 \end{bmatrix} \begin{bmatrix} W_{\mathrm{f}}^{*2} \\ W_{\mathrm{f}}^* \\ 1 \end{bmatrix} \tag{63}$$

$$\begin{bmatrix} a_6 \\ b_6 \\ c_6 \end{bmatrix} = \begin{bmatrix} 0.0022 & -0.0471 & 0.3451 \\ 0.0058 & -0.0835 & 0.4747 \\ 0.0302 & -0.3991 & 1.3623 \end{bmatrix} \begin{bmatrix} L_{\mathrm{f}}^{*2} \\ L_{\mathrm{f}}^* \\ 1 \end{bmatrix} \tag{64}$$

$$\begin{bmatrix} a_7 \\ b_7 \\ c_7 \end{bmatrix} = \begin{bmatrix} -0.0169 & 0.2154 & -0.1135 \\ -0.0175 & 0.2492 & -0.207 \\ 0.0022 & -0.0484 & 1.5556 \end{bmatrix} \begin{bmatrix} L_{\mathrm{f}}^{*2} \\ L_{\mathrm{f}}^* \\ 1 \end{bmatrix} \tag{65}$$

5.2.2.3. Accuracy of single-film correlations

Figure 44 presents a representative comparison between the numerically generated Sh and correlation-predicted Sh (Sh_{cor}) at the film wake. This film has the following configuration: Pe = 26.16, W_f* = 0.39, and L_f* = 9.80. Figure 44a shows the superposition of Sh and Sh_{cor} plotted against the logarithm of non-dimensionalized distance in the film wake (x_w*) as defined in Eq. (54). As Figure 44a depicts, there is a very good agreement with the numerical data and the prediction. A quantification of the prediction accuracy is presented in Figure 44b. This figure presents the ratio of Sh_{cor}/Sh. It can be noted that the maximum error for the prediction is 10%.

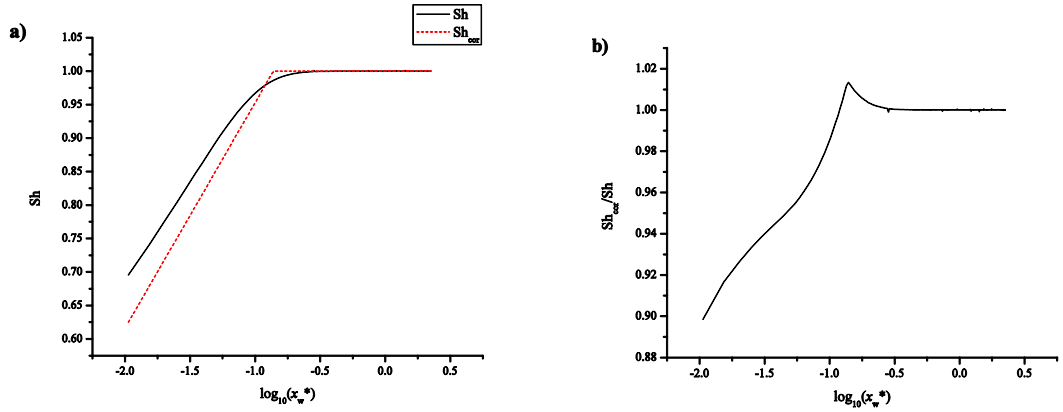

Figure 44: Comparison of numerically generated Sherwood number (Sh) and predicted Sh through correlations (Sh_{cor}) along the non-dimensional distance measured in the film wake (x_w*). a) Superimposition of Sh and Sh_{cor}, b) Ratio of Sh_{cor}/Sh.

5.2.2.4. Application example for the Sh correlations

The correlations of Sh_{eff} provided by this study can be applied to air channels with a characterized film distribution and air velocity. This section utilizes an image from an ex-situ visualization setup that was described in detail by Banerjee and Kandlikar [26]. This setup creates the two-phase flow conditions in a flow field with parallel channels by injecting liquid water through a GDL and into channels. The image in Figure 45 shows two films at $x_{f,1}$ = 5.00 mm and $x_{f,2}$ = 10.00 mm. Although the film sizes and channel width are shown to the scale, the section in

between two films was removed to superimpose the images with the plot. This image was taken at 0.4 A cm^{-2} current density, 23 °C and 0% relative humidity. These conditions correspond to a Pe of 48.62. Film widths are $W_{f,1}$ = 0.40 mm and $W_{f,2}$ = 0.50 mm.

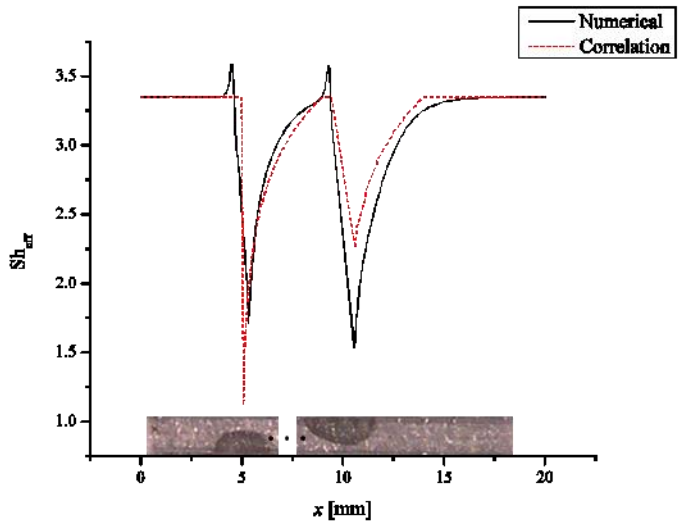

Figure 45: The comparison of Sh_{eff} obtained through numerical simulations and correlations. The comparison is made for a configuration of two films that 5.00 mm apart. Their widths are $W_{f,1}$ = 0.40 mm and $W_{f,2}$ = 0.50 mm.

Sh_{eff} profiles for the visualized film configuration were obtained through a numerical simulation and correlations. The correlations were input a constant film width of W_f = 0.45 mm to represent the width of both films. The comparison of the plots revealed an agreement in the wake of films. Since the films have zero length, the flow conditions are the most difficult to predict on the side of the films. On regions that are at least a film width away from a film, the error percentages are below 20%.

5.3. EXPANDING THE USE OF SHERWOOD NUMBER CORRELATIONS

5.3.1. Applicability of Droplet Results to Different Length Scales and Air Properties

As introduced earlier in Section 5.1.1. , Sherwood number is a function of Pe, r^*, Δx_d^*, and Sc. The present study provides Sh correlations for the first three parameters. In order to showcase the applicability of these correlations to different length scales, two simulations were performed. Both of them had the same Pe, r^*, Δx_d^*, and Sc that correspond to 174.22, 0.29, 3.92, and 0.633 respectively. One of the simulations had dimensions that were scaled-up by a factor of 2 based on the dimensions of the other simulation. Hence, these simulations can be differentiated with their hydraulic diameters: d_h = 0.51 and 1.02 mm. In order to keep the non-dimensional parameters of r^* and Δx_d^* the same, r and Δx_d were changed proportional to d_h. Contrarily, u_m was changed inversely proportional to d_h to keep Pe the same.

Figure 46 shows local Sh results at different length scales d_h = 0.51 and 1.02 mm with the same non-dimensional parameters (Pe, r^*, and Δx_d) that was specified in the paragraph above. Since two simulations had two different channel lengths, down the channel position (x) was non-dimensionalized with the respective value of d_h. This plot depicts the same case presented in Section 4.3.4.1. for mesh independency study. The non-dimensional position x/d_h = 21.56 refers to the position of the fifth droplet. The close-up view in Figure 46 is shown with the intent of showing how well two results match. This plot proves that the non-dimensionalization was performed correctly since results match at the same non-dimensional parameters despite different length scales.

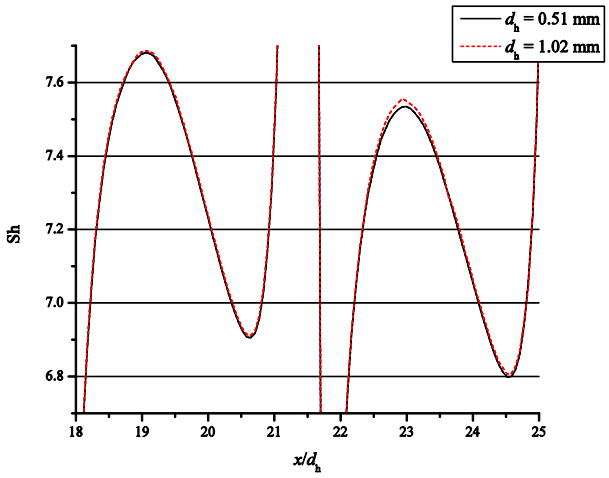

Figure 46: The applicability of Sherwood number (Sh) correlations at different length scales. The Péclet number (Pe), non-dimensional droplet radius (r^*) and uniform spacing (Δx_d^*) are 174.22, 0.29, and 3.92, respectively. Results of Sh exactly match at different hydraulic diameters (d_h) since non-dimensional variables are the same.

The parametric investigation of Sh dependence on Sc is kept out of the scope of this work. In order to provide a rough estimate for the Sh-Sc dependency, two simulations were performed. Both simulations had the conditions of Pe = 139.13, r^* = 0.29, and Δx_d^* = 3.92. However, they had different Sc values of 0.633 and 0.722. The former value corresponds to conditions that all other simulations in this work had (fully humidified air at 80 °C). The latter value corresponds to fully humidified conditions at 50 °C. The aforementioned conditions led to similar $Sh_{av,n}$ profiles with 7% difference. Further studies can map the effect Sc at different values of Pe, r^*, and Δx_d^*.

5.3.2. Applicability of Single-Film Correlations to Multiple Films and Different Air Properties

The correlations presented in Section 5.2.2. were built using the single-film simulation results. The applicability of these correlations to multiple-film scenarios is important for simplified PEMFC performance models to account for realistic conditions. This section will present the characterization of single-film correlations for their applicability to multiple-film scenarios.

Single-film Sh correlations were characterized for their applicability to multiple-film predictions. Figure 47 presents the ratio of Sh_{cor} to Sh. This ratio represents the prediction accuracy and was plotted for 3 consecutive films. The results were plotted starting from the first film (x-$x_{f,1}$). The films are 5.00 mm long and separated from each other for a film length. Hence, the first 5.00 mm of the plot corresponds to the film region while the following 5.00 mm corresponds to the wake region. This pattern continues for the next two films. The plot includes 21 conditions as a result of different permutations of Pe and W_f* as shown in Table 11. The results indicate that the largest error values can be seen in the beginning of a film and at the film wake. However, all error values are within 20%.

All multiple-film simulation results were used to characterize the accuracy of the correlations built with single-film results. Similar results were obtained to those shown in Figure 47. These results were first transformed into absolute error percentage values ($100\times|1\text{-}Sh_{cor}/Sh|$) and then averaged through the flow direction for all multiple-film simulations. The resulting value is called mean absolute percentage error (MAPE) as formally defined in Eq. (66). Each down the channel location is referred to with the variable, x_t in the discrete numerical solution. For an entire number of data points, k; the data is averaged.

$$\mathrm{MAPE} = 100\frac{1}{k}\sum_{t=1}^{k}\left|\frac{\mathrm{Sh_{cor}}(x_t) - \mathrm{Sh_{num}}(x_t)}{\mathrm{Sh_{num}}(x_t)}\right| \tag{66}$$

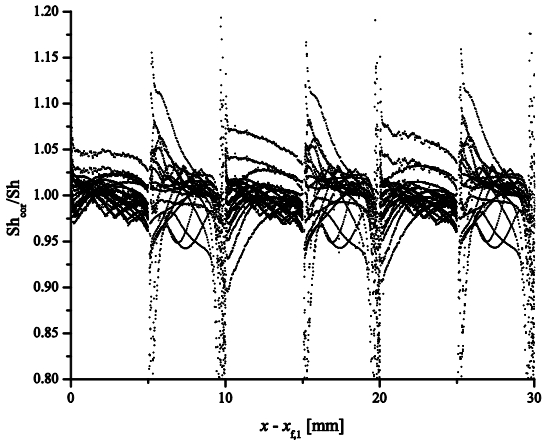

Figure 47: The ratio of correlation-predicted Sherwood number (Sh_{cor}) to numerically generated Sherwood number (Sh): Sh_{cor}/Sh. The ratio is plotted against the distance measured from the first film in the domain (x-$x_{f,1}$). At the same position different data points are presented for various Pe and W_f* conditions. L_f* and Δx_f* are 9.80 (5.00 mm).

The total number of cases is 252. These cases can be categorized into two groups based on Pe. For the range of Pe $\leq$ 52.32, there are 192 cases. MAPE for these cases is 9%. Among the data points of error, 83% and 5% of them are in between 0-10% and 10-20%, respectively. As a more challenging range of Pe, Pe > 52.32 covers 60 cases. In this range, MAPE is 9% as in the lower range of Pe. However, distribution of error differs by 80% and 8% of the data having an error range of 0-10% and 10-20%, respectively. Under the light of the aforementioned error characterization, the single-film based correlations can be applied to multiple-film cases with accuracy.

Although developed by using results obtained at 80 °C and 100% relative humidity, the applicability of the correlations was tested and found to be accurate down to 20 °C and 0% relative humidity. The effect of Sc on Sh at constant values of Pe = 121.62, W_f* = 0.79, and L_f* = 9.82 was numerically simulated. Since the effect of Δx_f can be neglected based on the results above, the effect of Sc was tested for a single film that results strong flow disruptions. Values of Sc for fully humidified air at temperatures of 20 and 80 °C are 0.753 and 0.632, respectively. Sc increases negligibly at temperatures lower than 20 °C since there is already a 2% increase from

40 to 20 °C. Hence, the lowest temperature to test the applicability of the correlations was selected to be 20 °C. Comparison of local Sh at 20 and 80 °C resulted in a maximum discrepancy of 3%. Variation of relative humidity from 0 to 100% has a negligible effect on Sc. The mixture of fully humidified air at 20 °C has a vapor molar fraction of 0.02. The subtraction of this marginal component to obtain dry air does not lead to a significant difference in Sc. Therefore, the reported simulation result for the effect of Sc is also applicable to dry air at 20 °C.

CHAPTER 6. CONLUSIONS AND FUTURE WORK

6.1. Conclusions

6.1.1. Addressing the Needs in the Available Literature

This study investigated the interfacial mass transport resistance at the GDL-air channel interface of a PEMFC. This resistance is used to predict the performance of a PEMFC through modeling efforts. With more accurate modeling, commercialization of PEMFCs can be faster and hence, cheaper PEMFCs can stand as a stronger contender against the contemporary internal combustion engines. Mass transport resistance can be expressed as the concentration drop of the species in interest. The oxygen concentration loss on the cathode side of PEMFCs is a major concern. In particular, the effect of two-phase flow in the air channel on the interfacial oxygen concentration drop remains as a question unanswered in the available literature. This concentration drop can be expressed through the non-dimensional Sherwood number (Sh) which is the reciprocally related to the concentration drop.

6.1.2. Approach

In order to investigate Sh, steady-state and 3D numerical simulations were conducted with a commercially available software package, COMSOL Multiphysics®. Simulations focused on an isolated air channel with water features (droplets and films) inside represented with solid obstructions. On the GDL-air channel interface O_2 is consumed and water features emerge. Governing equations for air flow and O_2 transport were solved. With the use of the resulting velocity and O_2 concentration profiles in the channel, Sh was calculated. In the fully developed region of the channel Sh ($Sh_{FD,ch}$) was calculated to be 3.349 for a channel cross section of 0.70 mm × 0.40 mm. Conclusions from this work are organized in major (Section 6.1.3.) and specific ones (Sections 6.1.4. and 6.1.5.).

6.1.3. Major Conclusions

- Characterization of Sh is provided to General Motors in form of mathematical correlations to be incorporated into their simplified PEMFC performance model. This model was earlier established with an assumption of dry air flow in cathode channels. With the correlations provided in this study, the aforementioned model will be operating by taking two-phase flow in account to calculate interfacial oxygen transport resistance.
- In modeling the performance of a PEMFC, inclusion of interfacial O_2 transport resistance was predicted to decrease the calculated voltage by 9.0 mV at a cell current density of 1.5 A cm^{-2}. Hence, it was shown that PEMFC performance models should include interfacial O_2 transport resistance through an accurate value of Sh.
- The variables that affect the results were non-dimensionalized to obtain an understanding of the physics which is applicable to different length scales and PEMFC operating conditions. The dimensional variables can be listed as air properties (density and viscosity), O_2 diffusivity in the air, superficial air velocity in the channel, droplet radius, film width/length, uniform spacing between droplets/films. Air properties and O_2 diffusivity were together expressed through Schmidt number (Sc). Superficial air velocity was non-dimensionalized into Péclet number (Pe). The remaining geometrical variables were non-dimensionalized with channel hydraulic diameter and referred to as non-dimensional geometrical variables.
- The approach of isolating the air channel from the adjacent GDL was shown to be accurate. The following were compared to each other to justify this approach: a simulation with an isolated channel and another with a channel-GDL combined domain. There is no significant difference between the results of Sh. Hence the less computationally expensive method, isolated channel, was utilized throughout this study.

- A water feature adhesion analysis was performed to justify steady-state simulations. The adhesion force of a water feature was semi-empirically calculated based on the experimental data available in the literature. This force was compared against the drag force that was numerically calculated. Tables were created with the variables of Pe and non-dimensional water feature size. Sets of Pe and non-dimensional water feature size were marked with adhesion or detachment.
- Multiple droplets were shown to lead to significant increases in Sh with respect to $Sh_{FD,ch}$ at high Pe values.
- Films were shown to affect their wake regions similar to their lengths. These wake regions have always low Sh compared to $Sh_{FD,ch}$.
- It was found that Sh on the side of a film vary significantly throughout the film length.
- Results for Sh were expressed through non-dimensional correlations that are specific to an array of droplets or films. Since these correlations are using non-dimensional parameters, they can be used at different length scales.

6.1.4. Conclusions for Droplets

- An experimental study of droplet adhesion study was used from the available literature to validate the adhesion prediction technique. The study from the literature provided an experimental observation of a droplet detaching from a GDL surface when it is subject to an increasing superficial air velocity. This experimental study was numerically simulated and the adhesion prediction technique was applied. This technique predicted all the experimental data of adhesion/detachment correctly.
- Sh starts showing an increase in the droplet wake when Pe reaches the minimum value for a given non-dimensional droplet radius. The increase in Sh is intensified with Pe, non-dimensional droplet radius, and the number of droplets in a row.

- A correlation was provided to predict the maximum possible Sh downstream of a single droplet. The maximum possible increase of Sh was reported to be 21%.
- For multiple droplets, the Sherwood number in between two consecutive droplets was averaged along the flow direction and referred to as average Sherwood number (Sh_{av}). This value starts changing in the flow direction with the first droplet. As the change vanishes in the flow direction, Sh converges to the asymptotic Sherwood number ($Sh_{av,\infty}$).
- A critical range of Péclet number was found ($52.32 < Pe < 69.75$) to identify $Sh_{av,\infty}$ switching from being lower than $Sh_{FD,ch}$ to being higher.
- Sherwood number values do not change significantly (less than 11%) throughout droplets in a row when Péclet number is below about 69.
- A set of correlations were built to provide Sh_{av} between any two consecutive droplets as a subset of a multiple droplet array. The correlations are a function of droplet number, Péclet number, non-dimensional droplet size and uniform droplet spacing. The maximum error of these correlations among 999 data points is 11%.
- The maximum $Sh_{av,\infty}$ was obtained to be 7.438 at the Péclet number, non-dimensional droplet radius and uniform spacing of 174.22, 0.29, and 3.92, respectively. The minimum $Sh_{av,\infty}$ was obtained to be 2.925 at the Péclet number, non-dimensional droplet radius and uniform spacing of 13.16, 0.39, and 1.96, respectively.
- It was noted that the voltage can decrease by 1.6 mV due to the minimum Sh and relatively increase by 5.3 mV due to the maximum Sh as compared to a channel with no droplets.

6.1.5. Conclusions for Films

- Films were categorized into two: zero and non-zero length. Zero-length films represent droplets that emerge from channel corner and establish a bridge between the GDL and top channel wall. When zero-length films are elongated in the air flow direction, they

start resembling the films typically seen in PEMFC air channels. These called non-zero-length films.

- There is a fully developed Sh on the side of a film that is sufficiently long ($Sh_{FD,f}$) which varies between the following values 2.32-2.71 with the film width.
- Films reduce the area of GDL-air channel interface for O_2 transport. This reduction has been accounted for by introducing the effective Sh (Sh_{eff}). It is equivalent to local Sh value that is reduced proportionally to the interfacial water coverage.
- In the immediate wake of a film, there is a minimum observed in Sh (Sh_{min}) which can be as low as $0.39Sh_{FD,ch}$.
- In the wake of Sh_{min}, there is a convergence trend of Sh from Sh_{min} to $Sh_{FD,ch}$. This convergence extends over a length similar to the film length. The maximum length was 13.48 mm.
- It was found that Sh on the side of a film varies significantly throughout the film length. The maximum Sh (Sh_{max}) is found at the entrance of the film and can be as high as $2.25Sh_{FD,f}$. If the film is long enough for a given Pe, Sh at the exit is $Sh_{FD,f}$.
- Correlations were developed to predict the local Sh profile for the side of a film and its wake. These correlations can be applied multiple-films. The correlations were tested against 252 multiple-film configurations. Mean absolute percentage error for Sh prediction was 9%.
- The maximum interfacial channel width blockage (39%) and Sh reduction on the side of a film (31%) lead to a voltage loss of 8 and 5 mV, respectively at a current density of 1.5 A cm^{-2}. The combined transport resistance due to the aforementioned components is a voltage reduction of 20 mV. Hence, Sh number correlations in this study should be incorporated into simplified PEMFC models along with interfacial blockage by films.

6.2. Future Work

The problem that was discussed in this study was a function of Pe, non-dimensional water feature size and uniform spacing, and Sc. The value of Sc represents the air properties. This study showed limited results on the effect of Sc on Sh. For a wider range of Sc, results can be quantified. This will be done while Pe and non-dimensional geometrical variables remain the same. An important constraint is that Reynolds number calculated on the water features should remain in the same regime (creeping, laminar, steady, unsteady, etc.) as Sc varies. This will ensure that the effect of Sc will be investigated while being isolated from the flow regime.

This study focused on the specific fuel cell design that complied with the requirements of US DoE. Hence, the numerical simulations were conducted only in the aforementioned channel cross section. Since Sh correlations were obtained in the non-dimensional form, they can be applied to channels with different length scales. However, the aspect ratio of the channel in interest should match the aspect ratio that was used in this work. For this reason, a future study can be defined to conduct numerical simulations aimed to investigate the effect of channel aspect ratio on Sh results.

The prediction of water feature attachment/detachment was shown to be possible with a hybrid technique (simulations, empirical data, and theoretical calculations). This technique can be applied to other available experimental data for a better validation. If it can be better validated with a wider range of parameters, a correlation can be established for attachment/detachment conditions while using the inputs of channel cross section, water feature position and size, and superficial air velocity.

CHAPTER 7. REFERENCES

[1] J. M. Ogden, "Alternative fuels and prospects - Overview," in *Handbook of fuel cells: fundamentals, technology, and applications*, vol. 3, 6 vols., W. Vielstich, A. Lamm, and H. A. Gasteiger, Eds. Chichester, England ; New York: Wiley, 2003, pp. 3–24.

[2] J. S. Cannon, "China at the crossroads: Energy, transportation, and the 21st century," INFORM, Inc., 1998.

[3] "Top Hybrid Cars | Hybrid Cars," *HybridCars.com*. [Online]. Available: http://www.hybridcars.com/top-hybrid-cars-list/. [Accessed: 19-Sep-2013].

[4] M. A. Weiss, J. B. Heywood, E. M. Drake, A. Schafer, and F. F. AuYeung, "On the road in 2020: A life-cycle analysis of new automobile technologies," Massachusetts Institute of Technology, Cambridge, MA, MIT EL 00-003, 2000.

[5] M. Q. Wang, "GREET 1.5 - Transportation fuel-cycle model. Volume 1: Methodology, Development, Use, and Results," Center for Transportation Research, Energy Systems Divison, Argonne, IL, 1999.

[6] M. Wang, M. Mintz, M. Singh, K. Stork, and L. Johnson, "Assessment of PNGV fuels infrastructure. Phase 2 Report: Additional capital needs and fuel-cycle energy and emissions impacts," The Center for Transportation Research, Energy Systems Division, Argonne, IL, 1998.

[7] C. E. Thomas, B. James, F. J. Lomax, and I. J. Kuhn, "Integrated analysis of hydrogen passenger vehicle transportation pathways, draft final," US Department of Energy.

[8] J. M. Ogden, M. M. Steinbugler, and T. G. Kreutz, "A comparison of hydrogen, methanol and gasoline as fuels for fuel cell vehicles: implications for vehicle design and infrastructure development," *J. Power Sources*, vol. 79, no. 2, pp. 143–168, Jun. 1999.

[9] C. E. Thomas, B. D. James, F. D. Lomax Jr., and I. F. Kuhn Jr., "Societal impacts of fuel options for fuel cell vehicles," in *International Fall Fuels and Lubricants Meeting and Exposition, October 19, 1998 - October 22, 1998*, 1998.

[10] J. M. Ogden, "Solar Hydrogen," in *Renewable energy sources of electricty and fuels*, Washington, DC: Island Press, 1993, pp. 925–1009.

[11] E. D. Larson, E. Worrell, and J. S. Chen, "Clean fuels from municipal solid waste for fuel cell buses in metropolitan areas," *Resour. Conserv. Recycl.*, vol. 17, no. 4, pp. 273–298, 1996.

[12] Y. Wang, K. S. Chen, J. Mishler, S. C. Cho, and X. C. Adroher, "A review of polymer electrolyte membrane fuel cells: Technology, applications, and needs on fundamental research," *Appl. Energy*, vol. 88, no. 4, pp. 981–1007, 2011.

[13] M. M. Mench, *Fuel cell engines*. John Wiley & Sons, 2008.

[14] R. P. O'Hayre, S.-W. Cha, W. Colella, and F. B. Prinz, *Fuel cell fundamentals*. Hoboken, N.J: John Wiley & Sons, 2006.

[15] J. E. Steinbrenner, E. S. Lee, C. H. Hidrovo, J. K. Eaton, and K. E. Goodson, "Impact of channel geometry on two-phase flow in fuel cell microchannels," *J. Power Sources*, vol. 196, no. 11, pp. 5012–5020, Jun. 2011.

[16] K. Seidenberger, F. Wilhelm, J. Haußmann, H. Markötter, I. Manke, and J. Scholta, "Grand canonical Monte Carlo study on water agglomerations within a polymer electrolyte membrane fuel cell gas diffusion layer," *J. Power Sources*, Feb. 2013.

[17] A. Turhan, K. Heller, J. S. Brenizer, and M. M. Mench, "Quantification of liquid water accumulation and distribution in a polymer electrolyte fuel cell using neutron imaging," *J. Power Sources*, vol. 160, no. 2, pp. 1195–1203, Oct. 2006.

[18] Z. Lu, M. M. Daino, C. Rath, and S. G. Kandlikar, "Water management studies in PEM fuel cells, part III: Dynamic breakthrough and intermittent drainage characteristics from GDLs with and without MPLs," *Int. J. Hydrog. Energy*, vol. 35, no. 9, pp. 4222–4233, May 2010.

[19] J. Eller, T. Rosén, F. Marone, and M. Stampanoni, "Progress in in situ x-ray tomographic microscopy of liquid water in gas diffusion layers of PEFC," *J. Electrochem. Soc.*, vol. 158, no. 8, pp. B963–B970.
[20] D. Lee and J. Bae, "Visualization of flooding in a single cell and stacks by using a newly-designed transparent PEMFC," *Int. J. Hydrog. Energy*, vol. 37, no. 1, pp. 422–435, Jan. 2012.
[21] H. Masuda, A. Yamamoto, K. Sasaki, S. Lee, and K. Ito, "A visualization study on relationship between water-droplet behavior and cell voltage appeared in straight, parallel and serpentine channel pattern cells," *J. Power Sources*, vol. 196, no. 13, pp. 5377–5385, Jul. 2011.
[22] J. Dillet, O. Lottin, G. Maranzana, S. Didierjean, D. Conteau, and C. Bonnet, "Direct observation of the two-phase flow in the air channel of a proton exchange membrane fuel cell and of the effects of a clogging/unclogging sequence on the current density distribution," *J. Power Sources*, vol. 195, no. 9, pp. 2795–2799, May 2010.
[23] E. Kimball, T. Whitaker, Y. Kevrekidis, and J. B. Benziger, "Drops, Slugs and Flooding in PEM Fuel Cells," 2007, vol. 11, pp. 725–736.
[24] Z. Zhan, C. Wang, W. Fu, and M. Pan, "Visualization of water transport in a transparent PEMFC," *Int. J. Hydrog. Energy*, vol. 37, no. 1, pp. 1094–1105, Jan. 2012.
[25] J. M. Sergi and S. G. Kandlikar, "Quantification and characterization of water coverage in PEMFC gas channels using simultaneous anode and cathode visualization and image processing," *Int. J. Hydrog. Energy*, vol. 36, no. 19, pp. 12381–12392, Sep. 2011.
[26] R. Banerjee and S. G. Kandlikar, "Liquid water quantification in the cathode side gas channels of a proton exchange membrane fuel cell through two-phase flow visualization," *J. Power Sources*, vol. 247, pp. 9–19, Feb. 2014.
[27] I. S. Hussaini and C.-Y. Wang, "Visualization and quantification of cathode channel flooding in PEM fuel cells," *J. Power Sources*, vol. 187, no. 2, pp. 444–451, Feb. 2009.
[28] Z. Lu, S. G. Kandlikar, C. Rath, M. Grimm, W. Domigan, A. D. White, M. Hardbarger, J. P. Owejan, and T. A. Trabold, "Water management studies in PEM fuel cells, Part II: Ex situ investigation of flow maldistribution, pressure drop and two-phase flow pattern in gas channels," *Int. J. Hydrog. Energy*, vol. 34, no. 8, pp. 3445–3456, May 2009.
[29] Y. Ding, X. Bi, and D. P. Wilkinson, "3D simulations of the impact of two-phase flow on PEM fuel cell performance," *Chem. Eng. Sci.*, vol. 100, pp. 445–455, Aug. 2013.
[30] L. Chen, T. F. Cao, Z. H. Li, and Y. L. He, "Numerical investigation of liquid water distribution in the cathode side of proton exchange membrane fuel cell and its effects on cell performance," *Int. J. Hydrog. Energy*, vol. 37, no. 11, pp. 9155–9170, Jun. 2012.
[31] H. Ju and C.-Y. Wang, "Experimental Validation of a PEM Fuel Cell Model by Current Distribution Data," *J. Electrochem. Soc.*, vol. 151, no. 11, p. A1954, 2004.
[32] U. Pasaogullari and C. Y. Wang, "Two-phase modeling and flooding prediction of polymer electrolyte fuel cells," *J. Electrochem. Soc.*, vol. 152, no. 2, pp. A380–A390, 2005.
[33] Y. Wang and C.-Y. Wang, "A Nonisothermal, Two-Phase Model for Polymer Electrolyte Fuel Cells," *J. Electrochem. Soc.*, vol. 153, no. 6, p. A1193, 2006.
[34] H. Ju, G. Luo, and C.-Y. Wang, "Probing Liquid Water Saturation in Diffusion Media of Polymer Electrolyte Fuel Cells," *J. Electrochem. Soc.*, vol. 154, no. 2, p. B218, 2007.
[35] B. Dokkar, N. E. Settou, O. Imine, N. Saifi, B. Negrou, and Z. Nemouchi, "Simulation of species transport and water management in PEM fuel cells," *Int. J. Hydrog. Energy*, vol. 36, no. 6, pp. 4220–4227, Mar. 2011.
[36] V. Gurau, T. A. Zawodzinski, and J. A. Mann, "Two-Phase Transport in PEM Fuel Cell Cathodes," *J. Fuel Cell Sci. Technol.*, vol. 5, no. 2, p. 021009, 2008.
[37] P.-H. Chi, F.-B. Weng, A. Su, and S.-H. Chan, "Numerical Modeling of Proton Exchange Membrane Fuel Cell With Considering Thermal and Relative Humidity Effects on the Cell Performance," *J. Fuel Cell Sci. Technol.*, vol. 3, no. 3, p. 292, 2006.

[38] H. Ju, "Investigation of the effects of the anisotropy of gas-diffusion layers on heat and water transport in polymer electrolyte fuel cells," *J. Power Sources*, vol. 191, no. 2, pp. 259–268, Jun. 2009.
[39] S. Basu, C.-Y. Wang, and K. S. Chen, "Phase Change in a Polymer Electrolyte Fuel Cell," *J. Electrochem. Soc.*, vol. 156, no. 6, p. B748, 2009.
[40] G. He, Y. Yamazaki, and A. Abudula, "A three-dimensional analysis of the effect of anisotropic gas diffusion layer(GDL) thermal conductivity on the heat transfer and two-phase behavior in a proton exchange membrane fuel cell(PEMFC)," *J. Power Sources*, vol. 195, no. 6, pp. 1551–1560, Mar. 2010.
[41] X.-G. Yang, Q. Ye, and P. Cheng, "Matching of water and temperature fields in proton exchange membrane fuel cells with non-uniform distributions," *Int. J. Hydrog. Energy*, vol. 36, no. 19, pp. 12524–12537, Sep. 2011.
[42] C. Y. Wang and P. Cheng, "Multiphase Flow and Heat Transfer in Porous Media," *Adv. Heat Transf.*, vol. 30, pp. 93–182, 1997.
[43] V. Gurau and J. A. Mann, "A Critical Overview of Computational Fluid Dynamics Multiphase Models for Proton Exchange Membrane Fuel Cells," *SIAM J. Appl. Math.*, vol. 70, no. 2, pp. 410–454, Jan. 2009.
[44] W. Gu, D. R. Baker, Y. Liu, and H. A. Gast, "Proton exchange membrane fuel cell (PEMFC) down-the-channel performance model," in *Handbook of fuel cells: fundamentals, technology, and applications*, vol. 6, 6 vols., W. Vielstich, H. Yokokawa, and H. A. Gasteiger, Eds. John Wiley & Sons, 2009, pp. 631–657.
[45] U. Pasaogullari and C. Y. Wang, "Liquid Water Transport in Gas Diffusion Layer of Polymer Electrolyte Fuel Cells," *J. Electrochem. Soc.*, vol. 151, no. 3, pp. A399–A406, 2004.
[46] U. Pasaogullari, C.-Y. Wang, and K. S. Chen, "Two-Phase Transport in Polymer Electrolyte Fuel Cells with Bilayer Cathode Gas Diffusion Media," *J. Electrochem. Soc.*, vol. 152, no. 8, p. A1574, 2005.
[47] G.-S. Kim, P. C. Sui, A. A. Shah, and N. Djilali, "Reduced-dimensional models for straight-channel proton exchange membrane fuel cells," *J. Power Sources*, vol. 195, no. 10, pp. 3240–3249, May 2010.
[48] J. He, J. Ahn, and S.-Y. Choe, "Analysis and control of a fuel delivery system considering a two-phase anode model of the polymer electrolyte membrane fuel cell stack," *J. Power Sources*, vol. 196, no. 10, pp. 4655–4670, May 2011.
[49] I. S. Hussaini and C. Y. Wang, "Dynamic water management of polymer electrolyte membrane fuel cells using intermittent RH control," *J. Power Sources*, vol. 195, no. 12, pp. 3822–3829, Jun. 2010.
[50] H. Wu, X. Li, and P. Berg, "Numerical analysis of dynamic processes in fully humidified PEM fuel cells," *Int. J. Hydrog. Energy*, vol. 32, no. 12, pp. 2022–2031, Aug. 2007.
[51] H. Wu, P. Berg, and X. Li, "Non-isothermal transient modeling of water transport in PEM fuel cells," *J. Power Sources*, vol. 165, no. 1, pp. 232–243, Feb. 2007.
[52] A. Casalegno, F. Bresciani, G. Groppi, and R. Marchesi, "Flooding of the diffusion layer in a polymer electrolyte fuel cell: Experimental and modelling analysis," *J. Power Sources*, vol. 196, no. 24, pp. 10632–10639, Dec. 2011.
[53] R. M. Darling and S. Khateeb, "The influence of gas-diffusion layer properties on elevated temperature operation of polymer-electrolyte fuel cells," *J. Power Sources*, vol. 243, pp. 328–335, Dec. 2013.
[54] J. Park and K. Min, "A quasi-three-dimensional non-isothermal dynamic model of a high-temperature proton exchange membrane fuel cell," *J. Power Sources*, vol. 216, pp. 152–161, Oct. 2012.
[55] K. Tüber, D. Pócza, and C. Hebling, "Visualization of water buildup in the cathode of a transparent PEM fuel cell," *J. Power Sources*, vol. 124, no. 2, pp. 403–414, Nov. 2003.

[56] H. Liu, P. Li, and K. Wang, “Optimization of PEM fuel cell flow channel dimensions—Mathematic modeling analysis and experimental verification,” *Int. J. Hydrog. Energy*, vol. 38, no. 23, pp. 9835–9846, Aug. 2013.
[57] P. K. Das, X. Li, and Z.-S. Liu, “Analysis of liquid water transport in cathode catalyst layer of PEM fuel cells,” *Int. J. Hydrog. Energy*, vol. 35, no. 6, pp. 2403–2416, Mar. 2010.
[58] H. Heidary and M. J. Kermani, “Performance enhancement of fuel cells using bipolar plate duct indentations,” *Int. J. Hydrog. Energy*, vol. 38, no. 13, pp. 5485–5496, May 2013.
[59] C. Y. Wang, Z. H. Wang, and K. S. Chen, “Two-phase flow and transport in the air cathode of proton exchange membrane fuel cells,” *J. Power Sources*, vol. 94, no. 1, pp. 40–50, 2001.
[60] K. T. Jeng, C. Y. Wen, and L. D. Anh, “A study on mass transfer in the cathode gas channel of a proton exchange membrane fuel cell,” *J. Mech.*, vol. 23, no. 4, pp. 275–284, Dec. 2007.
[61] H. Hassanzadeh, X. G. Li, J. J. Baschuk, and S. H. Mansouri, “Numerical simulation of laminar flow development with heat and mass transfer in PEM fuel cell flow channels having oxygen and hydrogen suction at one channel wall,” *Int. J. Energy Res.*, vol. 35, no. 8, pp. 670–689, Jun. 2011.
[62] S. B. Beale, “Conjugate Mass Transfer in Gas Channels and Diffusion Layers of Fuel Cells,” *J. Fuel Cell Sci. Technol.*, vol. 4, no. 1, p. 1, 2007.
[63] S. B. Beale, “Mass transfer in plane and square ducts,” *Int. J. Heat Mass Transf.*, vol. 48, no. 15, pp. 3256–3260, Jul. 2005.
[64] M. I. Rosli, D. J. Borman, D. B. Ingham, M. S. Ismail, L. Ma, and M. Pourkashanian, “Transparent PEM Fuel Cells for Direct Visualization Experiments,” *J. Fuel Cell Sci. Technol.*, vol. 7, no. 6, pp. 061015–1–061015–7, 2010.
[65] A. D. Le, B. Zhou, H.-R. Shiu, C.-I. Lee, and W.-C. Chang, “Numerical simulation and experimental validation of liquid water behaviors in a proton exchange membrane fuel cell cathode with serpentine channels,” *J. Power Sources*, vol. 195, no. 21, pp. 7302–7315, Nov. 2010.
[66] E. C. Kumbur, K. V. Sharp, and M. M. Mench, “Liquid droplet behavior and instability in a polymer electrolyte fuel cell flow channel,” *J. Power Sources*, vol. 161, no. 1, pp. 333–345, Oct. 2006.
[67] C. D. Rath and S. G. Kandlikar, “Liquid filling in a corner with a fibrous wall—An application to two-phase flow in PEM fuel cell gas channels,” *Colloids Surf. Physicochem. Eng. Asp.*, vol. 384, no. 1–3, pp. 653–660, Jul. 2011.
[68] P. Gopalan and S. G. Kandlikar, “Droplet-Sidewall Dynamic Interactions in PEMFC Gas Channels,” *J. Electrochem. Soc.*, vol. 159, no. 8, pp. F468–F475, Jan. 2012.
[69] P. Gopalan and S. G. Kandlikar, “Effect of Channel Material on Water Droplet Dynamics in a PEMFC Gas Channel,” *J. Electrochem. Soc.*, vol. 160, no. 6, pp. F487–F495, 2013.
[70] P. K. Das, A. Grippin, A. Kwong, and A. Z. Weber, “Liquid-Water-Droplet Adhesion-Force Measurements on Fresh and Aged Fuel-Cell Gas-Diffusion Layers,” *J. Electrochem. Soc.*, vol. 159, no. 5, pp. B489–B496, 2012.
[71] T. C. Wu and N. Djilali, “Experimental investigation of water droplet emergence in a model polymer electrolyte membrane fuel cell microchannel,” *J. Power Sources*, vol. 208, pp. 248–256, Jun. 2012.
[72] K. Sugiura, M. Nakata, T. Yodo, Y. Nishiguchi, M. Yamauchi, and Y. Itoh, “Evaluation of a cathode gas channel with a water absorption layer/waste channel in a PEFC by using visualization technique,” *J. Power Sources*, vol. 145, no. 2, pp. 526–533, Aug. 2005.
[73] X. G. Yang, F. Y. Zhang, A. L. Lubawy, and C. Y. Wang, “Visualization of Liquid Water Transport in a PEFC,” *Electrochem. Solid-State Lett.*, vol. 7, no. 11, pp. A408–A411, 2004.
[74] T. Ous and C. Arcoumanis, “Visualisation of water droplets during the operation of PEM fuel cells,” *J. Power Sources*, vol. 173, no. 1, pp. 137–148, Nov. 2007.

[75] F. Y. Zhang, X. G. Yang, and C. Y. Wang, "Liquid Water Removal from a Polymer Electrolyte Fuel Cell," *J. Electrochem. Soc.*, vol. 153, no. 2, pp. A225–A232, 2006.
[76] D. Spernjak, A. K. Prasad, and S. G. Advani, "Experimental investigation of liquid water formation and transport in a transparent single-serpentine PEM fuel cell," *J. Power Sources*, vol. 170, no. 2, pp. 334–344, Jul. 2007.
[77] K. Nishida, S. Tanaka, S. Tsushima, and S. Hirai, "Image Measurement of Water Droplets in Cathode of PEFC Based on Background Subtraction Method," in *ECS Transactions*, 2011, vol. 41, pp. 419–428.
[78] A. Theodorakakos, T. Ous, M. Gavaises, J. M. Nouri, N. Nikolopoulos, and H. Yanagihara, "Dynamics of water droplets detached from porous surfaces of relevance to PEM fuel cells," *J. Colloid Interface Sci.*, vol. 300, no. 2, pp. 673–687, Aug. 2006.
[79] K. Takada, Y. Ishigami, S. Hirakata, M. Uchida, Y. Nagumo, J. Inukai, H. Nishide, and M. Watanabe, "Imaging of Water Droplets Formed during PEFC Operation on GDLs with Different Pore Sizes," *Electrochemistry*, vol. 79, no. 5, pp. 388–391, 2011.
[80] K. Nishida, T. Murakami, S. Tsushima, and S. Hirai, "Measurement of liquid water content in cathode gas diffusion electrode of polymer electrolyte fuel cell," *J. Power Sources*, vol. 195, no. 11, pp. 3365–3373, Jun. 2010.
[81] E. Gauthier, T. Hellstern, I. G. Kevrekidis, and J. Benziger, "Drop Detachment and Motion on Fuel Cell Electrode Materials," *ACS Appl. Mater. Interfaces*, vol. 4, no. 2, pp. 761–771, Feb. 2012.
[82] S. C. Cho, Y. Wang, and K. S. Chen, "Droplet dynamics in a polymer electrolyte fuel cell gas flow channel: Forces, Deformation and detachment. II: Comparisons of analytical solution with numerical and experimental results," *J. Power Sources*, vol. 210, pp. 191–197, Jul. 2012.
[83] S. C. Cho, Y. Wang, and K. S. Chen, "Droplet dynamics in a polymer electrolyte fuel cell gas flow channel: Forces, deformation, and detachment. I: Theoretical and numerical analyses," *J. Power Sources*, vol. 206, pp. 119–128, May 2012.
[84] G. Minor, N. Djilali, D. Sinton, and P. Oshkai, "Flow within a water droplet subjected to an air stream in a hydrophobic microchannel," *Fluid Dyn. Res.*, vol. 41, no. 4, p. 045506, Aug. 2009.
[85] C. E. Colosqui, M. J. Cheah, I. G. Kevrekidis, and J. B. Benziger, "Droplet and slug formation in polymer electrolyte membrane fuel cell flow channels: The role of interfacial forces," *J. Power Sources*, vol. 196, no. 23, pp. 10057–10068, Dec. 2011.
[86] M. J. Cheah, I. G. Kevrekidis, and J. B. Benziger, "Water Slug Formation and Motion in Gas Flow Channels: The Effects of Geometry, Surface Wettability, And Gravity," *Langmuir*, vol. 29, no. 31, pp. 9918–9934, Aug. 2013.
[87] C. P. Ody, "Capillary contributions to the dynamics of discrete slugs in microchannels," *Microfluid. Nanofluidics*, vol. 9, no. 2–3, pp. 397–410, Dec. 2009.
[88] P. T. Tsilingiris, "Thermophysical and transport properties of humid air at temperature range between 0 and 100°C," *Energy Convers. Manag.*, vol. 49, no. 5, pp. 1098–1110, May 2008.
[89] C. R. Wilke, "Diffusional properties of multicomponent gases," *Chem Eng Prog*, vol. 46, no. 2, pp. 95–104, 1950.
[90] E. N. Fuller, P. D. Schettler, and J. C. Giddings, "New method for prediction of binary gas-phase diffusion coefficients," *Ind. Eng. Chem.*, vol. 58, no. 5, pp. 18–27, 1966.
[91] J. P. Owejan, J. J. Gagliardo, J. M. Sergi, S. G. Kandlikar, and T. A. Trabold, "Water management studies in PEM fuel cells, Part I: Fuel cell design and in situ water distributions," *Int. J. Hydrog. Energy*, vol. 34, no. 8, pp. 3436–3444, May 2009.
[92] P. J. Pritchard, *Fox and McDonald's Introduction to Fluid Mechanics, 8th Edition*, 8 edition. John Wiley & Sons, Inc., 2010.

[93] R. Krishna and J. A. Wesselingh, “The Maxwell-Stefan approach to mass transfer,” *Chem. Eng. Sci.*, vol. 52, no. 6, pp. 861–911, 1997.
[94] S. Um and C. Y. Wang, “Three-dimensional analysis of transport and electrochemical reactions in polymer electrolyte fuel cells,” *J. Power Sources*, vol. 125, no. 1, pp. 40–51, Jan. 2004.
[95] L. Wang and H. Liu, “Separate measurement of current density under the channel and the shoulder in PEM fuel cells,” *J. Power Sources*, vol. 180, no. 1, pp. 365–372, May 2008.
[96] V. V. Dharaiya and S. G. Kandlikar, “Numerical Investigation of Heat Transfer in Rectangular Microchannels Under H2 Boundary Condition During Developing and Fully Developed Laminar Flow,” *J. Heat Transf.*, vol. 134, no. 2, p. 20911, 2012.
[97] R. K. Shah, *Fundamentals of heat exchanger design*. Hoboken, NJ: John Wiley & Sons, 2003.
[98] B. F. Armaly, A. Li, and J. H. Nie, “Measurements in three-dimensional laminar separated flow,” *Int. J. Heat Mass Transf.*, vol. 46, no. 19, pp. 3573–3582, Sep. 2003.
[99] Y. C. Cheng and G. J. Hwang, “Experimental studies of laminar flow and heat transfer in a one-porous-wall square duct with wall injection,” *Int. J. Heat Mass Transf.*, vol. 38, no. 18, pp. 3475–3484, 1995.
[100] G. J. Hwang, Y. C. Cheng, and Y. W. Chiang, “An experimental study of laminar heat transfer in a one-porous-wall square duct with suction flow,” *Int. J. Heat Mass Transf.*, vol. 40, no. 2, pp. 481–485, 1997.